The Gravitational Field of Comet Churyumov-Gerasimenko from Radio Science and Optical Data Combined Orbit Determination

Robert Jacob

Vollständiger Abdruck der von der Fakultät für Luft-und Raumfahrttechnik der Universität der Bundeswehr München zur Erlangung des akademischen Grades eines

Doktors der Naturwissenschaften

genehmigten Dissertation.

Gutachter:

1. Prof. Dr. rer. nat. Bernd Häusler

2. PD Dr. rer. nat. Martin Pätzold

Die Dissertation wurde am 05.11.2021 bei der Universität der Bundeswehr München eingereicht und durch die Fakultät für Luft-und Raumfahrttechnik am 01.03.2022 angenommen. Die mündliche Prüfung fand am 02.03.2022 statt.

Abstract

Context. ESA's Rosetta mission was launched from Kourou in 2004 to enter the orbit of the Jupiter-family-comet Churyumov-Gerasimenko after a ten-year journey through the solar system. The orbiter accompanied the comet on its way through the solar system for more than two years.

Aim. The aim of the work "The Gravitational Field of Comet Churyumov-Gerasimenko from Radio Science and Optical Data Combined Orbit Determination" is the precise determination of the comet's gravitational field parameters. The main topic is the processing of optical data from the navigation camera and the camera system OSIRIS, which were on board the spacecraft Rosetta.

Methods. The techniques developed and combined allow the accurate estimation of the camera position at the time of image acquisition. First, for the search of corresponding image points, the Scale Invariant Feature Transform (SIFT) is combined with Polynomial Least Squares Matching and a correction for the change in illumination conditions. Bundle Adjustment is used to estimate the position of the camera as well as the triangulated points on the surface of the comet, and the noise in the image data is modeled according to the t-distribution. This makes the method particularly robust against false measurements, so-called outliers.
The positions of the camera at the time of the image acquisition provide a decisive contribution to the determination of the orbit of the spacecraft relative to the comet nucleus. Already established methods of Radio Science Investigations (RSI) for orbit determination from frequency and time-of-flight measurements can thus be improved in their accuracy. The uncertainties in the spacecraft's orbit are reduced, which at the same time leads to a more accurate estimate of the comet's gravitational field parameters. In addition, the developed methods can be used to gain insights into the rotational properties of the comet.

Results. With the developed methods, 1.93×10^6 points on the comet's surface were automatically detected in 10975 images and their position was measured 36.88×10^6 times with subpixel precision. All images used originate from orbits within 35 kilometers of the comet's nucleus. The reprojection error of the triangulated points results in 0.6 pixel RMS, achieving subpixel accuracy in the bundle adjustment. The average uncertainty of the resulting camera positions is 7 meters across all images and 3.7 meters in the close orbits at the end of the mission in 2016. Before perihelion, an increase in the rotation period from 12.4040 to 12.4060 ± 0.0001h can be measured from September 2014 to February 2015 due to comet outgassing. After perihelion, a decreasing rotation period from 12.0607 to 12.0567 ± 0.0001h is observed from February to September 2016. Additional periods in a rotation mode beyond the main inertial axes could not be confirmed. From orbital integration of the spacecraft, a gravity field in spherical harmonics up to degree and order 4 could be determined. Within the uncertainties all gravity field coefficients are in the range of a homogeneous density distribution within the nucleus. With $GM = 665.71 \pm 0.43$ $\mathrm{m^3 s^{-2}}$ in August 2016, the total mass of the comet could be determined based on optical data. When combined with the established methods from Doppler measurements, this results in a reduction of the uncertainties of the gravity field parameters to 53 % of the initial values.

Conclusions. With this work a method is presented, which allows the estimation of physical parameters of the comet Churyumov-Gerasimenko from optical data received from the orbiter. In agreement with other publications, the interior of the nucleus is characterized by a homogeneous density distribution. This is in good agreement with current theories on the formation of the solar system.

Kurzfassung

Kontext. Die ESA Mission Rosetta wurde 2004 von Kourou gestartet, um nach einer zehnjährigen Reise durch das Sonnensystem in die Umlaufbahn des Jupiter-Familien-Kometen Churyumov-Gerasimenko einzutreten. Der Orbiter begleitete den Kometen mehr als zwei Jahre auf seinem Weg durch das Sonnensystem.
Ziel. Das Ziel der Arbeit „The Gravitational Field of Comet Churyumov-Gerasimenko from Radio Science and Optical Data Combined Orbit Determination“ ist die genaue Bestimmung der Schwerefeldparameter des Kometen. Hauptthema ist dabei die Verwendung von optischen Daten der Navigationskamera sowie des Kamerasystems OSIRIS, welche sich an Bord der Raumsonde Rosetta befanden.
Methoden. Es werden Verfahren entwickelt und kombiniert, welche die genaue Schätzung der Kameraposition zum Zeitpunkt der Aufnahme ermöglichen. Für die Suche korrespondierender Bildpunkte wird zunächst die Scale Invariant Feature Transform (SIFT) mit Polynomial Least Squares Matching und einer Korrektur für veränderliche Lichtverhältnisse kombiniert. Zur Schätzung der Position der Kamera sowie der triangulierten Punkte auf der Oberfläche des Kometen wird Bundle Adjustment genutzt, wobei das Rauschen in den Bilddaten entsprechend der t-Verteilung modelliert ist. Dies macht das Verfahren besonders robust gegenüber Falschmessungen, sogenannten „Outliers“. Die dabei gewonnenen Positionen der Kamera zu den Zeitpunkten der Bildaufnahme liefern einen entscheidenden Beitrag dazu, den Orbit der Raumsonde relativ zum Kometenkern zu bestimmen. Bereits etablierte Methoden von Radio Science Investigations (RSI) zur Bahnberechnung aus Frequenz- und Lichtlaufzeitmessungen können dadurch in ihrer Genauigkeit verbessert werden. Die Unsicherheiten im Orbit der Raumsonde werden reduziert, was zugleich zu einer genaueren Schätzung der Schwerefeldparameter des Kometen führt. Zusätzlich lassen sich mit den entwickelten Methoden Erkenntnisse über die Rotationseigenschaften des Kometen gewinnen.
Ergebnisse. Mit den entwickelten Methoden wurden automatisiert 1.93×10^6 Punkte auf der Kometenoberfläche in 10975 Aufnahmen detektiert und deren Koordinaten in 36.88×10^6 Bildpunkten subpixelgenau vermessen. Alle verwendeten Aufnahmen stammen aus Bahnen innerhalb von 35 Kilometern Abstand zum Kometenkern. Der Reprojektionsfehler der triangulierten Punkte resultiert in 0.6 Pixel RMS, womit Subpixelgenauigkeit im Bundle Adjustment erreicht wird. Die durchschnittliche Unsicherheit der resultierenden Kamerapositionen beträgt über alle Aufnahmen hinweg 7 Meter und 3.7 Meter in den nahen Orbits am Ende der Mission im Jahr 2016. Vor Perihel kann von September 2014 bis Februar 2015 aufgrund der Kometenausgasung ein Anstieg der Rotationsperiode von 12.4040 auf 12.4060 ± 0.0001h gemessen werden. Nach Perihel wird von Februar bis September 2016 eine sinkende Rotationsperiode von 12.0607 auf 12.0567 ± 0.0001h beobachtet. Zusätzliche Perioden jenseits der Hauptträgheitsachsen konnten nicht bestätigt werden. Aus Bahnintegration der Raumsonde konnte ein Schwerefeld in Kugelflächenfunktionen bis Grad und Ordnung 4 ermittelt werden. Innerhalb der Unsicherheiten liegen alle Schwerefeldkoeffizienten im Bereich einer homogenen Dichteverteilung innerhalb des Nukleus. Mit $GM = 665.71 \pm 0.43$ $\mathrm{m^3 s^{-2}}$ im August 2016 konnte die Gesamtmasse des Kometen basierend auf optischen Daten ermittelt werden. Bei Kombination mit den etablierten Methoden aus Dopplermessungen ergibt sich eine Verringerung der Unsicherheiten der Schwerefeldparameter auf 53 % der Ausgangswerte.
Zusammenfassung. Mit dieser Arbeit wird eine Methode vorgestellt, welche die Schätzung physikalischer Parameter des Kometen Churyumov-Gerasimenko aus optischen Daten des Orbiters ermöglicht. Das Innere des Nukleus ist dabei übereinstimmend mit anderen Publikationen von einer homogenen Dichteverteilung geprägt. Dies steht in guter Übereinstimmung mit gängigen Theorien zur Entstehung des Sonnensystems.

Selbstständigkeitserklärung

Ich versichere, dass ich die vorliegende Arbeit selbstständig verfasst und nur die angegebenen Quellen und Hilfsmittel verwendet habe. Insbesondere versichere ich, dass ich alle wörtlichen und sinngemäßen Übernahmen aus anderen Werken als solche gekennzeichnet habe.

.....

"Remember to look up at the stars and not down at your feet. Try to make sense of what you see and wonder about what makes the universe exist. Be curious. And however difficult life may seem, there is always something you can do and succeed at. It matters that you don't just give up."

Professor Stephen Hawking

Contents

1. Introduction, Motivation, and Goal

In the early stages of the solar system, a rotating disk of dust and gas surrounded its center of mass and slowly but continuously lost homogeneity. About 4.6 billion years later, one observes a dynamic system with the Sun in its center and multiple dense objects surrounding it, such as planets and dwarf planets as well as asteroids and comets.

From a rotating disk until the stage of a dynamic solar system as it may be observed today, many unanswered questions about the physical processes remain. How did the planets form in detail? Why does planet Earth have such a big amount of liquid water? When investigating processes that formed the planets billions of years ago, a well-established method is the detailed analysis of geologic material. However, since Earth is an active planet, the material found is of limited value because it went through reforming processes a couple of times. To account for this, it is helpful to analyze the structure and composition of primordial objects like asteroids and comets, since they may contain unchanged material from the first stage of solar system development [111][15]. They provide information about its chemical composition as well as how the material has compounded and formed these objects [81][112]. With the ambitious goal to find answers to questions like those and many more, in 2004, ESA successfully launched the Rosetta mission for a meeting with comet 67P/ Churyumov-Gerasimenko.

The wide field of scientific objectives for the mission may be seen through the various instruments onboard the orbiter, starting from multiple camera systems over detailed particle analysis up to the landing unit “Philae”, to name just a few of them. One scientific goal addresses fundamental aspects of cometary physics, such as the gravitational field, mass, bulk density, and the internal structure of the nucleus [94].

Information about the inner mass distribution is of great value for fundamental physics as it may support the basic theory in our understanding of solar system evolution. It can be revealed from a precise analysis of the gravitational field, which may be described by gravitational coefficients in spherical or ellipsoidal harmonics. Thus, the estimation of the cometary mass together with its gravitational coefficients is one of the main goals for the Radio Science Investigations (RSI) experiment [94].

To get a detailed understanding of the gravitational field, the analysis of spacecraft acceleration caused by the target body is necessary. It may be estimated from the processing of Doppler shifts in the up- and downlink frequency, caused by changes in relative velocity along the signal line of sight. The functionality of this method has been proven in multiple previous applications, such as the flybys at Mercury, Uranus,

Neptune and the Galilean satellites at Jupiter. Further measurements were obtained at Phobos, Eros, Mathilde, Lutetia, Steins and comet P/Wild-2 [94].

However, the comet Churyumov-Gerasimenko offers additional challenges to this procedure. Here, the spacecraft was established orbiting the target body for a long period instead of a flyby comparable to previous applications. The gravitational influence of 67P is generally small, since the nucleus size is smaller than 5km and its density appears to be small as well. Furthermore, due to the comet's outgassing activity, an additional non-gravitational force resulting from particle impulse on the spacecraft causes perturbing accelerations that need to be distinguished from the target body's gravity.

To overcome challenges such as these, an additional measurement for the spacecraft trajectory around the nucleus is obtained from optical data [113][114][93]. The Rosetta Navcam, as well as the Optical, Spectroscopic, and Infrared Remote Imaging System (Osiris), frequently took images of the comet during the orbiting phases of the mission. Besides the many stunning features and details in those images, they also provide the possibility to obtain the position of the spacecraft at the particular point in time when an image was taken. This information is of great value in determining the influence of the gravitational field on the spacecraft trajectory.

In this dissertation, a method is introduced that processes images from the Rosetta mission in a way, that the relative spacecraft-position can be extracted from it. These positions, in turn, can then be combined with the RSI established method of mass and gravitational coefficient estimation in a way that existing solutions can be improved to a higher level of accuracy. The methods and techniques used, as well as a detailed summary of all the results, will be discussed in this work.

1.1. The Rosetta Mission

The Rosetta spacecraft was launched by an Ariane-5 on 2 March 2004 from Kourou. To join the orbit for an escort of comet Churyumov-Gerasimenko, four gravity assist maneuvers were accomplished - three from Earth and one from Mars (Figure 1). On its journey, Rosetta also flew past two asteroids. It passed Steins on 5 September 2008 and Lutetia on 10 July 2010. While orbiting beyond the main asteroid belt, Rosetta was the first spacecraft that was solely powered from solar cells. For this reason, it had to enter deep space hibernation in June 2011. The spacecraft woke up in January 2014 and arrived at Comet 67P/ Churyumov-Gerasimenko in August 2014. On 12 November 2014, the lander Philae was detached from the spacecraft and slowly descended to the cometary surface.

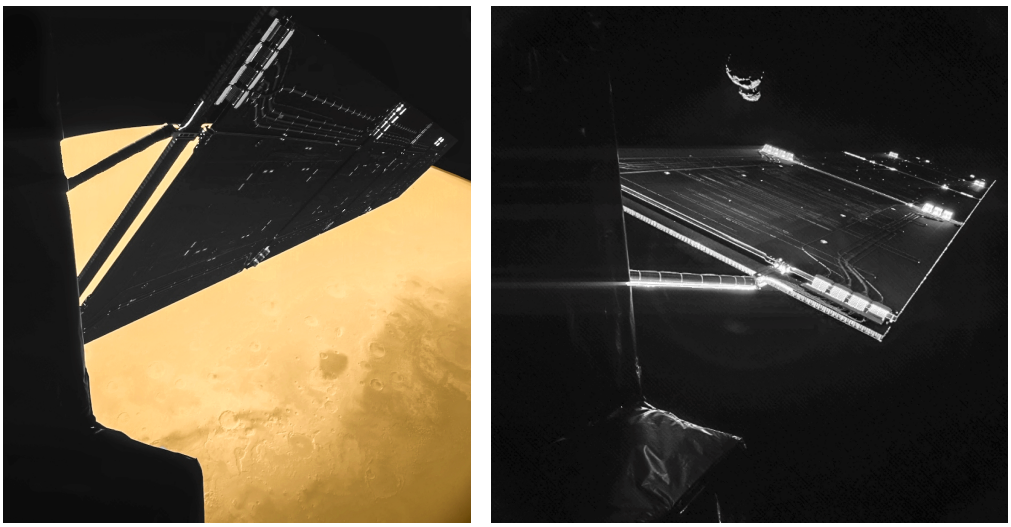

Figure 1: Images of Rosetta's 14 meter-long solar array taken by the CIVA camera on Rosetta's lander Philae. Mars is visible in the background on the left image, which was taken during the gravity assist flyby in February 2007. On the right hand side, comet Churyumov-Gerasimenko can be seen in the background on an image that was taken more than seven years later in October 2014. ESA/Rosetta/Philae/CIVA [31].

Rosetta escorted the comet towards perihelion and on its way back to the orbit of Jupiter. The mission ended with a controlled descent of the spacecraft to the cometary surface. A time line with the most important events of the Rosetta mission can be found in Table 1.

Figure 2: An illustration of Rosetta orbiting the comet Churyumov-Gerasimenko. Sources: spacecraft - ESA/ATG medialab / comet image - ESA/Rosetta/-NAVCAM [31].

The spacecraft bus measured 2.8 x 2.1 x 2.0 meter with two 14 meter long solar panels (Figure 2). It was equipped with a variety of instruments for remote sensing and radio science to study the composition, mass distribution, and dust flux of the comet's nucleus. Additionally, the comet's plasma environment and its interaction with the solar wind was investigated. The instruments onboard Rosetta were mounted on one side of the spacecraft, which typically faced the comet during the escort. Until its release, the lander Philae was carried on the opposite side to the large high-gain antenna. The information in this subsection was taken from [31][109]. Detailed descriptions of the Rosetta payload can be found in [102].

Date	**Event**
2 March 2004	Launch
4 March 2005	1st Earth flyby
25 February 2007	Mars flyby
13 November 2007	2nd Earth flyby
05 September 2008	Flyby - asteroid Steins
13 November 2009	3rd Earth flyby
10 July 2010	Flyby - asteroid Lutetia
08 June 2011	Enter deep space hibernation
20 January 2014	Exit deep space hibernation
06 August 2014	100 km from comet 67P - arrival
12 November 2014	Release and landing of Philae
13 August 2015	Perihelion
12 December 2015	End of nominal mission
30 September 2016	End of mission extension

Table 1: Key events during the Rosetta mission [31].

1.2. Problem Description and Emphasis

When a spacecraft transmits a signal towards an antenna located at the surface of the Earth, established methods accurately predict the radio frequency that is expected to be measured at that ground station. If all other contributions to the radio signal are known, an observed change in the signal frequency can be associated to the Doppler shift caused by velocity changes of the spacecraft. If the velocity change is caused by the gravitational acceleration through the target body, the mass as well as gravitational

coefficients may be estimated from it. RSI has been able to determine the mass of asteroid Lutetia from Rosetta's flyby with an error of 1 % using this method [3].

However, the Doppler shift only gives evidence of velocity changes along the signal's line of sight. Accelerations perpendicular to the signal's line of sight can not be observed in the measured frequency. Additionally, at the beginning of the measurement, the position of the spacecraft relative to the target body must be estimated, if no further information is available. More difficulties can arise from the influence of Earth's atmosphere on the radio signal.

Another important problem is the uncertainty in the orbit of the target body relative to the solar system. The forces acting on a comet may not be described from the gravitational influence of solar system bodies alone, since its outgassing continuously adds perturbations to its orbit and, therefore, significantly changes its trajectory on its way through the solar system. This phenomenon, in turn, can lead to higher uncertainties concerning the target body's and the orbiter's position relative to Earth, adding an additional offset between measured and predicted frequency. Hence, the frequency changes caused by an outgassing-induced orbital change of the comet must be distinguished from those induced by spacecraft acceleration through cometary gravity alone.

At this point, optical data can improve the solution to a higher level of accuracy, since it provides three-dimensional information about the spacecraft's position at the time when an image was taken [105][91][66]. Thus, the data enables the determination of both the relative position of the spacecraft as well as the gravitational acceleration in all directions when comparing the changes in spacecraft position obtained from consecutive image series, irrespective of the downlink signal's line of sight.

From the Rosetta mission, large sets of scientific data are accessible for the Navigation Camera (NAVCAM) as well as the OSIRIS Narrow Angle Camera (OSINAC) and Wide Angle Camera (OSIWAC). These images can be filtered and processed in multiple ways, covering a wide spectrum of possible scientific goals. However, with terabytes of optical data available, the cost in terms of computation time can quickly grow to an unacceptable amount, if the type of processing is not adapted to a specific scientific goal. Therefore, through development of the associated methods and routines, it is important to define a specific point of view regarding what exactly defines the outcome that is needed from the data.

For this purpose, one important consideration arises especially from a comet, because one observes an actively changing surface throughout the mission. Thus, when carrying out a three-dimensional reconstruction, one always reconstructs an object that is chang-

ing over time - and, therefore, obtains a built-in uncertainty for landmarks. The first row in Figure 3 shows two images several months prior perihelion in August 2014 and January 2015. This timeframe is of great value for estimating the gravitational field of the comet, because in between orbits were flown in close proximity. Therefore, optical reconstruction from images like these is needed to get an improved solution. However, significant changes on the cometary surface appeared during that time, potentially leading to inaccuracies in estimation of three-dimensional geometry. Regarding longer time frames and according to [28], parts of the cometary surface changed in elevation up to several meters during the mission (Figure 4). If a landmark is defined in such an area, the associated change in its position can also influence the corresponding reconstructed spacecraft orbit, possibly leading to errors in the precise orbit determination process.

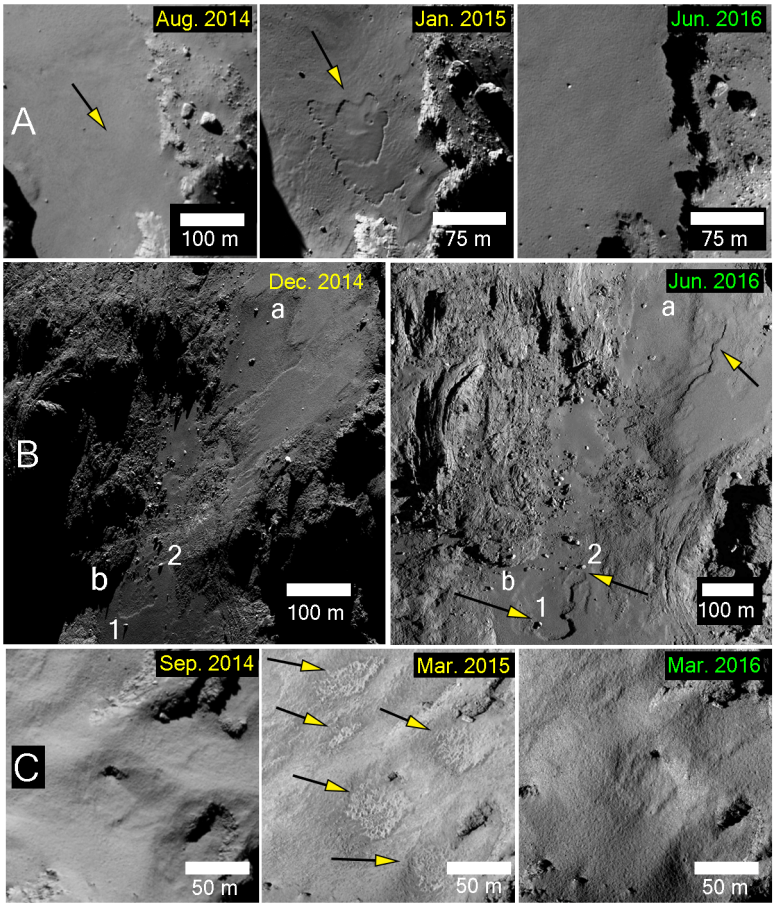

Figure 3: Changes on the cometary surface visible throughout the Rosetta mission [28].

Last but not least, the comet constantly changes its rotational period, which offers additional challenges to navigation, since the rotational state must be estimated as a part of the relative orbit determination process and cannot just be assumed as constant.

Summarized, a constantly changing object with a previously unknown relative position, orientation, and scale accompanied by a continuously changing rotational period represents a challenging environment to improve the orbit reconstruction with optical data. Hence, the **reconstruction from key point correspondences in combination with a robust statistical approach** is the method of choice for this work.

Corresponding key points will be detected in the imagery data and, in this way, images are linked relative to each other, yielding relative geometric information. Thus, there is no requirement for a fixed three-dimensional model of the comet to achieve the information that is needed: the relative position and orientation of the camera reference frame at the time when an image was taken.

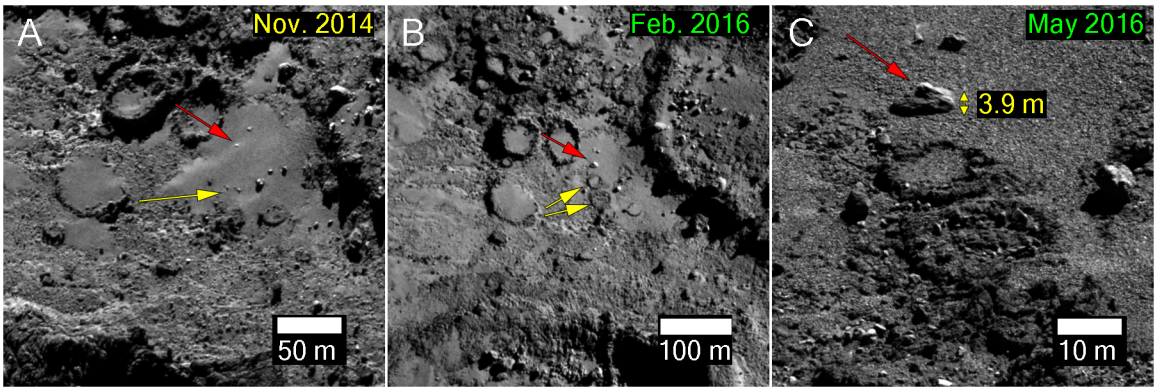

Figure 4: Changes in cometary surface elevation due to outgassing activity [28].

The key points detected and matched to each other through a series of images only depend on the received sensor data itself, thus minimizing the need for assumptions, such as the albedo of the cometary surface. In the end, only minimized residuals for the reprojected tie points lead to an optimal solution for the relative geometric reprojection problem. In this way, the orbit accuracy can be improved without the need for a fixed model of comet 67P which is altering its surface slowly over time.

Another important goal of this work is to have the computational process running based on a high level of automation. A minimum requirement of attention and interference from the user is wanted, since thousands of images need to be processed.

1.3. Subdivision in Areas of Interest

Broadly, the development of routines and methods in this work may be subdivided into three major steps. First, distinctive points in the images must be automatically detected and matched. The result of this step is a list of key points observed in multiple images, measured in two-dimensional coordinates together with the associated uncertainties.

After corresponding keypoints were detected within the imagery data, in a second step, the relative geometry between the observing cameras and the key points on the cometary surface can be estimated. Besides the position of the orbiter, also the location

of the key points on the cometary surface is determined through triangulation and updated as additional measurements are taken into account (Figure 5). Hence, no a priori knowledge concerning the shape of the target body is necessary.

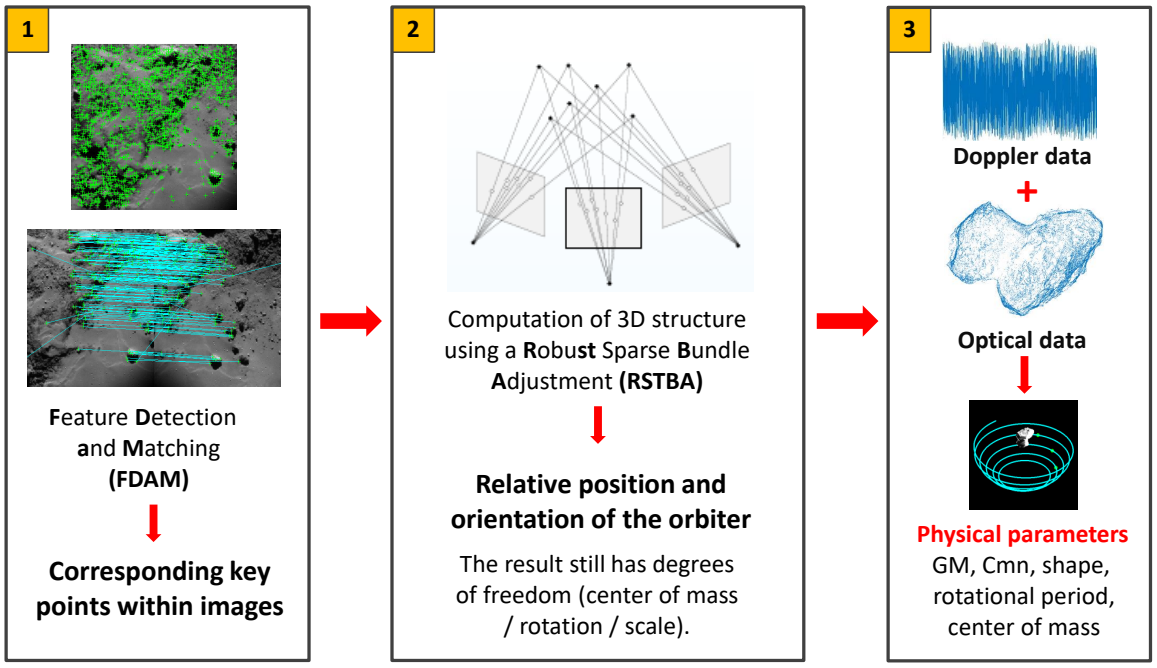

Figure 5: The three main areas of interest from left to right: The feature detection and matching algorithm **(FDAM)** together with robust sparse bundle adjustment **(RSTBA)** leading to the main goal of this work, the estimation of physical parameters of comet 67P [52].

In the third and last step of methods developed within this work, physical parameters of the comet can be revealed from the previously estimated geometric relationship. In combination with the simulation of Doppler data from the radio carrier links of the spacecraft's Telemetry, Tracking and Command subsystem, the improvement in the accuracy through the combination of both methods will be shown.

1.3.1. Feature Detection and Matching - FDAM

The main goal for this part is the detection of maximally repeatable and stable key points - i.e., the maximum number of possible observations per key point with the highest possible, subpixel accuracy. The method also must be robust with respect to significant changes in relative scale or illumination. Two-dimensional uncertainty estimates should be available for each key point measurement. This first part is referred to as the "feature

detection and matching" **(FDAM)** algorithm and is described in subsection 3.1.

1.3.2. Robust Bundle Adjustment - RSTBA

The technique that estimates relative geometry of the cameras and surface points out of the measurements obtained from the **FDAM** algorithm is called bundle adjustment. The main challenge in this approach is, that outliers must be considered in the data from **FDAM**. Generally, outliers can arise, for example, from significant changes in illumination or just in parts of the cometary surface that are very similar but, in fact, do not refer to the same point. On top of this, parts of the cometary surface were actually moving. If the boulder-like feature in the image pair C of Figure 6 gets detected by the **FDAM** algorithm and is being measured in the two consecutive images, it now relates to a new position on the surface and can consequently cause errors in the estimation process. Accordingly, the existence of outliers cannot be avoided. For this reason, a robust algorithm that automatically filters outliers in the three-dimensional estimation process is needed. The associated part of this work is called "robust bundle adjustment", **RSTBA** and is thoroughly discussed in subsection 3.2.

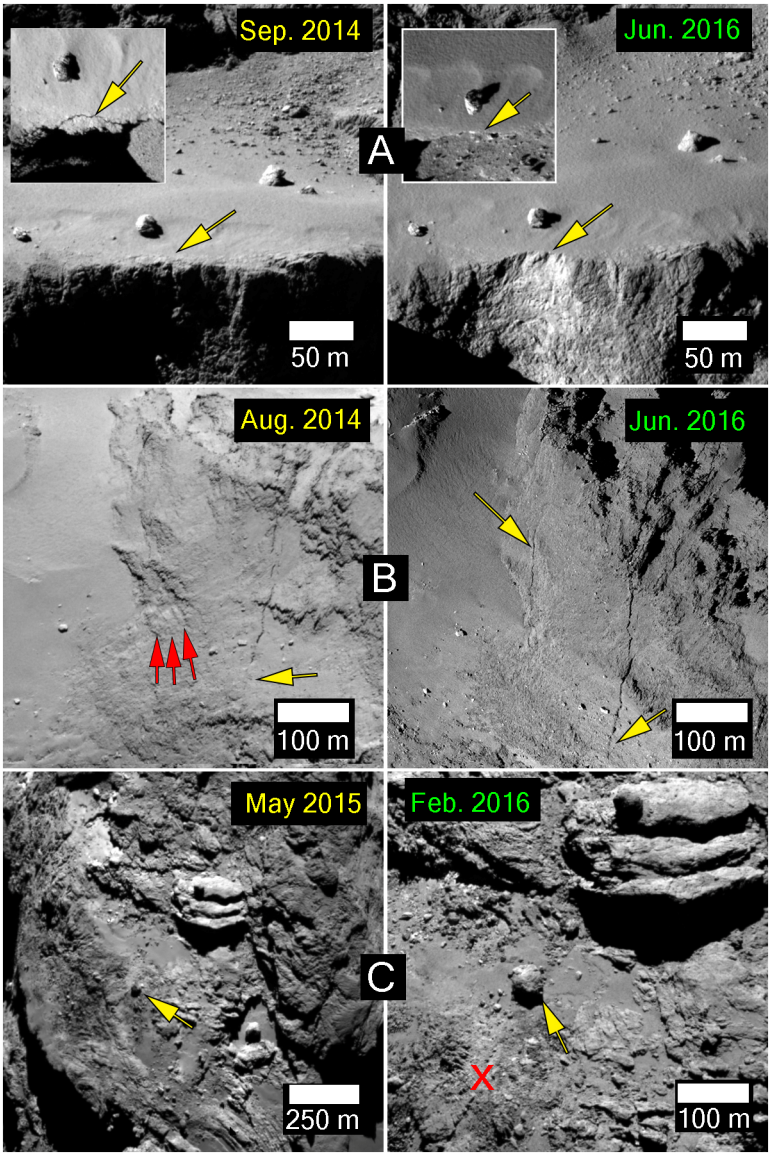

Figure 6: Significant alterations of cometary landmarks from August 2014 until June 2016 including a 30 meters sized boulder-like feature that has moved from its origin by more than 100 meters [28].

1.3.3. Cometary Parameter Estimation

The result that can be obtained from the **RSTBA** bundle adjustment is pure relative geometric information; it is reconstructed in a body-fixed frame without any physical properties. There is only a reprojected geometric relation resulting from minimized residuals in the optical data, thus leaving seven open degrees of freedom. Three of them arise from translation, three from rotation, and one from scale ambiguity (Figure 7). To determine the position of the spacecraft relative to the comet with the correct scale, some additional measurement that is referred to as "ground-truth" is necessary, i.e., the exact location of features visible in the optical data must be known. However, when arriving at a comet, there is no fixed measurement on the "ground" of 67P available that could define the absolute position, orientation, and scale of the scene visible in the images. Hence, the positions of the landmarks need to be defined based on the orbit of the spacecraft relative to the comet. Because of this, the reconstructed orbit is constrained with the correct scale through the combination of the geometry derived from optical data with the Doppler and ranging measurements from the radio carrier links. Accordingly, the third main section of methods and algorithms in this work combines the pure geometric relation from **FDAM** and **RSTBA** with real **cometary physics** and, in this way, leads to improved solutions for the spacecraft orbit together with physical parameters, such as total mass, bulk density, the gravitational field, and the rotational state of the comet. The used methods are described in subsection 3.3.

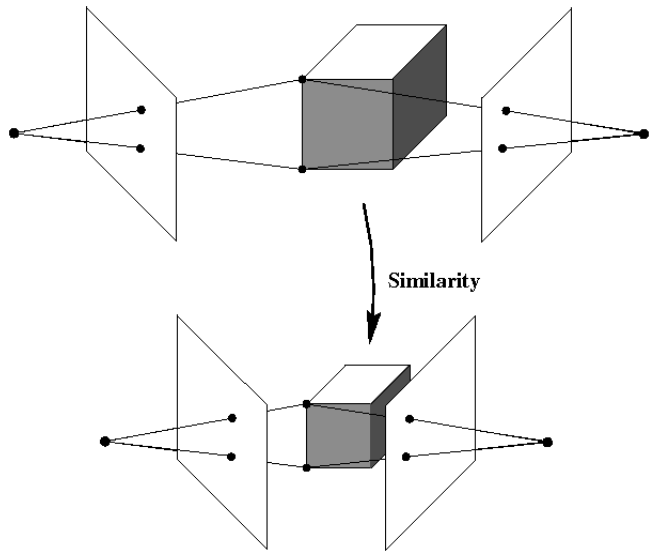

Figure 7: From projective optical data alone, the overall scale of an observed scene cannot be determined [52].

In section 4, all results obtained within this work are explained, and discussed. This includes the interim results from **FDAM** and **RSTBA** together with the main goal of this work, the gravitational field of comet 67P. Here, an orbit solution from simulated Doppler data alone is compared to a solution combined with optical data, estimating the expected improvement in accuracy. Section 4 also includes topics about the evolution

of the rotational period and the search for non-principal-axis rotation.

In this introduction, the three areas that are crucial to achieve the main goal of this work were introduced. Additionally, a brief review of the Rosetta mission was given. In the next section, all definitions and theoretical aspects that are necessary for the development of the methods in subsections 3.1, 3.2 and 3.3 are explained.

2. Definitions and Theory

In the following section, all theoretical aspects which are fundamental to the methods used in this work will be discussed. All related equations will be briefly set up and explained together with the corresponding definitions. Within the given references, amplifying information and more detailed explanations may be found. The reader of this document may also continue with section 3 to obtain a common theme about what actually was implemented in all components of the software and then step back into section two if questions concerning the related theory arise.

In this work, the following notation standard will be used. The column vectors $\mathbf{x} \in \mathbb{R}^n$ and row vectors $\mathbf{x}^\mathsf{T} \in \mathbb{R}^n$ with scalar-valued entries x_i are written in bold letters, and matrices $\mathrm{A} \in \mathbb{R}^{m \times n}$ are written in capitalized non-bold letters as

$$\mathbf{x}^\mathsf{T} = [x_1, x_2, \ldots, x_n]\,, \tag{1}$$

$$\mathbf{x} = \begin{bmatrix} x_1 \\ \vdots \\ x_n \end{bmatrix}, \quad \mathrm{A} = \begin{bmatrix} a_{11} & \cdots & a_{1n} \\ \vdots & \ddots & \vdots \\ a_{m1} & \cdots & a_{mn} \end{bmatrix}. \tag{2}$$

2.1. Celestial Mechanics Definitions

In this subsection, all celestial mechanics related definitions that are needed within this work are described.

2.1.1. Reference Frames

International Celestial Reference Frame ICRF

The position of the ecliptic and the central Earth equator to the standard epoch on 1 January 2000 at 12 noon UT1 are used to define the orientation of the International Celestial Reference Frame (ICRF) coordinate system. The first coordinate at this time is aligned towards the mean vernal equinox, the second towards the increasing obliquity. This coordinate system is rotation-free. The origin lies in the barycenter of the solar system. The actual alignment of the reference frame is based on observations of extra-galactic reference points, which implies a small difference from equatorial coordinates. For all results derived within this work, however, this difference is negligible. Comet orbit integration was performed in this coordinate system [85].

International Terrestrial Reference Frame ITRF

The International Terrestrial Reference Frame ITRF is an Earth-fixed rotating coordinate system. It has its origin in the center of gravity of the Earth. The ITRF is defined by the true equatorial plane. The first coordinate is aligned in the direction of the intersection between the equatorial plane and the Greenwich meridian. This coordinate frame is used to compute the position and relative motion of ground stations [85][3].

Cheops Frame Definition for 67P

In order to be able to use one common reference frame for the Rosetta mission target 67P/ C-G, the so called **Cheops reference frame** (Figure 9) was defined following the first results about the cometary rotation and center of mass. It was initially based upon the analysis of images that were acquired in August and September of 2014 [34]. Prominent landmarks were chosen to define zero longitude and latitude (Figure 8).

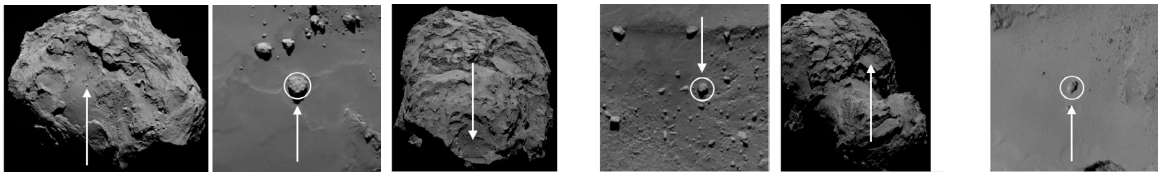

Figure 8: From left to right: boulder-like features in the Cheops, Hatmehit, and Seth region defining the Cheops Reference Frame [34][99].

These landmarks are assumed to be large enough to not undergo significant positional changes during the mission. For the definition of zero longitude, i.e., the orientation of the x-axis, the boulder-like feature in the Cheops region on the 67P/ C-Gs big lobe was selected. Its spherical coordinates were fixed to 142.35° right-hand-rule eastern longitude and $-0.28°$ latitude. The center of a secondary boulder-like feature near the equator on the opposite lobe in the Hatmehit region was fixed at 354.69° longitude and 3.48° latitude. Last, the center of the third feature in the Seth region was at 157.82° longitude and 71.99° latitude. The Frame is body-fixed and rotates with the comet, however not at a fixed rate. The observed changes in the rotational period of the 67P/ C-G will be discussed thoroughly in Chapter 4. More information about the Cheops Frame definition can be found in [34][99].

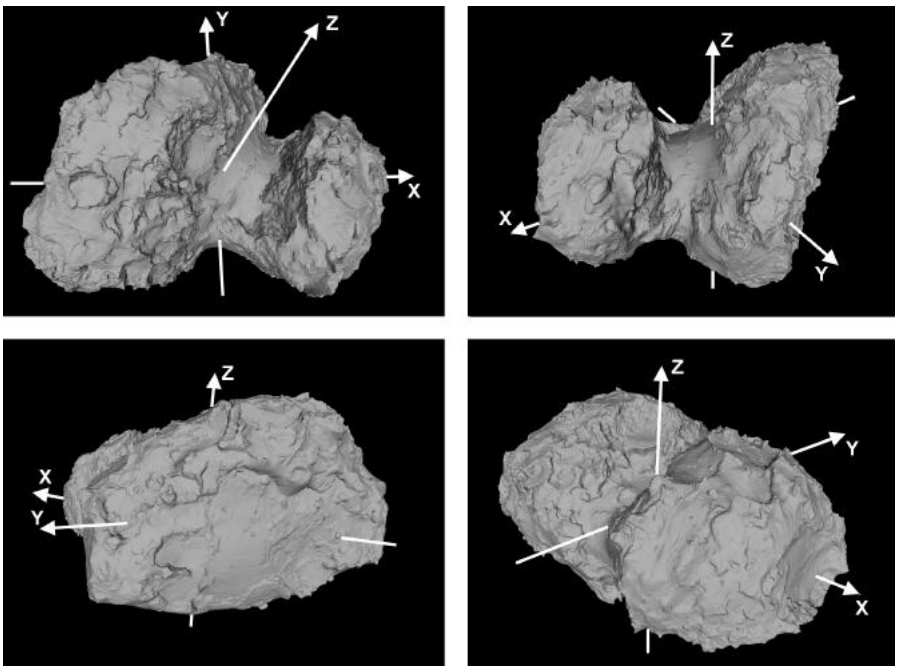

Figure 9: The cometary shape, position, and orientation in the Cheops Reference Frame [99][100].

Rosetta Mechanical Spacecraft Frame

The Rosetta mechanical spacecraft Frame (Figure 10) is defined by its +Z axis, which is perpendicular to the launch vehicle interface plane, and points toward the payload side.

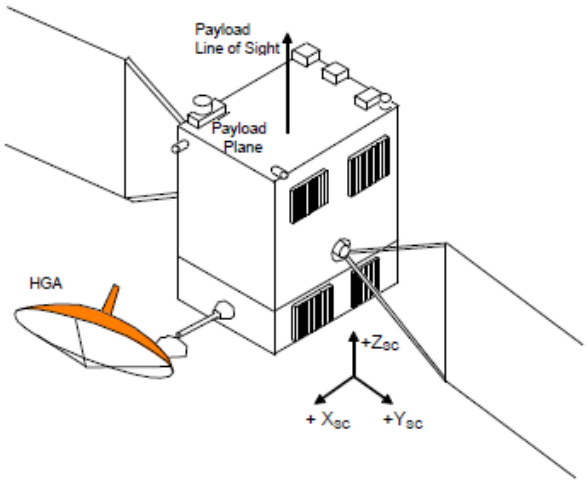

Figure 10: The Rosetta mechanical spacecraft frame [27].

The +X axis is perpendicular to the High Gain Antenna (HGA) mounting plane and points towards it parallel to the antenna mounting axis. The +Y axis completes the right-handed frame. The origin of this frame is the launch vehicle interface point. Note that the origin of the Rosetta spacecraft frame may also be defined as the spacecraft's center of Gravity, which changes during the mission. The center of the Rosetta mechanical spacecraft frame, however, remains unchanged. More information can be found in [27].

2.1.2. Time

A multitude of historically grown concepts of both the definition and measurement of time have evolved in the last century. Especially in astronomical observations, time definitions with distinct scalings arose because atomic clocks run slower when they are in relative motion or experience gravitational influence. Therefore, time is a variable that requires careful attention in the description of astronomical and physical phenomena [85].

In general, time may be subdivided in three timescales, Dynamical Time, Atomic Time and Mean Solar Time or Sidereal Time. The last two are determined by the rotation of the Earth. For example, Universal Time (UT) is defined as the time between two meridian transits of the fictitious mean Sun. The Sidereal Time definition uses the same principle, but measured relative to fixed stars.

When evidence of irregularities in the Earth's rotation became apparent, additional time bases were defined. The International Atomic Time (TAI) is based on the SI second defined by hyperfine radiation of cesium-133 atoms and depicts the basis for the definition of UTC. The TAI timescale does not depend on other timescales or Earth's rotation.

Dynamical Time, such as Ephemeris Time, depicts a number of uniform timescales and is used as the independent variable in the equations of motion in celestial mechanics. Dynamical Time includes the time variables of geocentric and barycentric ephemeris as Terrestrial Dynamical Time (TDT) or Terrestrial Time (TT) and Barycentric Dynamical Time (TDB), as well as relativistic time coordinates; for example, in the 4-dimensional geocentric frame (Geocentric Coordinate Time TCG) or the 4-dimensional barycentric frame (Barycentric Coordinate Time TCB) [85].

In this work, only Universal Time Coordinated (UTC) and Ephemeris Time, as referred to as Barycentric Dynamical Time, are used. To ensure that with all methods and results in this work the basic variable of time is clearly defined for all further use,

the corresponding definitions will be introduced.

Universal Time Coordinated (UTC)

Universal Time Coordinated (UTC) is obtained from atomic clocks that run at the same speed as International Atomic Time (TAI) or Terrestrial Time (TT). These atomic clocks are located at the surface of the Earth. The UTC time format is always within a 0.7 seconds difference from Universal Time ($UT1$). The introduction of leap seconds ensures that this difference is not exceeded. However, this time definition is consequently not steady. The International Earth Rotating Service (IERS) can add these leap seconds if necessary at the end of June or December of each year. This means that the UTC can only be determined for a past time. However, forecasts are also published by the IERS, which is particularly important for planning future missions based on UTC. With

$$UTC = TAI - LS, \tag{3}$$

UTC can be determined from International Atomic Time and the number of leap seconds [85][3].

For both the Rosetta Navcam and Osiris-Nac, there is a predefined time slot of exposure to light. In this time, the pixel value evolves from photon impact on the CCD. Thus, for each image of the two camera's systems, a start- and stop time is given in UTC. Hence, for all image-defined spacecraft positions in this work, the average between the two values is used as a time reference.

Ephemeris Time (ET)

Ephemeris Time provides a conceptually smooth and uniform time scale. It is defined as the number of TDB seconds since the Greenwich noon, 1 January 2000 Barycentric Dynamic Time, also known as the J2000 epoch. All precise solar system ephemeris are so far based on a TDB time scale [85]. TDB is adjusted from Terrestrial Time (TT), which is defined based on the SI second as

$$TT = TDT = TAI + 32.184\,[s]\,. \tag{4}$$

With (3) one may obtain TDB from UTC via [3]

$$TDB = UTC + LS + 32.184\,[s] + \Delta_{TDB,TT}, \tag{5}$$

with the difference $\Delta_{TDB,TT}$ that evolves from the relativistic framework and depends on the Julian Date at the time of transformation.

In this work, all processed scientific measurements are based and referenced on a UTC time. The transformation to the corresponding Ephemeris Time is done through the above equations using SPICE routines.

2.2. Gravitational Forces

In the following subsection, all gravitational forces that act on the spacecraft will be described.

2.2.1. N-Body Equation

The Newtonian equations of motion for n point masses in gravitational influence are known as (Figure 11)

$$\ddot{\mathbf{r}}_i = \sum_{j=1, j\neq i}^{n} \frac{\mu_j}{r_{ij}^3}\mathbf{r}_{ij}, \quad (i = 1, 2, 3, ..., n), \tag{6}$$

with

$$\begin{aligned} \mathbf{r}_{ij} &= \mathbf{r}_j - \mathbf{r}_i, \\ r_{ij} &= \|\mathbf{r}_j - \mathbf{r}_i\|_2\,, \\ \mu_j &= GM_j, \end{aligned} \tag{7}$$

where G denotes the gravitational constant and M_j the j-th mass of an attracting point mass. If all ephemeris and masses of the bodies M_j with $(j = 1, 2, 3, ..., n,\ j \neq i)$ are known, the trajectory of the i-th point mass M_i can be integrated in an inertial frame [59][85].

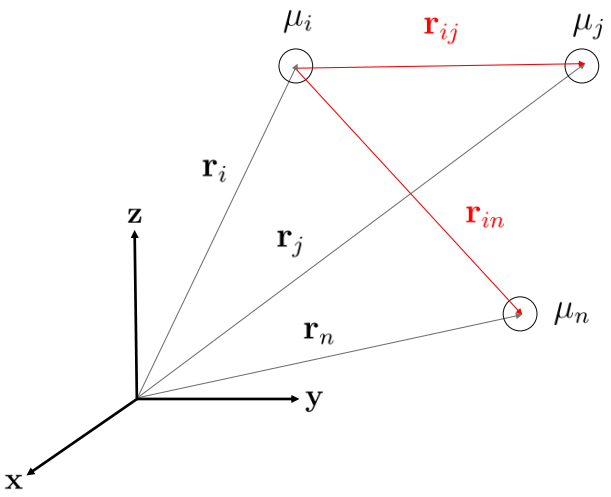

Figure 11: The definition of vectors describing the positions of attracting point masses in (6) where $\mathbf{r}_i$ is the vector that describes the position of the i-th point mass in the reference frame ICRF, whereas $\mathbf{r}_{ij}$ describes the position of the j-th point mass relative to the i-th point mass.

2.2.2. Third-Body-Perturbations

When orbit integrations in a reference frame of a central body other than the Sun are desired, the coordinate frame itself is now subject to gravitational acceleration and therefore may not be considered inertial anymore. It is then necessary to distinguish between central body acceleration and perturbing accelerations which are a result of the gravitational acceleration of the central body reference frame. First, relative coordinates $\mathbf{q}_i$ can be defined with [59][60]

$$\mathbf{q}_i = \mathbf{r}_i - \mathbf{r}_1, \tag{8}$$

$$\mathbf{r}_{ij} = \mathbf{r}_j - \mathbf{r}_i = \mathbf{q}_j - \mathbf{q}_i = \mathbf{q}_{ij}, \tag{9}$$

$$\ddot{\mathbf{q}}_i = \ddot{\mathbf{r}}_i - \ddot{\mathbf{r}}_1. \tag{10}$$

From (10) and (6) it can be seen that

$$\ddot{\mathbf{q}}_i = \sum_{j=1, j\neq i}^{n} \mu_j \frac{\mathbf{q}_{ij}}{q_{ij}^3} - \sum_{j=2}^{n} \mu_j \frac{\mathbf{q}_j}{q_j^3} \quad (i = 2, 3, ..., n). \tag{11}$$

Simplifying leads to

$$\ddot{\mathbf{q}}_i = \frac{\mathbf{q}_{i1}}{q_{i1}^3}\mu_1 - \frac{\mathbf{q}_i}{q_i^3}\mu_i + \sum_{j=2, j\neq i}^{n} \mu_j \left(\frac{\mathbf{q}_{ij}}{q_{ij}^3} - \frac{\mathbf{q}_j}{q_j^3} \right) \quad (i = 2, 3, ..., n), \tag{12}$$

and with

$$\begin{aligned} \mathbf{q}_{i1} &= \mathbf{q}_1 - \mathbf{q}_i = \mathbf{r}_1 - \mathbf{r}_i, \\ \Rightarrow -\mathbf{q}_{i1} &= \mathbf{r}_i - \mathbf{r}_1 = \mathbf{q}_i, \end{aligned}$$

(12) may be further simplified to [59][60]

$$\ddot{\mathbf{q}}_i = -\frac{\mu_1 + \mu_i}{q_i^3}\mathbf{q}_i + \sum_{j=2, j\neq i}^{n} \mu_j \left(\frac{\mathbf{q}_{ij}}{q_{ij}^3} - \frac{\mathbf{q}_j}{q_j^3} \right) \quad (i = 2, 3, ..., n). \tag{13}$$

Let $\mathbf{q}_r$ be the relative position of the spacecraft with respect to the central body reference frame. Furthermore, let μ_1 be the gravitational parameter of the central body with the assumption that the spacecraft mass can be neglected in comparison with the central body mass, $\mu_r << \mu_1$. When modeling the force environment of the system, forces on the spacecraft arising from celestial bodies are considered while forces on the celestial bodies arising from the spacecraft are ignored [10]. Therefore, (13) further simplifies to

$$\ddot{\mathbf{q}}_r = \underbrace{-\frac{\mu_1}{q_r^3}\mathbf{q}_r}_{\text{central body acceleration}} + \underbrace{\sum_{j=2, j\neq r}^{n} \mu_j \left(\frac{\mathbf{q}_j - \mathbf{q}_r}{|\mathbf{q}_j - \mathbf{q}_r|^3} - \frac{\mathbf{q}_j}{q_j^3} \right)}_{\text{perturbing acceleration}}, \tag{14}$$

whereby the gravitational influence of the central body μ_1 can now be distinguished from the forces caused by gravitational parameters of perturbing bodies μ_j. In [10] and [98], methods can be found where the reference body's ephemeris were generated using

more than point mass gravitational modeling, such as a general relativistic framework as well as the solar quadrupole moment.

Note, that in (14) the term for a central body is still assumed to be valid only for a point mass. However, one of the main goals in this work is to precisely determine the gravitational field of this central body. Thus, the influence of higher-order terms arising from an inhomogeneous gravitational potential can no longer be neglected.

Hence. in the following subsection, the characterization of a gravitational potential using spherical harmonics will be discussed.

2.2.3. Gravitational Potential

In potential theory, solutions to Laplace's equation

$$\Delta V = 0 \tag{15}$$

are subject to a broad spectrum of scientific topics in gravitation, electrostatics, fluid dynamics, and general physics. They are called harmonic functions. Laplace's equation is an elliptical, partial differential second-order equation. The Laplace operator in Cartesian coordinates may be written as

$$\Delta = \nabla \cdot \nabla = \sum_{i=1}^{3} \frac{\partial^2}{\partial x_i^2}. \tag{16}$$

However, for the description of a gravitational field, it can be useful to describe the potential in spherical coordinates (Figure 12). The Laplace operator may then be written as [75]

$$\Delta\left(r, \theta, \varphi\right) = \frac{1}{r^2}\frac{\partial}{\partial r}\left(r^2 \frac{\partial}{\partial r}\right) + \frac{1}{r^2 \sin\theta}\frac{\partial}{\partial \theta}\left(\sin\theta \frac{\partial}{\partial \theta}\right) + \frac{1}{r^2 \sin^2\theta}\frac{\partial^2}{\partial \varphi^2}, \tag{17}$$

where $r \geq 0$, $\theta \in [0, \pi]$ and $\varphi \in [0, 2\pi]$. Functions that fulfill both (15) and (17) now describe the potential in spherical coordinates. Assume that the gravitational potential only depends on some value $r > 0$, but not on (θ, φ). Now, the angular part

of the equation will vanish, and all spherical surfaces become equipotential. Laplace's equation simplifies to [61]

$$\Delta V\left(r\right)=\frac{1}{r^{2}}\frac{\partial}{\partial r}\left(r^{2}\frac{\partial V\left(r\right)}{\partial r}\right)=0, \tag{18}$$

which yields the first nontrivial solution to the potential problem,

$$V(r)=\frac{GM}{r}, \tag{19}$$

where M is mass of the attracting body. This relationship is well known from the two-body problem. Considering the Rosetta-mission, with increasing target distance, at some point the influence of the angular terms in (17) becomes too small to be measured. Therefore, the comet appears as a point mass when the spacecraft orbit is too far away and the orbit solution fulfills (18). For this reason, when searching for a measurable influence of the angular terms, special attention must be given to the closer orbits, where higher-order terms of the gravitational potential become more pronounced and may be measured. They are described in spherical harmonics, which will be discussed in the following section.

2.2.4. Spherical Harmonics

It can be shown that spherical harmonics of degree l are a solution of the angular part $\Delta\left(\theta,\varphi\right)$ in (17). They can be written as [85]

$$K_{lm}\left(r,\theta,\varphi\right)=\left(\frac{s}{r}\right)^{l}P_{lm}\left(\cos\theta\right)\left(C_{lm}\cos\left(m\varphi\right)+S_{lm}\sin\left(m\varphi\right)\right), \tag{20}$$
$$l=(0,1,..,\infty),\ m=(0,..,l),\ r>s.$$

Here, P_{lm} are called associated Legendre polynomials. They are defined as [85]

$$P_{lm}(u)=\left(1-u^{2}\right)^{\frac{m}{2}}\frac{\mathrm{d}^{m}}{\mathrm{d}u^{m}}P_{l}(u), \tag{21}$$

with the Legendre polynomial of degree l

$$P_l(u) = \frac{1}{2^l l!} \frac{\mathrm{d}^l}{\mathrm{d}u^l} \left(u^2 - 1\right)^l, \tag{22}$$

where u is the cosine of θ as defined in Figure 12. The scalars C_{lm} and S_{lm} in (20) are called gravitational potential coefficients. Radius s defines the Brillouin-Sphere, which encloses the target body with value $R_\oplus$. In this work, $R_\oplus$ is the distance of the surface point that is farthest away from the target body's center of gravity.

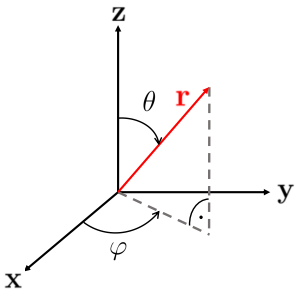

Figure 12: The angles defining a spherical coordinate system.

In Figure 13, Spherical Harmonics are illustrated up to degree $l = 4$ on the Brillouin-Sphere ($r = s$) with $C_{lm} = 1,\ S_{lm} = 0$ for all gravitational potential coefficients [61][85].

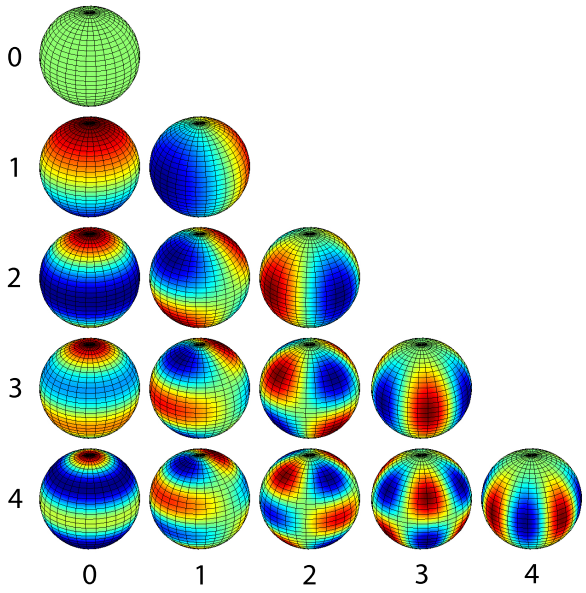

Figure 13: Spherical harmonics up to degree $l = 4$ from top to bottom, order m left to right [61].

Since the Laplace operator is linear, the radial and angular part of solutions to (17) may be summarized to a linear combination of basis functions. Thus, the gravitational potential of an arbitrary shaped body is written as a spherical harmonics expansion [85]

$$V(r,\theta,\varphi) = \frac{GM_\oplus}{r}\sum_{l=0}^{\infty}\sum_{m=0}^{l}\left(\frac{R_\oplus^l}{r^l}\right)P_{lm}\left(\cos\theta\right)\left(C_{lm}\cos\left(m\varphi\right)+S_{lm}\sin\left(m\varphi\right)\right). \tag{23}$$

In this way, the true potential of the body is approximated by a series of potential functions. Note, that the gravitational potential coefficients C_{lm} and S_{lm} contain the information of the inner mass distribution of the target body inside the Brillouin-Sphere. Assuming, that the density distribution $\rho(\mathbf{s})$ of the target body is known, the coefficients can be obtained from [85]

$$C_{lm} = \frac{2-\delta_{0m}}{M_\oplus}\frac{(l-m)!}{(l+m)!}\int\frac{s^l}{R_\oplus^l}P_{lm}\left(\cos\theta\right)\cos\left(m\varphi\right)\rho(\mathbf{s})\mathrm{d}V, \tag{24}$$

$$S_{lm} = \frac{2-\delta_{0m}}{M_\oplus}\frac{(l-m)!}{(l+m)!}\int\frac{s^l}{R_\oplus^l}P_{lm}\left(\cos\theta\right)\sin\left(m\varphi\right)\rho(\mathbf{s})\mathrm{d}V, \tag{25}$$

$$\text{where } \delta_{ij} = \begin{cases} 1 & \text{if } i=j, \\ 0 & \text{else.} \end{cases}$$

For the Rosetta mission, the density distribution of the target body was unknown prior to the arrival of the Orbiter. However, as previously introduced, the spacecraft orbit is determined by the influence of the irregularly shaped comet's gravitational potential. Hence, for a given expansion of Spherical Harmonics, a spacecraft trajectory around the comet may be integrated and compared to the measured one. Therefore, in an iterative process, gravitational potential coefficients C_{lm} and S_{lm} in (23) can be estimated up to a certain degree l and order m. This allows one to better understand the inner structure of the comet. The more gravitational potential coefficients can be determined, the more detailed information about mass distribution and inner structure can be revealed [61].

Since gravitational potential coefficients may cover wide orders of magnitude, it is favorable to describe the gravitational field with normalized coefficients $\bar{C}_{lm}$ and $\bar{S}_{lm}$; they may be obtained from [85]

$$\begin{bmatrix} \bar{C}_{lm} \\ \bar{S}_{lm} \end{bmatrix} = \sqrt{\frac{(l+m)!}{(2-\delta_{0m})\,(2l+1)\,(l-m)!}} \begin{bmatrix} C_{lm} \\ S_{lm} \end{bmatrix}. \tag{26}$$

The associated Legendre polynomials may be normalized as well with

$$\bar{P}_{lm} = \sqrt{\frac{(2-\delta_{0m})\,(2l+1)\,(l-m)!}{(l+m)!}} P_{lm}. \tag{27}$$

2.2.5. Gravitational Potential Coefficients and Moments of Inertia

In general, the gravitational potential of an arbitrary shaped body can be derived from its density distribution inside the body's volume via [85]

$$V(\mathbf{r}) = G \int \frac{\rho(\mathbf{s})\mathrm{d}V}{\|\mathbf{r}-\mathbf{s}\|}. \tag{28}$$

Regarding this density distribution, some special gravitational potential coefficients are predetermined. First, it can be shown that

$$\frac{2-\delta_{0m}}{M_\oplus}\frac{(l-m)!}{(l+m)!} = \frac{1}{M_\oplus} \text{ for } l = m = 0, \tag{29}$$

$$C_{00} = \frac{1}{M_\oplus} \int \frac{s^0}{R_\oplus^0} P_{00}\left(\cos\theta\right) \cos 0 \rho(\mathbf{s})\mathrm{d}V = \frac{1}{M_\oplus} \int \rho(\mathbf{s})\mathrm{d}V = 1. \tag{30}$$

Furthermore, one finds that

$$C_{10} = \frac{1}{M_\oplus R_\oplus} \int s\left(\cos\theta\right) \rho(\mathbf{s})\mathrm{d}V = \frac{1}{M_\oplus R_\oplus} \int z\rho(\mathbf{s})\mathrm{d}V = \frac{z_0}{R_\oplus}, \tag{31}$$

$$C_{21} = \frac{2}{6M_\oplus R_\oplus^2} \int 3s^2 \cos\theta \sin\theta \cos\left(\varphi\right) \rho(\mathbf{s})\mathrm{d}V \tag{32}$$

$$= \frac{1}{M_\oplus R_\oplus^2} \int xz\rho(\mathbf{s})\mathrm{d}V = -\frac{I_{xz}}{M_\oplus R_\oplus^2}. \tag{33}$$

Accordingly, one can write

$$C_{11} = \frac{x_0}{R_\oplus},\ S_{21} = -\frac{I_{yz}}{M_\oplus R_\oplus^2}, \tag{34}$$

$$S_{11} = \frac{y_0}{R_\oplus},\ S_{22} = -\frac{I_{xy}}{2M_\oplus R_\oplus^2}. \tag{35}$$

Thus, the coefficients C_{10}, C_{21}, C_{11}, S_{11}, S_{21}, S_{22} only depend on the body's mass, the Brillouin-Sphere, the center of mass and the off-diagonal elements in the moment of inertia tensor. Hence, if the body-fixed coordinate system is defined with its origin in the center of mass of the target body and the axes are co-aligned with its main axes of inertia, all six coefficients vanish, since $[x_0, y_0, z_0] = \mathbf{0}$ and $[I_{xz}, I_{yz}, I_{xy}] = \mathbf{0}$. It becomes obvious, that gravitational potential coefficients are closely related to the body's moments of inertia, which will become important in section 4.

Finally, if $m = 0$, $\sin(m\varphi)$ vanishes and with (25) one finds that $S_{l0} = 0\ \forall\ l$. Additional information about the description of a gravitational potential can be found in [3][85][61].

2.2.6. Recursion Formulation of the Legendre Polynomials

The associated Legendre polynomials may be determined from a recursion. Beginning from $P_{00} = 1$, one may write P_{mm} up to the desired highest degree by [85]

$$P_{mm}(u) = (2m-1)\left(1-u^2\right)^{\frac{1}{2}} P_{m-1,m-1}. \tag{36}$$

Now, with

$$P_{m+1,m}(u) = (2m+1)\, uP_{mm}(u) \tag{37}$$

and

$$P_{lm}(u) = \frac{1}{l-m}\left((2l-1)\, uP_{l-1,m}(u) - (l+m-1)\, P_{l-2,m}(u)\right) \tag{38}$$

the remaining polynomials may be determined for $l > m+1$. In Table 2, the first six associated Legendre polynomials may be seen.

l	**m**	$P_{lm}(u)$	$P_{lm}(\cos\theta)$
0	0	1	1
1	0	u	$\cos\theta$
1	1	$(1-u^2)^{1/2}$	$\sin\theta$
2	0	$\frac{1}{2}(3u^2-1)$	$\frac{1}{2}(3\cos^2\theta-1)$
2	1	$3u(1-u^2)^{1/2}$	$3\cos\theta\sin\theta$
2	2	$3(1-u^2)$	$3\sin^2\theta$

Table 2: The first six associated Legendre polynomials [61].

2.3. Non-Gravitational Perturbing Forces

In this subsection, the non-gravitational forces that act on the spacecraft are described.

2.3.1. Solar Radiation Pressure

Solar radiation pressure has a significant influence on a spacecraft's trajectory and can, therefore, not be neglected in precise orbit determination. It results from the transfer of momentum through impact, reflection, absorption and re-emission of photons [103]. Generally, the force acting on a spacecraft through solar radiation pressure may be written as

$$F_R = \frac{\Delta p}{\Delta t} = \frac{q_s}{c} A, \tag{39}$$

where Δp is the transferred impulse during time interval Δt. The force equals the solar flux q_s that passes the spacecraft area A divided by c, the speed of light. However, this model is only valid with the assumption that all photons are absorbed by a surface that is oriented perpendicular to the Sun. Ultimately, a more detailed model considers an inclined surface and, accordingly distinguishes absorption from reflection in the respective fractions of solar radiation. The reflected portion of the radiation may then further be subdivided into diffuse and specular reflection. The corresponding spacecraft accelerations caused by absorption and the two types of reflection are written as

$$\ddot{\mathbf{r}}_{\mathrm{a}} = -\frac{q_s}{c}\cos\left(\vartheta_{\mathrm{inc}}\right)\frac{A}{m_{\mathrm{sc}}}\mathbf{e}_{\odot}, \tag{40}$$

$$\ddot{\mathbf{r}}_{\mathrm{s}} = -\frac{2q_s}{c}\cos^2\left(\vartheta_{\mathrm{inc}}\right)\frac{A}{m_{\mathrm{sc}}}\mathbf{e}_{\mathrm{N}}, \tag{41}$$

$$\ddot{\mathbf{r}}_{\mathrm{d}} = -\frac{q_s}{c}\cos\left(\vartheta_{\mathrm{inc}}\right)\frac{A}{m_{\mathrm{sc}}}\left(\mathbf{e}_{\odot} + \frac{2}{3}\mathbf{e}_{\mathrm{N}}\right), \tag{42}$$

where $\mathbf{e}_{\odot}$ denotes the unit vector towards the Sun and $\mathbf{e}_{\mathrm{N}}$ is the surface normal of the exposed surface A. The spacecraft mass is given as m_{sc} and ϑ_{inc} denotes the angle of radiation incidence relative to the affected surface. The three contributions can be linearly combined by using coefficients ϕ_i to describe the fraction of the respective type of acceleration and setting $\sum_i \phi_i \stackrel{!}{=} 1$. Hence, one can write

$$\ddot{\mathbf{r}} = -k\frac{r_0^2 q_s A}{r_{\odot}^2 m_{\mathrm{sc}} c}\cos\left(\vartheta_{\mathrm{inc}}\right)\left(\left(\phi_1 + \phi_2\right)\mathbf{e}_{\odot} + 2\left(\phi_3\cos\left(\vartheta_{\mathrm{inc}}\right) + \frac{\phi_2}{3}\right)\mathbf{e}_{\mathrm{N}}\right). \tag{43}$$

where $r_{\odot}$ denotes the spacecraft distance from the Sun and r_0 is 1 AU. With the assumption that the surface normal points straight towards the Sun, one may simplify (43) to

$$\ddot{\mathbf{r}} = -k\frac{r_0^2 q_s A}{r_{\odot}^2 m_{\mathrm{sc}} c}\mathbf{e}_{\odot}, \tag{44}$$

which leads, however, to a decreased accuracy in the orbit prediction. Since the activity of the Sun changes the magnitude of solar flux, a scaling factor k is introduced and adjusted as a parameter in orbit determination. Starting from 2016-08-15T09:00:13 UTC, solar radiation pressure caused a perturbing acceleration of the spacecraft of 2.31×10^{-11}km s^{-2}, decreasing to 2.04×10^{-11}km s^{-2} towards the end of the mission. More detailed information about solar radiation pressure and its influence on orbit determination may be found in [85][3][103][36].

2.3.2. Outgassing

Another important non-gravitational perturbing force that must be considered for the Rosetta mission is outgassing. Especially during close flybys, precise coma drag mod-

eling is probably the most difficult part of orbit prediction around the comet. The outgassing flow has measurable influence on the trajectory of the spacecraft and, therefore, cannot be neglected. However, cometary activity in general is difficult to predict. The direction of the cometary gas species flow as well as the density and velocity shows diurnal variations throughout the mission. Additionally, outbursts (Figure 14) eject cometary dust and remain active for several minutes and up to a few hours [77].

Figure 14: An Osiris-Nac image showing an outburst in July 2015. Copyright: ESA/Rosetta/MPS for Osiris Team MPS/UPD/LAM/IAA/SSO/INTA/UPM/DASP/IDA – CC BY-SA 4.0

These physical processes are driven by the complex shape of the cometary nucleus and depend on sunlight illumination angle, duration, as well as heliocentric distance. Fortunately, the activity decreases with an increasing distance from the Sun. Since very close orbits - which are most important for the estimation of the gravitational field of the comet - were flown either at the beginning or towards the end of the mission, cometary activity was moderate. However, the orbit perturbation of the outgassing flow still must be considered for a precise orbit reconstruction. In general, the drag acceleration caused by the cometary outgassing may be written as

$$\ddot{\mathbf{r}} = \frac{C_D}{2m_{\text{sc}}} \rho v \mathbf{v} A, \tag{45}$$

where m_{sc} denotes the spacecraft mass, ρ and $v = \|\mathbf{v}\|_2$ are the density and relative velocity of the atmosphere and A is the affected area of the spacecraft with respect to the velocity vector $\mathbf{v}$. Starting from 2016-08-15T09:00:13 UTC, outgassing caused a perturbing acceleration of the spacecraft up to 1.59×10^{-11}km s^{-2}. More detailed information about the cometary outgassing and different model approaches can be found in [48][11][65][70][109][69][13][88][44][7].

2.4. Prediction of Doppler Shift

In this work, Doppler data received from the Rosetta spacecraft is simulated. Hence, a brief overview of the related theory will be given. More in depth derivations can be found within the given references.

2.4.1. Radio Link

Let $\mathbf{n}$ be the unit vector from the position of a transmitter at transmission time t_T to the position of a receiver at receiving time t_R. Furthermore, let $\boldsymbol{\Psi}_R = \frac{\mathbf{v}_R}{c}$ and $\boldsymbol{\Psi}_T = \frac{\mathbf{v}_T}{c}$ be the normalized velocity of the receiver and transmitter at the respective point in time. Then, the relativistic Doppler effect is obtained from [53][85][3][60][55]

$$\frac{\Delta f}{f_0} = 1 - \frac{1 - \mathbf{n} \cdot \boldsymbol{\Psi}_R + \frac{1}{2} \|\boldsymbol{\Psi}_R\|_2^2 - \frac{\Phi_R}{c^2}}{1 - \mathbf{n} \cdot \boldsymbol{\Psi}_T + \frac{1}{2} \|\boldsymbol{\Psi}_T\|_2^2 - \frac{\Phi_T}{c^2}}, \tag{46}$$

where Φ_R and Φ_T denote the gravitational potential in the sphere of influence where the receiver and the transmitter are located. If the receiver is located on the Earth, the gravitational potential may be approximated via $\Phi_R = -\frac{\mu_\odot}{r_\odot} - \frac{\mu_E}{r_E}$, where $r_\odot$ denotes the distance of the receiver to the Sun and r_E the distance to the Earth respectively. Since the receiver on the surface of the Earth is located in a non-inertial rotating system, the potential by centrifugal acceleration must also be considered with [53][60][3]

$$\Phi_Z = -\frac{1}{2}\left(\omega_{\oplus} sin\left(\frac{\pi}{2} - \varphi\right) r_E\right)^2, \tag{47}$$

where $\omega_{\oplus}$ denotes the angular velocity of the Earth and φ the geographical latitude of the receiving ground station.

2.4.2. Relativity

As mentioned before in (46), normalized velocities need to be determined by summation in barycentric and planetocentric reference frames. The velocity in the system S may be determined through **relativistic summation** via [25][60][3]

$$\mathbf{v} = \frac{1}{\gamma(1 + \mathbf{\Psi}_u \cdot \mathbf{\Psi}_{v'})} \cdot \left[\mathbf{v}' + (\gamma - 1) \cdot (\mathbf{v}' \cdot \tilde{\mathbf{u}}) \cdot \tilde{\mathbf{u}} + \gamma \cdot \mathbf{u}\right], \tag{48}$$

where $\tilde{\mathbf{u}}$ is the unit vector of the velocity $\mathbf{u}$ of system S' relative to system S, and $\mathbf{\Psi}_u$ is $\frac{\mathbf{u}}{c}$ analogous to the definitions in (46). Accordingly, $\mathbf{\Psi}_{v'}$ denotes the normalized velocity $\frac{\mathbf{v}'}{c}$ of the body in system S'. γ is known as the **Lorentz term** and is defined as [3]

$$\gamma = \frac{1}{\sqrt{1 - \|\mathbf{\Psi}_u\|_2^2}}. \tag{49}$$

2.4.3. Effects from the Location of the Ground Station

The location of the ground station on the surface of the Earth has a significant influence on the measured Doppler shift. The RSI established method of mass estimation covers a wide spectrum of modeling effects that influence the position of the antenna and, in that way, allows for precise orbit determination [3][85][8] [54].

In order to obtain residuals in the prediction of Doppler shift down to only a few millihertz, the position of the ground station in the celestial reference frame must be known accurately. First, for the transformation from the ITRF into the ICRF, effects caused by **precession, nutation, Earth rotation and polar motion** need to be modeled precisely.

Additionally, the displacement of the ground station within the ITRF caused by

Tectonic plate motion is approximated by a linear model, since the crust of the Earth is not invariable. On top of this, **site displacement due to solid Earth tides** arising from the gravitational attraction of bodies external to Earth are described and predicted. They cause a nonlinear deformation of the planet's shape and, as a result, induce an additional displacement of the receiver depending on the time of measurement. Other effects like ocean loading, pole tides, atmospheric loading, thermal deformation of the antenna, and post glacial rebound are in the order of magnitude of a few centimeters or even millimeters. These effects are neglected and not considered in the ground station model.

Another important effect that must be considered is the influence of the atmosphere the signal travels through. Molecules, atoms, ions, and electrons in the atmosphere are known to cause interactions with electromagnetic radiation in terms of direction, velocity, polarization, and strength of the respective signal. Thus, one main interfering impact on the two-way-radio link is a **path delay** caused by the reduced speed of light in the atmosphere in comparison to the speed of light in vacuum. The subsequently raised **changes in frequency** need to be removed from the received data to obtain the pure changes in spacecraft velocity out of a Doppler shift. Here, contributions caused by the **troposphere** and the **ionosphere** must be distinguished.

All models, methods and approximations used to describe the interference effects that arise from the position of the receiver on Earth can be found in [85][3]. In these documents, a detailed overview of all implementations is given. Since this work is considered to be an extension of the already established method of RSI, these methods will not be discussed at a greater level of detail here.

2.5. Principles of Projective Geometry

A key topic of this work is the estimation of relative geometry from optical data. An in-depth overview of the related theory will be given in this subsection. The definitions, terms and equations are mainly taken from [52].

2.5.1. Homogeneous Representation of Lines

Homogeneous lines and points are important quantities in projective geometry. A homogeneous line in $\mathbb{R}^2$ may be written as [52]

$$ax + by + c = 0. \tag{50}$$

Note, that in this notation $ax+by+c=0$ and $kax+kby+kc=0$ represent the same line. Thus, any vector

$$k\,(a,b,c)^{\mathsf{T}}\,, \quad \forall k \neq 0 \tag{51}$$

represents an equivalence class known as homogeneous vectors [52].

2.5.2. Homogeneous Representation of Points

Since the point $\mathbf{x} = (x,y)^{\mathsf{T}} \in \mathbb{R}^2$ can only be a subset to the homogeneous line $\mathbf{l} = (a,b,c)^{\mathsf{T}}$ if the condition $ax + by + c = 0$ is fulfilled, one may choose the representation [52]

$$(x,y,1)\,(a,b,c)^{\mathsf{T}} = (x,y,1)\,\mathbf{l} \stackrel{!}{=} 0. \tag{52}$$

In this notation, the point $\mathbf{x} = (x,y)^{\mathsf{T}} \in \mathbb{R}^2$ is expressed in **homogeneous coordinates**. Note, that for any non-zero scalar k one may write [52]

$$(kx,ky,k)\,\mathbf{l} = 0. \tag{53}$$

Hence, the homogeneous vector $\mathbf{x} = (x_1,x_2,x_3)^{\mathsf{T}} \in \mathbb{R}^3$ represents the point $\left(\frac{x_1}{x_3},\frac{x_2}{x_3}\right)^{\mathsf{T}} \in \mathbb{R}^2$ [52]. This notation is often needed in conjunction with projective space and will be used throughout this document.

2.5.3. Camera Matrix

The camera matrix may generally be written in the form

$$\mathrm{P} = \begin{bmatrix} p_{11} & p_{12} & p_{13} & p_{14} \\ p_{21} & p_{22} & p_{23} & p_{24} \\ p_{31} & p_{32} & p_{33} & p_{34} \end{bmatrix} = \begin{bmatrix} \mathbf{p}^{1\mathsf{T}} \\ \mathbf{p}^{2\mathsf{T}} \\ \mathbf{p}^{3\mathsf{T}} \end{bmatrix}. \tag{54}$$

It can be decomposed into a product of matrices as explained in the following. Starting with the most simple case by using the basic pinhole camera model, a point in space $\mathbf{X}_{\text{cam}} = (X, Y, Z)^{\mathsf{T}}$ defined in the camera coordinate frame is mapped to the point $\mathbf{x}$ that lies on the image plane where a line between the point $\mathbf{X}_{\text{cam}}$ and the camera center $\mathbf{c}$ meets the image plane [52].

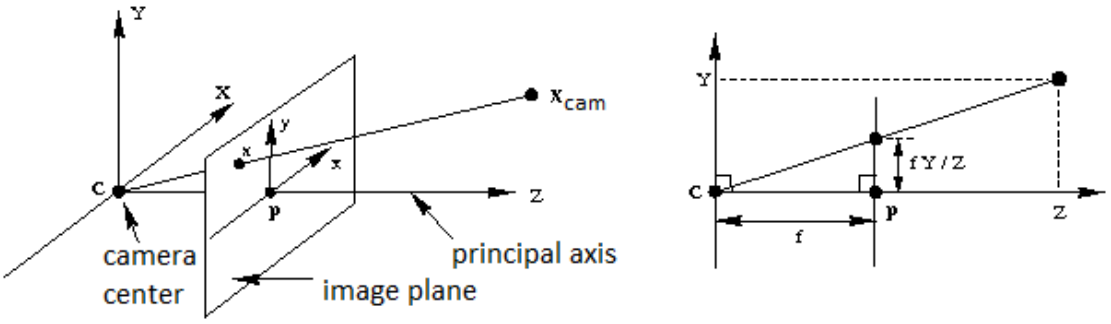

Figure 15: Reprojection of point $\mathbf{X}_{\text{cam}}$ into the image plane [52].

It may be seen from Figure 15 that the point $(X, Y, \mathrm{Z})^{\mathsf{T}}$ is mapped to $\left(f\frac{X}{Z}, f\frac{Y}{Z}, f\right)^{\mathsf{T}}$. By ignoring the final image coordinate f for this case, one obtains the central projection mapping from world to image coordinates

$$(X, Y, Z)^{\mathsf{T}} \longmapsto \left(f\frac{X}{Z}, f\frac{Y}{Z}\right)^{\mathsf{T}}, \tag{55}$$

which is a mapping from Euclidean 3-space $\mathbb{R}^3$ to Euclidean 2-space $\mathbb{R}^2$. The **camera center** is also called the **center of projection** or optical center. The line perpendicular to the image plane that joins the camera center is called the **principal axis** or **principal ray** (Figure 15). This principal axis meets the image plane at the **principal point p**. When using homogeneous vectors in the description of projective geometry, then central projection as seen in the subsection before may be expressed as [52]

$$\begin{pmatrix} fX \\ fY \\ Z \end{pmatrix} = \begin{bmatrix} f & 0 & 0 & 0 \\ 0 & f & 0 & 0 \\ 0 & 0 & 1 & 0 \end{bmatrix} \begin{pmatrix} X \\ Y \\ Z \\ 1 \end{pmatrix}, \tag{56}$$

where the world point $\mathbf{X}_{\text{cam}}$ is represented as a homogeneous 4-d-vector $(X, Y, Z, 1)^{\mathsf{T}}$, $\mathbf{x}$ is a homogeneous 3-d-vector, and P is the 3×4 homogeneous camera projection matrix, compactly written as

$$\begin{aligned} \mathbf{x} &= \mathrm{P}\mathbf{X}_{\text{cam}}, \\ \mathrm{P} &= \operatorname{diag}(f, f, 1) \left[\begin{array}{c|c} \mathrm{I} & \mathbf{0} \end{array} \right]. \end{aligned} \tag{57}$$

2.5.4. Calibration Matrix

Assuming, that the coordinates of the image origin are not at the principal point, then the mapping (55) is amended by the offset $(p_x, p_y)^{\mathsf{T}}$, and one may write

$$(X, Y, Z)^{\mathsf{T}} \longmapsto \left(f\frac{X}{Z} + p_x, f\frac{Y}{Z} + p_y \right)^{\mathsf{T}}, \tag{58}$$

where $(p_x, p_y)^{\mathsf{T}}$ denotes the coordinates of the **principal point** in world coordinates and $(x_0, y_0)^{\mathsf{T}}$ in pixel coordinates, respectively (Figure 16).

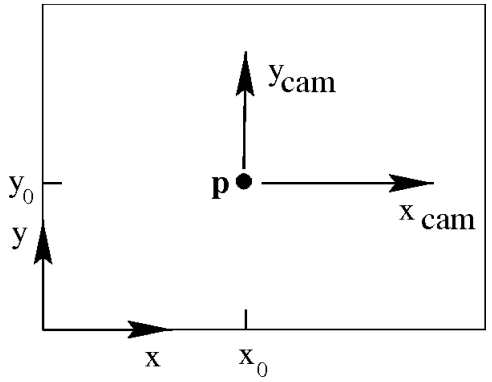

Figure 16: Definition of the principal point [52].

Expression (56) may now be written in its homogeneous notation [52]

$$\begin{pmatrix} fX + Zp_x \\ fY + Zp_y \\ Z \end{pmatrix} = \begin{bmatrix} f & 0 & p_x & 0 \\ 0 & f & p_y & 0 \\ 0 & 0 & 1 & 0 \end{bmatrix} \begin{pmatrix} X \\ Y \\ Z \\ 1 \end{pmatrix}, \tag{59}$$

and further decomposed by

$$\mathbf{x} = \mathrm{K} \left[\, \mathrm{I} \, \middle| \, \mathbf{0} \, \right] \mathbf{X}_{\mathrm{cam}}, \tag{60}$$

with the **calibration matrix**

$$\mathrm{K} = \begin{bmatrix} f & 0 & p_x \\ 0 & f & p_y \\ 0 & 0 & 1 \end{bmatrix}. \tag{61}$$

In this notation, the image coordinates are expressed in the same units as the world coordinates. However, in a practical application, the coordinates of key points are measured in pixel dimensions, which means that the pixel size of a CCD camera needs to be taken into account. Assume, that the number of pixels per unit distance in image coordinates is m_x and m_y in the respective coordinate directions. As a result, the calibration matrix becomes [52]

$$\mathrm{K} = \begin{bmatrix} \alpha_x & 0 & x_0 \\ 0 & \alpha_y & y_0 \\ 0 & 0 & 1 \end{bmatrix}, \tag{62}$$

where the entries $a_x = fm_x$, $a_y = fm_y$, $x_0 = m_x p_x$ and $y_0 = m_y p_y$ are now expressed in terms of pixel coordinates.

2.5.5. Camera Position and Pointing

Up to this point, the notation $\mathbf{X}_{\text{cam}}$ was used to clarify that the camera is located at the origin of a Euclidean coordinate system where the principal axis points down the Z-axis. This coordinate system will be called **camera coordinate frame** throughout this document. However, for a multiple view geometry application, it is useful to describe the world points in a fixed **world coordinate frame**, where the camera is defined by its respective camera matrix related via a non-homogeneous translation $\widetilde{\mathbf{C}}$ and a rotation R (Figure 17).

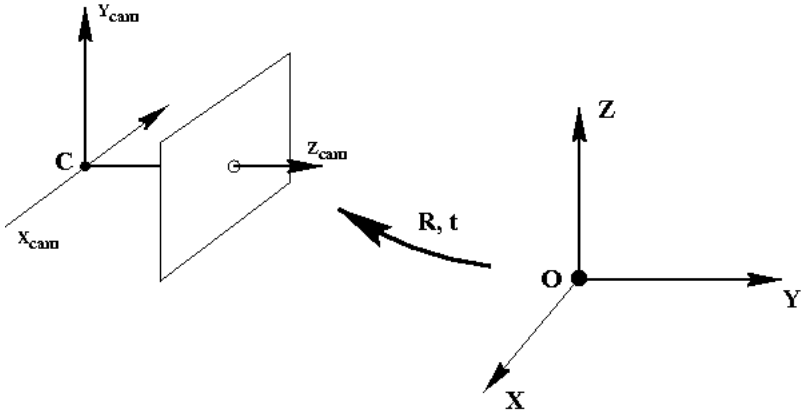

Figure 17: Rotation and translation of the camera reference frame [52].

Presupposing that $\widetilde{\mathbf{X}}$ is a non-homogeneous coordinate of a 3D-world point and $\widetilde{\mathbf{X}}_{\text{cam}}$ denotes the same point in a translated and rotated camera coordinate frame, then one may write

$$\widetilde{\mathbf{X}}_{\text{cam}} = \mathrm{R}\left(\widetilde{\mathbf{X}} - \widetilde{\mathbf{C}}\right). \tag{63}$$

This relation can also be expressed in its homogeneous form as [52]

$$\mathbf{X}_{\text{cam}} = \begin{bmatrix} \mathrm{R} & -\mathrm{R}\widetilde{\mathbf{C}} \\ 0 & 1 \end{bmatrix} \begin{pmatrix} X \\ Y \\ Z \\ 1 \end{pmatrix} = \begin{bmatrix} \mathrm{R} & -\mathrm{R}\widetilde{\mathbf{C}} \\ 0 & 1 \end{bmatrix} \mathbf{X}. \tag{64}$$

Combined with (60), one can write [52]

$$\mathbf{x} = \mathrm{KR}\left[\ \mathrm{I}\ \middle|\ -\widetilde{\mathbf{C}}\ \right]\mathbf{X}, \tag{65}$$

with $\mathbf{X}$ now being expressed in the world coordinate frame. It may be observed that the pinhole camera model has nine degrees of freedom: three for K, three for R, and three for $\widetilde{\mathbf{C}}$. These degrees of freedom are subdivided into internal camera parameters, which are contained in K, as well as external camera parameters, contained in the camera orientation R and in the non homogeneous position $\widetilde{\mathbf{C}}$. To further shorten the notation for the camera matrix, one may define

$$\mathbf{t} \coloneqq -\mathrm{R}\widetilde{\mathbf{C}}, \tag{66}$$

which leads to the general notation for the camera matrix [52]

$$\mathrm{P} = \mathrm{K}\left[\ \mathrm{R}\ \middle|\ \mathbf{t}\ \right]. \tag{67}$$

This notation will be used throughout this document. Note that one important quantity for this work - the relative position $\widetilde{\mathbf{C}}$ of the camera - is included here and is thus a part of the camera matrix P.

2.5.6. Fundamental Matrix

If a feature is detected in two images, the point correspondence defines a plane by the two camera centers as well as the point on the cometary surface that is observed with both cameras (Figure 18). This plane is called the **epipolar plane**.

The line connecting the two camera centers $\mathbf{C_1}$ and $\mathbf{C_2}$ is called the **baseline**. As can be seen in Figure 19, this plane intersects with the respective image plane of both cameras. The resulting intersection line is called the **epipolar line**.

Note, that any point $\mathbf{X}$ that lies on the line connecting the camera center and the reprojection $\mathbf{x}$ in the left camera's image plane will be subset to this epipolar line as long as it is in the field of view of camera two.

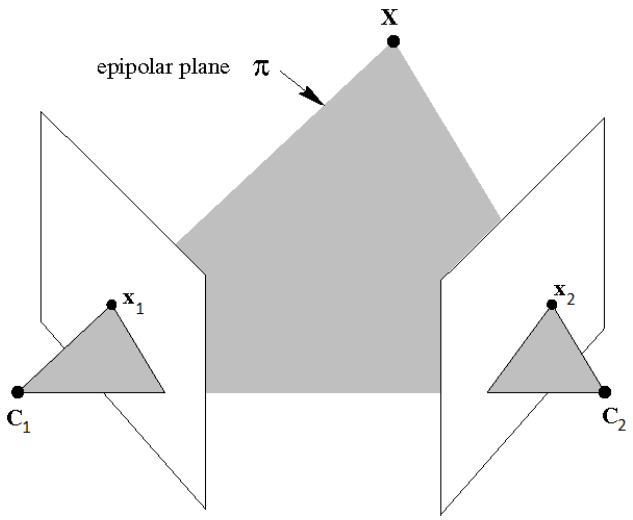

Figure 18: The epipolar plane π defined through the cometary surface point $\mathbf{X}$, and the two camera centers $\mathbf{C_1}$ and $\mathbf{C_2}$ with reprojections $\mathbf{x_1}$ and $\mathbf{x_2}$ [52].

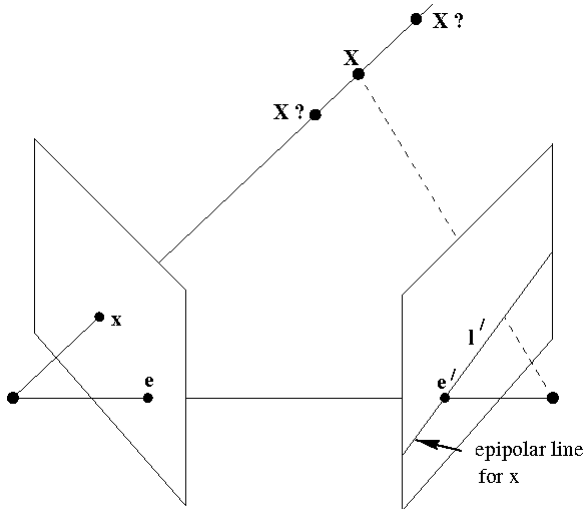

Figure 19: The epipolar line $\mathbf{l}'$ and epipoles $\mathbf{e}$ and $\mathbf{e}'$. Any reprojection of point $\mathbf{X}$ along the epipolar line $\mathbf{l}'$ in image two results in the same reprojection $\mathbf{x}$ in image one [52].

This geometric relationship (Figure 18) may be expressed algebraically via representation [52]

$$\mathbf{x}_2^{\mathsf{T}} \mathrm{F} \mathbf{x}_1 = 0, \tag{68}$$

where F is called the **fundamental matrix**, a 3×3 homogeneous matrix of rank 2. If

for a pair of cameras $(\mathrm{P}, \mathrm{P}')$ a fundamental matrix F can be found, then F^{T} describes the relation of the opposite pair $(\mathrm{P}', \mathrm{P})$. Furthermore, the corresponding epipolar lines may be obtained via $\mathbf{l}' = \mathrm{F}\mathbf{x}$ and $\mathbf{l} = \mathrm{F}^{\mathsf{T}}\mathbf{x}'$, where $\mathbf{l}'$ denotes the epipolar line in the second image defined by the point $\mathbf{x}$ in the first image as well as the opposite way, respectively. Assuming, that the pair of cameras is defined as

$$\mathrm{P}_1 = \mathrm{K}\left[\ \mathrm{I}\ \middle|\ \mathbf{0}\ \right] \quad , \quad \mathrm{P}_2 = \mathrm{K}\left[\ \mathrm{R}\ \middle|\ \mathbf{t}\ \right], \tag{69}$$

then the fundamental matrix may be obtained from

$$\mathrm{F} = \mathrm{K}^{-\mathsf{T}}\left[\mathbf{t}\right]_{\times}\mathrm{R}\mathrm{K}^{-1} = \mathrm{K}^{-\mathsf{T}}\mathrm{R}\left[\mathrm{R}^{\mathsf{T}}\mathbf{t}\right]_{\times}\mathrm{K}^{-1}, \tag{70}$$

where $\left[\mathbf{t}\right]_{\times}$ denotes a skew-symmetric matrix as described in appendix A.4. The full derivation can be found in [52].

2.5.7. Normalized Coordinates and Essential Matrix

If the calibration of a camera is known, then the image coordinates of a feature measured on the camera CCD may be converted into **normalized coordinates**. The idea of this approach is to remove all degrees of freedom that depend on the internal parameters of a camera from the related equations of epipolar geometry. Granting that a camera is defined as $\mathrm{P} = \mathrm{K}\left[\ \mathrm{R}\ \middle|\ \mathbf{t}\ \right]$ with the relation $\mathbf{x} = \mathrm{P}\mathbf{X}$, then the inverse of the calibration matrix may be applied to the image coordinates as

$$\hat{\mathbf{x}} = \mathrm{K}^{-1}\mathbf{x}, \tag{71}$$

with $\hat{\mathbf{x}}$ now being expressed in normalized coordinates. The camera matrix becomes $\mathrm{K}^{-1}\mathrm{P} = \left[\ \mathrm{R}\ \middle|\ \mathbf{t}\ \right]$ and is called a **normalized camera matrix**. The effects of the known calibration are now removed. For this case, the former **fundamental matrix** may be transformed via

$$\mathrm{E} = \mathrm{K}^{\mathsf{T}}\mathrm{F}\mathrm{K}, \tag{72}$$

and is now called an **essential matrix**. It is still a homogeneous quantity like the fundamental matrix. The relation between two independent measurements of the same 3D homogeneous world point now becomes

$$\hat{\mathbf{x}}_2^{\mathsf{T}}\mathrm{E}\hat{\mathbf{x}}_1 = 0, \tag{73}$$

equivalent to (68) but expressed in normalized coordinates [52]. If a pair of normalized camera matrices is defined as

$$\mathrm{P}_1 = \left[\ \mathrm{I}\ \middle|\ \mathbf{0}\ \right] \quad , \quad \mathrm{P}_2 = \left[\ \mathrm{R}\ \middle|\ \mathbf{t}\ \right], \tag{74}$$

the essential matrix may be obtained from

$$\mathrm{E} = [\mathbf{t}]_{\times}\,\mathrm{R} = \mathrm{R}\left[\mathrm{R}^{\mathsf{T}}\mathbf{t}\right]_{\times}, \tag{75}$$

respectively. Note that the images that have been processed in this work were always obtained from the same camera within one specific dataset. In other words, there are no tie point correspondences between two different camera systems, such as NAVCAM and OSINAC. Hence, unnecessary degrees of freedom can be removed from all contributing equations and algorithms. The notation of **normalized coordinates, normalized camera matrices, and essential matrices** will be used throughout this document and for all implemented software packages, respectively.

2.5.8. Essential Matrix Decomposition

The decomposition of an essential matrix into $\mathrm{E} = [\mathbf{t}]_{\times}\,\mathrm{R}$ may be used to find a camera position from optical data alone. In the case where insufficient a priori information about the spacecraft position relative to the target body is available, this technique may be used to obtain a first estimate of the camera's optical center position. From this point,

one may continue with a bundle adjustment technique as explained in subsection 3.2 to refine the result. Remember that the essential matrix is a product of a skew-symmetric matrix and a rotation matrix, $\mathrm{E} = [\mathbf{t}]_\times \mathrm{R}$. Now one can additionally define the matrices

$$\mathrm{Z} = \begin{bmatrix} 0 & 1 & 0 \\ -1 & 0 & 0 \\ 0 & 0 & 0 \end{bmatrix}, \quad \mathrm{W} = \begin{bmatrix} 0 & -1 & 0 \\ 1 & 0 & 0 \\ 0 & 0 & 1 \end{bmatrix}, \tag{76}$$

where Z is also skew-symmetric as $[\mathbf{t}]_\times$ and W is orthogonal as R, respectively. Another important property of an essential matrix is that two of its singular values are equal and the third one is zero. The respective proof can be found in [52]. Thus, the SVD of E may be written as

$$\mathrm{E} = \mathrm{U}\ \mathrm{diag}\,(1, 1, 0)\ \mathrm{V}^\mathsf{T}. \tag{77}$$

Now let S be any skew symmetric matrix. The block decomposition of a skew-symmetric matrix is $\mathrm{S} = \mathrm{UZU}^\mathsf{T}$, where U must be an orthogonal matrix. The corresponding proof can also be found in [52]. On the other hand, a rotation matrix may be decomposed as $\mathrm{R} = \mathrm{UR'V}^\mathsf{T}$, where R′ can be any arbitrary rotation matrix. Therefore, in order to extract $[\mathbf{t}]_\times$ and R from a given essential matrix E without any additional knowledge, all the above findings may be summarized as

$$\mathrm{E} = \mathrm{U}\ \mathrm{diag}\,(1, 1, 0)\ \mathrm{V}^\mathsf{T} = \mathrm{SR} = \left(\mathrm{UZU}^\mathsf{T}\right)\left(\mathrm{UR'V}^\mathsf{T}\right) = \mathrm{U}\,(\mathrm{ZR'})\,\mathrm{V}^\mathsf{T}. \tag{78}$$

With $\mathrm{ZR'} \stackrel{!}{=} \mathrm{diag}\,(1, 1, 0)$ and R′ being a rotation matrix, it follows that $\mathrm{R'} = \mathrm{W}$ or $\mathrm{R'} = \mathrm{W}^\mathsf{T}$ except for sign. Hence, one may summarize that if $\mathrm{E} = [\mathbf{t}]_\times \mathrm{R} = \mathrm{U}\ \mathrm{diag}\,(1, 1, 0)\ \mathrm{V}^\mathsf{T}$, then

$$[\mathbf{t}]_\times = \mathrm{UZU}^\mathsf{T}\ ,\ \mathrm{R} = \mathrm{UWV}^\mathsf{T} \text{ or } \mathrm{R} = \mathrm{UW}^\mathsf{T}\mathrm{V}^\mathsf{T}. \tag{79}$$

Presupposing that the first camera is set to $\mathrm{P}_1 = \left[\ \mathrm{I}\ \middle|\ \mathbf{0}\ \right]$, this leads to four possible solutions (Figure 20) for the second camera P_2, which are given as [52]

$$\begin{aligned} \mathrm{P}_2 = \left[\; \mathrm{U}\mathrm{W}\mathrm{V}^\mathsf{T} \;\middle|\; +\mathbf{u_3} \; \right] \text{ or } \left[\; \mathrm{U}\mathrm{W}\mathrm{V}^\mathsf{T} \;\middle|\; -\mathbf{u_3} \; \right] \\ \text{or } \left[\; \mathrm{U}\mathrm{W}^\mathsf{T}\mathrm{V}^\mathsf{T} \;\middle|\; +\mathbf{u_3} \; \right] \text{ or } \left[\; \mathrm{U}\mathrm{W}^\mathsf{T}\mathrm{V}^\mathsf{T} \;\middle|\; -\mathbf{u_3} \; \right], \end{aligned} \tag{80}$$

where $\mathbf{t}$ equals the third column of U, denoted as $\mathbf{u_3} = \mathrm{U}\,(0,0,1)^\mathsf{T}$ and stays undetermined in sign.

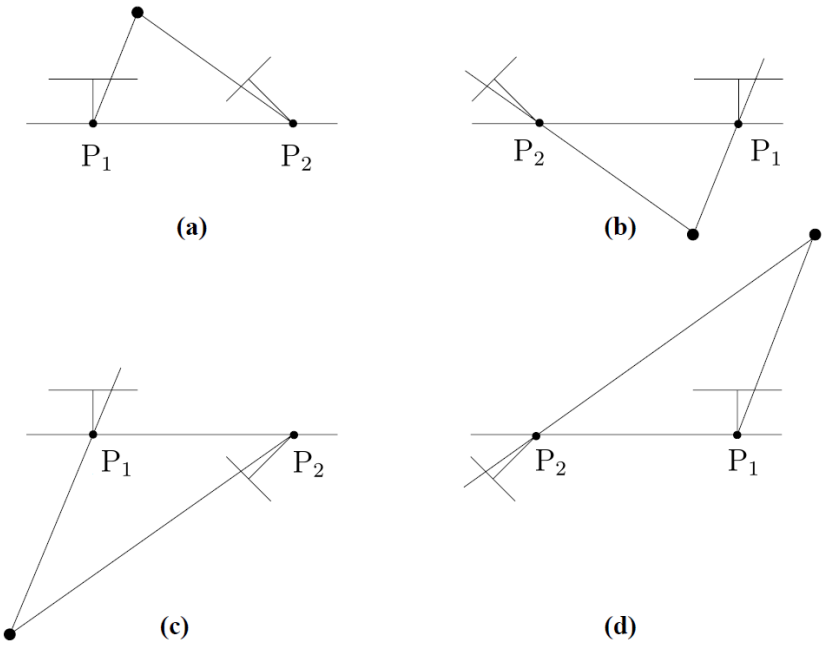

Figure 20: The decomposition of an essential matrix has four possible solutions for the camera matrices. Camera P_1 remains fixed, whereas camera P_2 has two possible rotations and translations according to (80). In the bottom row camera P_2 is rotated 180° about the baseline. Note that only in case **(a)** the tie point lies in front of both cameras; obviously, this should be the solution of choice [52].

Note that this set of equations is not unambiguous in sign and scale, which means that there are four possible solutions in geometry and even an infinite number of solutions in scale. Thus, if a reconstruction is attempted from optical data alone, additional constraints need to be defined. The full derivation of this subsection can be found in [52].

2.5.9. Triangulation

Linear triangulation is a good method for providing a first estimate in the 3D reconstruction process, despite knowing that it does not exactly satisfy geometric relations. However, it can be used as a starting point for **nonlinear triangulation** with higher precision or in order to provide initial values for **bundle adjustment**.

Let $\mathbf{X} \in \mathbb{R}^4$ be the homogeneous description of a point $\tilde{\mathbf{X}} \in \mathbb{R}^3$. Let $(\mathbf{x}, \mathbf{x}')$ be the corresponding measurements of $\mathbf{X}$ in two different images, described by the respective camera matrices $(\mathrm{P}, \mathrm{P}')$ with

$$\mathbf{x} = \mathrm{P}\mathbf{X}, \quad \mathbf{x}' = \mathrm{P}'\mathbf{X}. \tag{81}$$

Now, the cross product $\mathbf{x} \times (\mathrm{P}\mathbf{X}) = \mathbf{0}$ can be used to find three equations per tie point measurement. Writing the cross product out results in [52]

$$\begin{aligned} x\left(\mathbf{p}^{3\mathsf{T}}\mathbf{X}\right) - \left(\mathbf{p}^{1\mathsf{T}}\mathbf{X}\right) &= 0, \\ y\left(\mathbf{p}^{3\mathsf{T}}\mathbf{X}\right) - \left(\mathbf{p}^{2\mathsf{T}}\mathbf{X}\right) &= 0, \\ x\left(\mathbf{p}^{2\mathsf{T}}\mathbf{X}\right) - y\left(\mathbf{p}^{1\mathsf{T}}\mathbf{X}\right) &= 0, \end{aligned} \tag{82}$$

where $\mathbf{p}^{i\mathsf{T}}$ are the rows of P. In (82), two equations are linearly independent, respectively. After applying the same step to the second measurement $\mathbf{x}' = \mathrm{P}'\mathbf{X}$, the now combined system of four linearly independent equations may be solved from $\mathrm{A}\mathbf{X} = \mathbf{0}$ with

$$\mathrm{A} = \begin{bmatrix} x\mathbf{p}^{3\mathsf{T}} - \mathbf{p}^{1\mathsf{T}} \\ y\mathbf{p}^{3\mathsf{T}} - \mathbf{p}^{2\mathsf{T}} \\ x'\mathbf{p}'^{3\mathsf{T}} - \mathbf{p}'^{1\mathsf{T}} \\ y'\mathbf{p}'^{3\mathsf{T}} - \mathbf{p}'^{2\mathsf{T}} \end{bmatrix}, \tag{83}$$

which provides a first estimate of the homogeneous vector $\mathbf{X} \in \mathbb{R}^4$, and describes a **tie point on the cometary surface** that is visible in two images.

Nonlinear Triangulation

After the first estimate of the point $\mathbf{X}$ obtained through linear triangulation in (83), a nonlinear algorithm can refine the triangulation result. The noisy measurement $\{\mathbf{x}, \mathbf{x}'\}$ does not necessarily fulfill the epipolar constraint $\hat{\mathbf{x}}'^{\mathsf{T}}\mathrm{E}\hat{\mathbf{x}} = 0$.

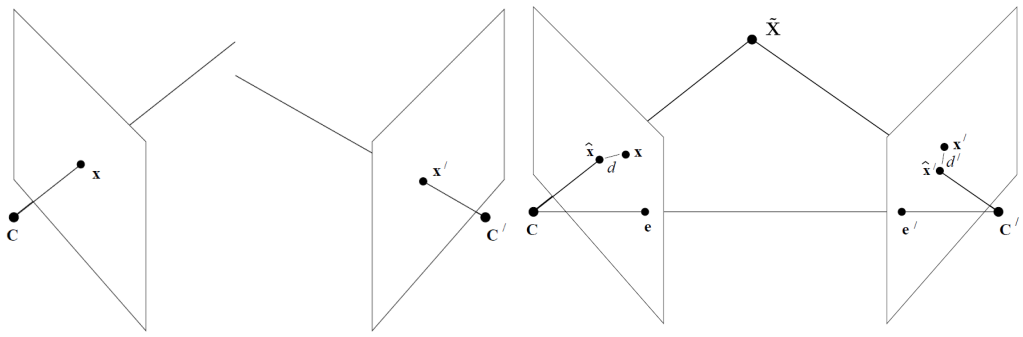

Figure 21: Presence of noise in the measurements $\mathbf{x}$ and $\mathbf{x}'$ of the point $\tilde{\mathbf{X}} \in \mathbb{R}^3$ in two different views $\mathbf{C}$ and $\mathbf{C}'$. This noise results in differences between measurement and reprojection - the **reprojection error** $d(\mathbf{x}, \hat{\mathbf{x}}), d'(\mathbf{x}', \hat{\mathbf{x}}')$. It can be seen that reprojected rays from imperfect measurements do not intersect [52].

Instead, the correct reprojected position of the image points is $\{\hat{\mathbf{x}}, \hat{\mathbf{x}}'\}$, lying close to the measured points $\{\mathbf{x}, \mathbf{x}'\}$ and satisfying the constraint $\hat{\mathbf{x}}'^{\mathsf{T}}\mathrm{E}\hat{\mathbf{x}} = 0$ exactly (Figure 21). Thus, the cost function [52]

$$C(\mathbf{x}, \mathbf{x}') = d(\mathbf{x}, \hat{\mathbf{x}})^2 + d'(\mathbf{x}', \hat{\mathbf{x}}')^2 \tag{84}$$

can be minimized with respect to the epipolar condition $\hat{\mathbf{x}}'^{\mathsf{T}}\mathrm{E}\hat{\mathbf{x}} = 0$, providing the maximum likelihood estimate (MLE) for $\mathbf{X}$ up to numerical accuracy. In [52], an optimal solution to the triangulation problem is provided, using a polynomial of degree six and solving non-iteratively for the MLE solution precisely. However, within this work, all optical reconstruction is refined through the process of bundle adjustment in the end. This technique will be thoroughly explained in subsection 3.2. With bundle adjustment, the camera parameters will subsequently be adjusted as well; they will be updated together with the coordinates of the formerly triangulated surface points. Therefore, in order to provide initial values, the above discussed methods are sufficient at this point. Advanced techniques of triangulation and further information may be found in [51].

2.6. Instrument Reference Frames, Calibration, and Boresight

In the following subsection, definitions are given that are needed to describe the function and orientation of the scientific instruments used within this work.

2.6.1. Rosetta NAVCAM Instrument and Image Frame

The Rosetta Navigation Camera has two identical cameras - a nominal and a redundant one. The optical heads protrude from the main body of the spacecraft, containing the optical system, the CCD detector, and the electronics required to operate the CCD [30]. The field of view of each camera is 5 degrees. The CCD detectors have 1024x1024 pixels with a broad spectral sensitivity in the visible range.

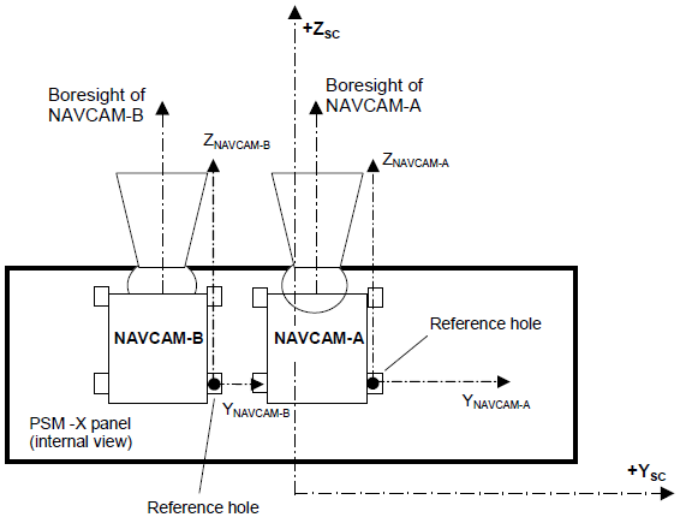

Figure 22: Definition of the Rosetta Navcam-A instrument reference frame [27]

In this work, only images recorded by the nominal unit Navcam-A are processed, since during the comet phase of the mission, this camera was used almost exclusively [42]. The corresponding instrument frame (Figure 22) is defined by the +Z axis pointing along the camera boresight. It is nominally co-aligned with the spacecraft's (s/c) +Z axis and oriented in view direction. The +X axis is parallel to the apparent image columns and nominally co-aligned with the s/c +X axis. The +Y axis completes a right-hand frame; it is nominally parallel to the apparent image lines and co-aligned with the s/c +Y axis. The origin of the frame is located at the camera focal point [41]. The coordinates of the Navcam-A unit with respect to the center of the Rosetta mechanical spacecraft frame are $[\ -0.973,\ 0.174,\ 1.971\ ]$ meters [27].

The image appears as stored in the CCD pixels on the detector. The columns are parallel to the X-axis and thus oriented vertically in the images. Their count starts with zero in the lower left image corner, where the line and column number counts increase with increasing coordinate value (Figure 23). The optical path leads to an inversion of the image coordinates with respect to the optical axis. As a result, to obtain the correct orientation of the scene in space, the image must be rotated by 180 degrees around the boresight [40].

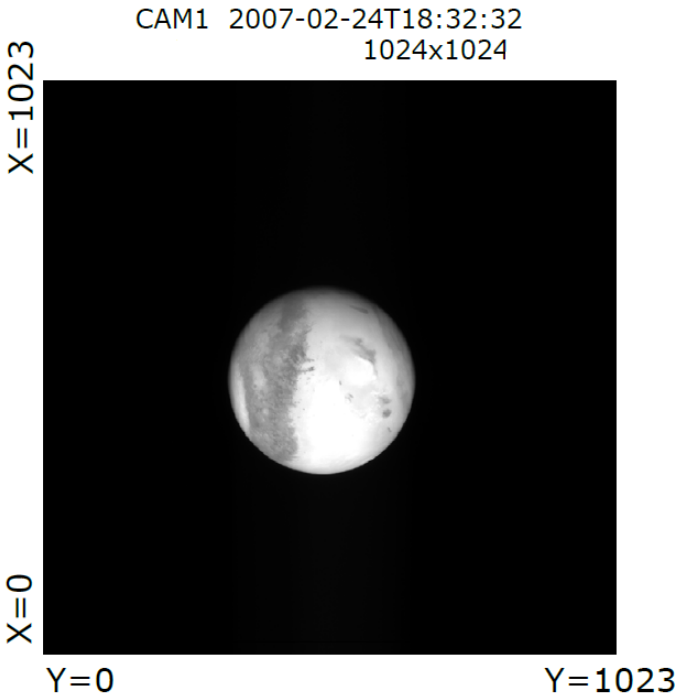

Figure 23: NAVCAM Image Orientation - CCD-Coordinates Example: Mars Swing-By 24 February 2007 [39].

2.6.2. OSIRIS Narrow Angle Camera Instrument and Image Frame

The OSIRIS camera system combines a narrow angle camera (OSIRIS-NAC) and a wide angle camera (OSIRIS-WAC). However, within this work, no images of the wide angle camera were processed. Therefore, only the reference frame of the OSIRIS narrow angle camera is explained.

The OSIRIS-NAC covers a field of view of 2.18 degrees with a CCD of 2048x2048 pixels and thus has a much better resolution than the NAVCAM. The corresponding instrument frame is defined in accordance with the NAVCAM frame. The +Z axis points along the camera boresight, the +X axis is parallel to the apparent image columns and the +Y axis completes the right-hand frame. All axes are nominally co-aligned with the

spacecraft-axes, and their origin is located at the camera focal point. For the OSIRIS-NAC, there are two different reference frames, the **mirror frame**, and the **nominal unit reference frame** [27]. The latter has a significant rotation and its origin is located at the OSIRIS-NAC reference hole, which is different to the focal point (Figure 24). In this work, only the OSIRIS-NAC mirror frame with the origin in the focal point is used for geometric processing. The focal point of the OSINAC is [−1.233, −0.157, 1.390] meters with respect to the Rosetta mechanical spacecraft frame [27]. The OSIRIS-NAC image frame is defined in accordance with the NAVCAM image frame; it can be seen in Figure 25. Detailed information about the OSIRIS system may be found in [57][108][64][58][18][90][17].

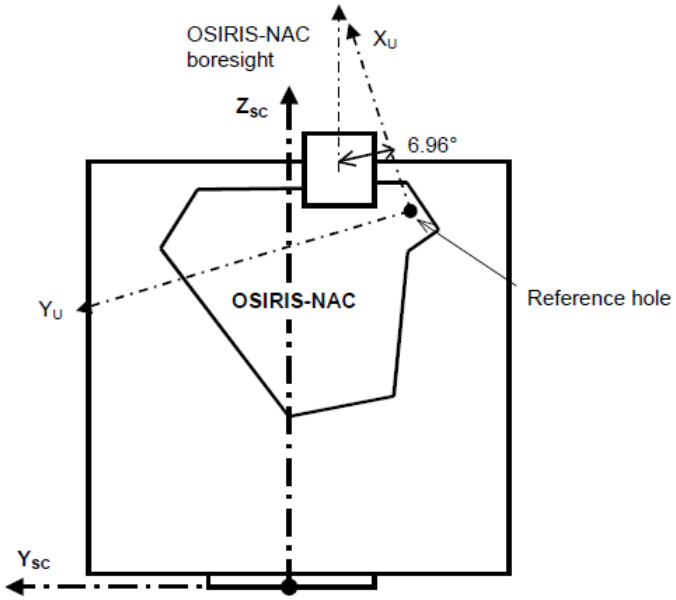

Figure 24: OSIRIS-NAC mirror frame and OSIRIS-NAC nominal unit reference frame [27].

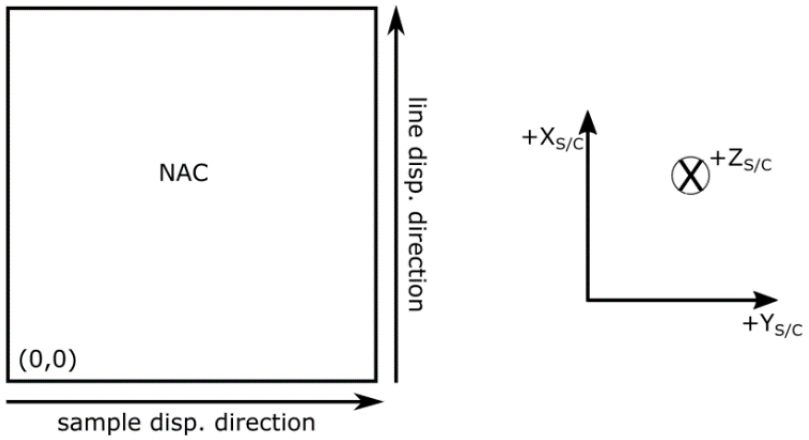

Figure 25: OSIRIS-NAC image reference frame definitions [18].

2.6.3. Instrument Boresight Alignment

The actual alignment of the camera boresights with respect to the mechanical spacecraft frame shows small deviations from nominal alignment and was determined by in-flight calibration. The actual NAVCAM-A boresight direction is specified in [33] as an offset from the s/c +Z axis along X s/c by -0.02678 and along Y s/c by $= -0.17210$ degrees. The difference may also be expressed as a corresponding pixel value, inducing an offset of ≈ 35 pixels from the image center. Consequently, when aiming for subpixel accuracy in optical reconstruction, the correct reference frame must be chosen carefully. The nominal alignment matrix of NAVCAM-A can be found in [32].

For the OSIRIS Narrow Angle Camera Frame, the offset in boresight alignment is smaller, but still not negligible. It has an offset from the s/c +Z axis along X s/c by -0.027 and along Y s/c by $= 0.013$ degrees, which means about 27 pixel units. In Figure 26, the instrument boresights of OSIRIS-NAC and NAVCAM-A as well as boresights of other Rosetta instruments are shown.

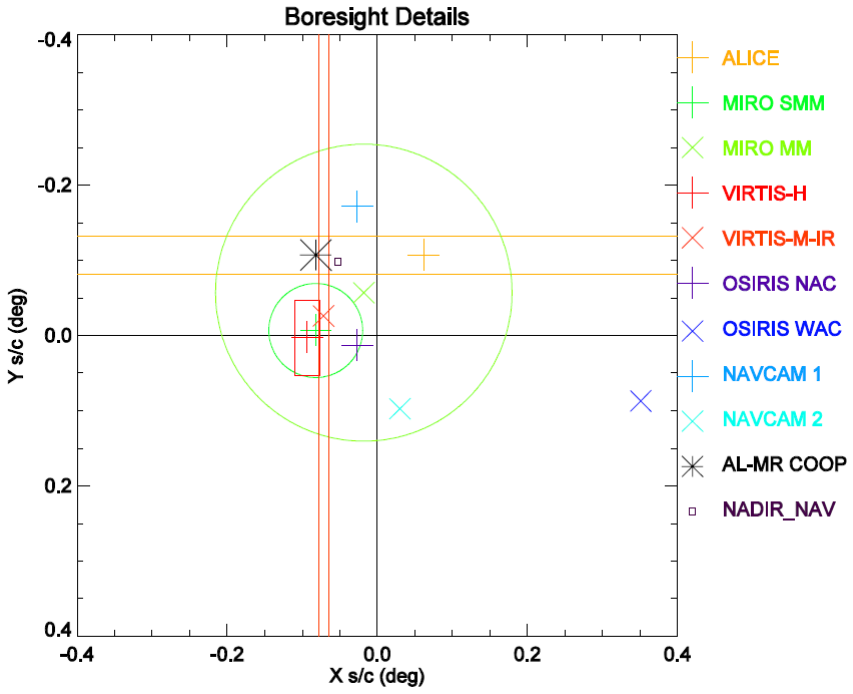

Figure 26: Detail of instrument boresights. +Z s/c points into the page [33].

2.6.4. Geometric Directional Calibration and Accuracy

Another important problem to be considered when transforming 3D-world points described in the **Cheops reference frame** introduced in subsection 2.1.1 into an image

plane coordinate frame is the nonlinear directional distortion caused by the respective camera system. For example, the distortion at the edge of the NAVCAM field-of-view is in the order of 1%, which means about 10 pixel units [40]. For a given pixel position (i, j) on the camera CCD, the corresponding direction in the NAVCAM-A camera frame is determined by [32]:

1) Converting the pixel position into a linear position relative to image center:

$$\begin{aligned} p_x &= 0.013\,(i - 511)\,, \\ p_y &= 0.013\,(j - 511)\,, \end{aligned} \tag{85}$$

2) Applying radial distortion correction to the relative linear position:

$$\begin{aligned} p_{x_{\text{Corr}}} &= p_x \left(1 + c_x \left(p_x^2 + p_y^2\right)\right), \\ p_{y_{\text{Corr}}} &= p_y \left(1 + c_y \left(p_x^2 + p_y^2\right)\right), \end{aligned} \tag{86}$$

3) Computing vector (d_x, d_y, d_z) and normalizing, where

$$\begin{aligned} d_x &= -\frac{p_{x_{\text{Corr}}}}{f_x}, \\ d_y &= -\frac{p_{y_{\text{Corr}}}}{f_y}, \\ d_z &= 1, \end{aligned} \tag{87}$$

with the radial distortion correction parameters

$$\begin{aligned} c_x &= -0.00012044038, \\ c_y &= -0.000114420733, \end{aligned} \tag{88}$$

and the focal length

$$\begin{aligned} f_x &= 152.5159, \\ f_y &= 152.4949. \end{aligned} \tag{89}$$

This algorithm is known to have a remaining geometric error up to about one pixel over the full CCD [32].

For the OSIRIS-NAC, a geometric calibration curve is also available. The camera

distortion is corrected over the full field of view. The correction values are fitted to a two dimensional, third-order polynomial. The undistorted pixel positions (X_u, Y_u) are expressed as a function of the actual image coordinates by [37]

$$X_u = \sum_{i,j} k_{x_{i,j}} X_0^i Y_0^j,$$
$$Y_u = \sum_{i,j} k_{y_{i,j}} X_0^i Y_0^j. \tag{90}$$

The full table of third-order polynomial fit coefficients for distortion removal $\left(k_{x_{i,j}}, k_{y_{i,j}}\right)$ may be found in [37] or in appendix A.6. After the removal of the radial distortion, an error up to 0.35 pixels remains for the OSIRIS-NAC. For the OSIRIS-WAC, an error up to 0.5 pixels remains in the image data. For the precise orbit determination purpose in this work, only OSIRIS-NAC images were processed. The remaining nonlinear distortion error distribution of OSIRIS-NAC and OSIRIS-WAC may be seen in Figure 27.

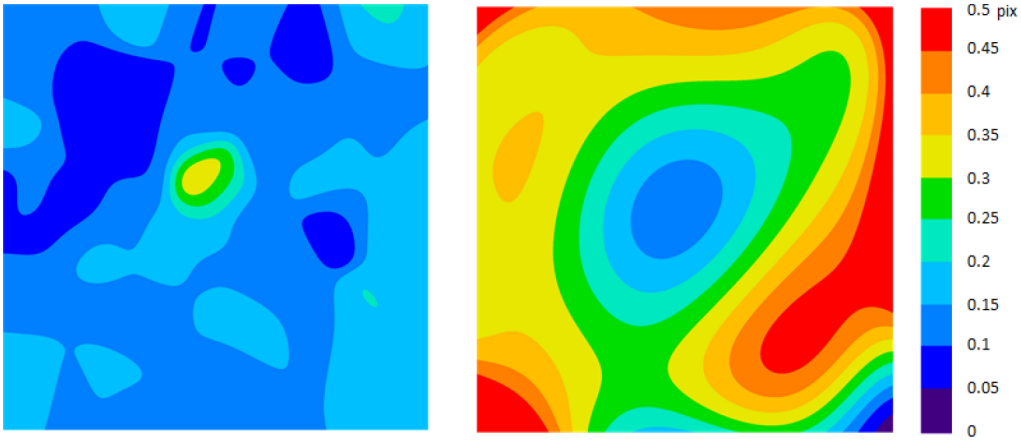

Figure 27: NAC distortion correction error (0, 0 pix bottom left) / WAC distortion correction error (0, 0 pix bottom right) [37][68].

2.7. Statistical Theory

In all scientific measurements in this work, the data has to be considered affected by some random error such as noise and so called outliers, i.e, incorrect measurements that result in large deviations from expected values. On top of this, the measurements may contain systematic errors, such as the remaining geometric calibration error of a camera.

One common approach to overcome random errors is to assume that the noise in these kinds of measurements is to be determined by some known statistical distribution. The

problem is then to find a solution which is best from a statistical point of view. Therefore, the **maximum likelihood estimation** has the goal of finding a mathematical model from which observations in a dataset of known statistical characteristics would be most likely. Generally, the method can be used for any estimation problem where one can presume a joint probability density function for the observations [6].

To further specify the problem, the most likely model parametrized by n elements in vector $\mathbf{m}$ for a set of m observations in vector $\mathbf{d}$ must be found. Once the model $\mathbf{m}$ is defined from a physical or geometrical point of view, for each observation d_i a probability density function $f(d_i, \mathbf{m})$ may be assumed. This PDF generally will vary, depending on $\mathbf{m}$. The joint probability density for a vector of observations $\mathbf{d}$ is then written as

$$f(\mathbf{d}, \mathbf{m}) = f_1(d_1, \mathbf{m}) \cdot f_2(d_2, \mathbf{m}) \cdot \ldots \cdot f_m(d_m, \mathbf{m}) = \prod_{i=1}^{m} f_i(d_i, \mathbf{m}), \tag{91}$$

where the values of $f(\mathbf{d}, \mathbf{m})$ are probability densities. Since the probability of an exact particular dataset is zero, a small box around that dataset must be considered. Then, the probability of this data is approximately proportional to the probability density $f(\mathbf{d}, \mathbf{m})$ itself. In this way, the **likelihood function** may be defined accordingly as

$$L(\mathbf{d}, \mathbf{m}) \approx f(\mathbf{d}, \mathbf{m}) = \prod_{i=1}^{m} f_i(d_i, \mathbf{m}), \tag{92}$$

where $\mathbf{d}$ is fixed and $\mathbf{m}$ is a set of variable parameters that can be adjusted in a way that the model is relatively likely to result in the data $\mathbf{d}$. The **maximum likelihood** principle is then to select the model $\mathbf{m}$ that maximizes the likelihood function $L(\mathbf{m}, \mathbf{d})$. If the assumption can be made that errors in the data are independent and normally distributed with expected value zero, the probability density for the i-th observation may be written as

$$f(d_i, \mathbf{m}) = \frac{1}{\sqrt{2\pi}\sigma_i} e^{-\left(\frac{(d_i - (\mathrm{G}\mathbf{m})_i)^2}{2\sigma_i^2}\right)}, \tag{93}$$

with the standard deviation σ_i of the i-th observation d_i and the matrix G from the

discrete inverse problem

$$\mathrm{G}\mathbf{m} = \mathbf{d}, \tag{94}$$

with residuals $\mathbf{r} = \mathbf{d} - \mathrm{G}\mathbf{m}$. The likelihood function may now be written as

$$L\left(\mathbf{d}, \mathbf{m}\right) = \frac{1}{\left(2\pi\right)^{\frac{m}{2}} \prod_{i=1}^{m} \sigma_i} \prod_{i=1}^{m} e^{-\left(\frac{\left(d_i - (\mathrm{G}\mathbf{m})_i\right)^2}{2\sigma_i^2}\right)}. \tag{95}$$

Maximizing the likelihood depending on the set of parameters $\mathbf{m}$ equals minimizing the associated negative log likelihood, since the logarithm is a monotonically increasing function. Eliminating the constant yields

$$\min \quad -\log \prod_{i=1}^{m} e^{-\left(\frac{\left(d_i - (\mathrm{G}\mathbf{m})_i\right)^2}{2\sigma_i^2}\right)} = \sum_{i=1}^{m} \frac{\left(d_i - (\mathrm{G}\mathbf{m})_i\right)^2}{2\sigma_i^2}. \tag{96}$$

While searching for a minimum, the constant 2 can be eliminated as well and with

$$\mathrm{W} = \mathrm{diag}\left(\frac{1}{\sigma_1}, \frac{1}{\sigma_2}, \ldots, \frac{1}{\sigma_m}\right), \ \mathrm{G}_w = \mathrm{W}\mathrm{G}, \ \mathbf{d}_w = \mathrm{W}\mathbf{d}, \tag{97}$$

one finds the now weighted system of equations which may be written as

$$\mathrm{G}_w\mathbf{m} = \mathbf{d}_w. \tag{98}$$

It has the least squares solution

$$\mathbf{m}_w = \left(\mathrm{G}_w^{\mathsf{T}}\mathrm{G}_w\right)^{-1} \mathrm{G}_w^{\mathsf{T}}\mathbf{d}_w. \tag{99}$$

Now,

$$\|\mathbf{d}_w - \mathrm{G}_w\mathbf{m}_w\|_2^2 = \sum_{i=1}^{m} \frac{\left(d_i - (\mathrm{G}\mathbf{m}_w)_i\right)^2}{\sigma_i^2}, \tag{100}$$

and the least squares solution to $\mathrm{G}_w\mathbf{m} = \mathbf{d}_w$ provides the **maximum likelihood estimate** for the model $\mathbf{m}$. For the computation of the associated covariance, one may make use of

$$\mathrm{Cov}\left(\mathbf{m}\right) = \left(\mathrm{G}_w^{\mathsf{T}}\mathrm{G}_w\right)^{-1}, \tag{101}$$

if noise in the data is independent and normally distributed with the expected value of zero. In the case of the data not being multivariate, one may further simplify to

$$\mathrm{Cov}\left(\mathbf{m}\right) = \sigma^2\left(\mathrm{G}^{\mathsf{T}}\mathrm{G}\right)^{-1}. \tag{102}$$

In nonlinear regression, matrix G is replaced by the Jacobian matrix J of a nonlinear function $G\left(\mathbf{m}\right)$. The discrete inverse problem from (94) is then the linearized relationship between the iteration step of the model parameters $\Delta\mathbf{m}$ and the respective change in the objective function $\Delta\mathbf{F}\left(\mathbf{m}\right)$, as described in (124). In this case, the covariance matrix changes with each step. However, this requires some approximations, which will be explained in the following.

2.7.1. Additional Aspects arising from Nonlinear Regression

Solving nonlinear inverse problems with the concept of least squares is probably one of the most commonly used methods in a broad variety of applications in technical or nature science. However, some simplifications, approximations, and assumptions are included in this approach. Therefore, it is even more important to get a thorough understanding of what these assumptions are and how they might affect the solution. For any arbitrary set of data, a somewhat nonlinear model may be found that fits these measurements and creates small residuals. However, a good model needs to fulfill some additional criteria. Therefore, in the following, some important notes on nonlinear optimization used in this work will be discussed. Assuming, that the nonlinear scalar valued function

$$f(\mathbf{m}) = \sum_{i=1}^{m} \left(\frac{G(\mathbf{m}, x_i) - d_i}{\sigma_i} \right)^2 \tag{103}$$

is twice continuously differentiable, the Taylor series approximation may be formulated as

$$f\left(\mathbf{m}^0 + \mathbf{s}\right) \approx f\left(\mathbf{m}^0\right) + \nabla f\left(\mathbf{m}^0\right)^{\mathsf{T}} \mathbf{s} + \frac{1}{2}\mathbf{s}^{\mathsf{T}} \nabla^2 f\left(\mathbf{m}^0\right) \mathbf{s}. \tag{104}$$

By neglecting the second order term, one may approximate the gradient of f by

$$\nabla f\left(\mathbf{m}^0 + \mathbf{s}\right) \approx \nabla f\left(\mathbf{m}^0\right) + \nabla^2 f\left(\mathbf{m}^0\right) \mathbf{s} \tag{105}$$

and equal this term to zero, since at minimum $\mathbf{m}^*$ the condition $\nabla f(\mathbf{m}^*) = \mathbf{0}$ must be fulfilled. This leads to

$$\nabla^2 f\left(\mathbf{m}^0\right) \mathbf{s} = -\nabla f\left(\mathbf{m}^0\right). \tag{106}$$

Solving this system of equations for step $\mathbf{s}$ leads to **Newton's method for minimizing** $f(\mathbf{m})$ [6]. Now, with the definitions

$$\mathbf{F}(\mathbf{m}) = \begin{bmatrix} f_1(\mathbf{m}) \\ f_2(\mathbf{m}) \\ \vdots \\ f_m(\mathbf{m}) \end{bmatrix}, \tag{107}$$

$$f_i(\mathbf{m}) = \frac{G(\mathbf{m}, x_i) - d_i}{\sigma_i}, \tag{108}$$

the gradient vector elements of $f(\mathbf{m})$ may be written as

$$\nabla f\left(\mathbf{m}\right)_j = \sum_{i=1}^{m} 2\nabla f_i\left(\mathbf{m}\right)_j \mathbf{F}\left(\mathbf{m}\right)_j, \tag{109}$$

or simplified in matrix notation by

$$\nabla f\left(\mathbf{m}\right) = 2\mathrm{J}\left(\mathbf{m}\right)^{\mathsf{T}} \mathbf{F}\left(\mathbf{m}\right), \tag{110}$$

with the Jacobian matrix

$$\mathrm{J}\left(\mathbf{m}\right) = \begin{bmatrix} \frac{\partial f_1(\mathbf{m})}{\partial m_1} & \dots & \frac{\partial f_1(\mathbf{m})}{\partial m_n} \\ \vdots & \ddots & \vdots \\ \frac{\partial f_m(\mathbf{m})}{\partial m_1} & \dots & \frac{\partial f_m(\mathbf{m})}{\partial m_n} \end{bmatrix}. \tag{111}$$

The left side of (106) at parameter vector $\mathbf{m}$ and without the step $\mathbf{s}$ may be expressed as

$$\nabla^2 f\left(\mathbf{m}\right) = \sum_{i=1}^{m} \nabla^2 \left(f_i\left(\mathbf{m}\right)^2\right) = \sum_{i=1}^{m} \mathrm{H}^i\left(\mathbf{m}\right), \tag{112}$$

where $\mathrm{H}^i\left(\mathbf{m}\right)$ is the Hessian Matrix of $f_i\left(\mathbf{m}\right)^2$. It is defined as

$$\mathrm{H}^i_{j,k}\left(\mathbf{m}\right) = \frac{\partial^2 \left(f_i\left(\mathbf{m}\right)^2\right)}{\partial m_j \partial m_k} \tag{113}$$

$$= \frac{\partial}{\partial m_j}\left(2 f_i\left(\mathbf{m}\right) \frac{\partial f_i\left(\mathbf{m}\right)}{\partial m_k}\right) \tag{114}$$

$$= 2\left(\frac{\partial f_i\left(\mathbf{m}\right)}{\partial m_j}\frac{\partial f_i\left(\mathbf{m}\right)}{\partial m_k} + f_i\left(\mathbf{m}\right)\frac{\partial^2 f_i\left(\mathbf{m}\right)}{\partial m_j \partial m_k}\right), \tag{115}$$

and thus, one may summarize

$$\nabla^2 f(\mathbf{m}) = 2\mathrm{J}(\mathbf{m})^{\mathsf{T}} \mathrm{J}(\mathbf{m}) + \mathrm{Q}(\mathbf{m}), \tag{116}$$

where

$$\mathrm{Q}(\mathbf{m}) = 2\sum_{i=1}^{m} f_i(\mathbf{m}) \nabla^2 f_i(\mathbf{m}). \tag{117}$$

In the **Gauss-Newton** method, the term $\mathrm{Q}(\mathbf{m})$ is assumed to be small and the Hessian Matrix is approximated by

$$\nabla^2 f(\mathbf{m}) \approx 2\mathrm{J}(\mathbf{m})^{\mathsf{T}} \mathrm{J}(\mathbf{m}). \tag{118}$$

With this approximation and the iteration step $\mathbf{s} = \left(\mathbf{m}^{k+1} - \mathbf{m}^{k}\right) = \Delta_{\mathbf{m}}$, equation (106) may be rewritten as

$$\mathrm{J}\left(\mathbf{m}^{k}\right)^{\mathsf{T}} \mathrm{J}\left(\mathbf{m}^{k}\right)\left(\mathbf{m}^{k+1} - \mathbf{m}^{k}\right) = -\mathrm{J}\left(\mathbf{m}^{k}\right)^{\mathsf{T}} \mathbf{F}\left(\mathbf{m}^{k}\right). \tag{119}$$

In the method of **Levenberg-Marquardt**, an additional parameter λ is introduced to insure convergence. It completes the equation to

$$\left(\mathrm{J}\left(\mathbf{m}^{k}\right)^{\mathsf{T}} \mathrm{J}\left(\mathbf{m}^{k}\right) + \lambda \mathrm{I}\right)\Delta_{\mathbf{m}} = -\mathrm{J}\left(\mathbf{m}^{k}\right)^{\mathsf{T}} \mathbf{F}\left(\mathbf{m}^{k}\right). \tag{120}$$

Thus, for large values of λ, the relation

$$\mathrm{J}\left(\mathbf{m}^{k}\right)^{\mathsf{T}} \mathrm{J}\left(\mathbf{m}^{k}\right) + \lambda \mathrm{I} \approx \lambda \mathrm{I} \tag{121}$$

ensures small but certain convergence; whereas, for small values of λ, one obtains the **Gauss-Newton** method with fast but uncertain convergence. Accordingly, the step size of $\Delta_{\mathbf{m}}$ changes with the regularization parameter λ. In each iterative step, the decrease of the objective function $f(\mathbf{m})$ can be evaluated, and the parameter λ can be

adjusted. If a covariance matrix $\Sigma_{\mathbf{d}}$ of the observations $\mathbf{d}$ is available, the weights σ_i from equation (108) can be found squared as the variances on the main diagonal of $\Sigma_{\mathbf{d}}$, and (120) can be written shortened as

$$\left(\mathrm{J}^{\mathsf{T}}\Sigma_{\mathbf{d}}^{-1}\mathrm{J} + \lambda\mathrm{I}\right)\Delta_{\mathbf{m}} = -\mathrm{J}^{\mathsf{T}}\Sigma_{\mathbf{d}}^{-1}\epsilon, \tag{122}$$

where the residuals $\epsilon_i = G(\mathbf{m}, x_i) - d_i$ are the differences between the observations d_i and the model $G(\mathbf{m}, x_i)$. The associated variances σ_i^2 of the observations can be found on the main diagonal of $\Sigma_{\mathbf{d}}$. In the case of nonlinear regression, there is no longer a linear relationship between the data and the parameters $\mathbf{m}$ from the estimation model. Accordingly, the assumption of multivariate, normally distributed model parameters is now an approximation through local linearization of the nonlinear function $\mathbf{F}(\mathbf{m})$ with [6]

$$\mathbf{F}(\mathbf{m}^* + \Delta_{\mathbf{m}}) \approx \mathbf{F}(\mathbf{m}^*) + \mathrm{J}(\mathbf{m}^*)\Delta_{\mathbf{m}}, \tag{123}$$

where small perturbations in the data are assumed to result in small perturbations in the model $\mathbf{m}$. With this approximation, the linearized relationship for changes in $\mathbf{F}(\mathbf{m})$ and $\mathbf{m}$ becomes

$$\Delta_{\mathbf{F}} \approx \mathrm{J}(\mathbf{m}^*)\Delta_{\mathbf{m}}, \tag{124}$$

and the covariance matrix may be obtained from

$$\mathrm{Cov}(\mathbf{m}^*) \approx \left(\mathrm{J}(\mathbf{m}^*)^{\mathsf{T}}\mathrm{J}(\mathbf{m}^*)\right)^{-1}, \tag{125}$$

which is in accordance with (101), however based on simplifications that were necessary because the problem is nonlinear. Hence, it is important to understand that the covariance matrix together with the uncertainties of the estimated parameters result from two critical approximations. First, the term $\mathrm{Q}(\mathbf{m})$ was assumed to be small and was dropped. Second, the model $f(\mathbf{m})$ was linearized around $\mathbf{m}^*$. Depending on the

problem, these two approximations can be problematic and cause incorrect interpretations of parameter uncertainties and the parameters themselves.

As soon as combinations of model parameters are considered, additionally, parameter correlation can affect the solution. The confidence intervals for the parameters may then be significantly larger than the intervals for the ones that are considered individually. The confidence region is an n-dimensional error ellipsoid, defined by the inequality

$$(\mathbf{m}_{\text{true}} - \mathbf{m}^*)\,\text{Cov}\,(\mathbf{m}^*)^{-1}\,(\mathbf{m}_{\text{true}} - \mathbf{m}^*) \leq \Delta^2, \tag{126}$$

where Δ^2 can be a percentile of the χ^2 distribution with n degrees of freedom, chosen, for example, to be within 99%. The error ellipsoid's principal axis may then be found from the eigenvalue problem

$$\text{Cov}\,(\mathbf{m}^*)^{-1} = \mathrm{P}^{\mathsf{T}}\Lambda\mathrm{P}, \tag{127}$$

where Λ contains the eigenvalues $\{\lambda_1, \lambda_2, \ldots, \lambda_n,\}$ on its main diagonal, and P contains the eigenvectors, associated to the error ellipsoid's principal axes, respectively. The 99% confidence ellipsoid's semiaxis lengths κ_i in the principal axes directions may then be found via

$$\kappa_i = \sqrt{\frac{F^{-1}_{\chi^2,n}\,(0.99)}{\lambda_i}}\;, \quad i = (1, 2, \ldots n)\,. \tag{128}$$

This confidence ellipsoid may thereafter be projected back into the $\mathbf{m}^*$ coordinate system, which yields the parameter uncertainties in case of correlated parameters.

2.7.2. Tikhonov-Regularization

In the context of finding a model that describes the trajectory of the spacecraft around the comet, parameters are spread widely regarding their influence on the spacecraft orbit, reaching from stronger inputs like perturbation gravitational forces or solar pressure down to tiny changes caused by wheel offloadings. The inverse solution

$$\Delta = -\left(\mathrm{J}^{\mathsf{T}}\mathrm{J} + \lambda\mathrm{I}\right)^{-1}\mathrm{J}^{\mathsf{T}}\epsilon, \tag{129}$$

may become unstable if one or more of the singular values s_i in $\left(\mathrm{J}^{\mathsf{T}}\mathrm{J} + \lambda\mathrm{I}\right)$ is small. The least squares problem may, therefore, become ill-posed. The positive effect obtained from a Tikhonov-Regularization is that an ill-posed problem may be solved as less sensitive to noise-data by giving larger weight to larger singular values and lower weight to small singular values. After a singular value decomposition, the generalized solution of an inverse problem $\mathrm{J}\Delta = \epsilon$ may be expressed as [6]

$$\boldsymbol{\Delta} = \mathrm{J}^{-1}\epsilon = \mathrm{V}\mathrm{S}^{-1}\mathrm{U}^{\mathsf{T}}\epsilon = \sum_{i=1}^{n} \frac{\left(\mathrm{U}_{.,i}\right)^{\mathsf{T}}\epsilon}{s_i}, \mathrm{V}_{.,i.}. \tag{130}$$

With the SVD of J in (129) one finds that [6]

$$\left(\mathrm{V}\mathrm{S}^{\mathsf{T}}\mathrm{U}^{\mathsf{T}}\mathrm{U}\mathrm{S}\mathrm{V}^{\mathsf{T}} + \lambda\mathrm{I}\right)\Delta = \left(\mathrm{V}\mathrm{S}^{\mathsf{T}}\mathrm{S}\mathrm{V}^{\mathsf{T}} + \lambda\mathrm{I}\right)\Delta = \mathrm{V}\mathrm{S}^{\mathsf{T}}\mathrm{U}^{\mathsf{T}}\epsilon. \tag{131}$$

Hence, the solution of the non singular system of equations (131) deduces to [6]

$$\Delta_\lambda = \sum_{i=1}^{n} \frac{s_i^2}{s_i^2 + \lambda} \frac{\left(\mathrm{U}_{.,i}\right)^{\mathsf{T}}\epsilon}{s_i} \mathrm{V}_{.,i.} \tag{132}$$

where

$$f_i = \frac{s_i^2}{s_i^2 + \lambda} \tag{133}$$

is called filter factor and fulfills the relation that $f_i \approx 1$ if $s_i \gg \lambda$ and $f_i \approx 0$ if $s_i \ll \lambda$. In between, the effect reduces the relative contribution of the smaller singular values to the solution.

Estimation and statistical aspects are core considerations for this thesis. The correct interpretation is crucial for all results. Iterative parameter estimation and inverse

problems will be important topics for three main areas within this work: the accurate measurement of features within the camera CCD, the estimation of projective geometry, and the determination of cometary parameters. Especially, when the trajectory of a spacecraft is obtained from the estimated gravitational field, parameter correlations become important and affect the solution. This problem will be thoroughly discussed in section 4. The content of this subsection was mainly taken from [6], a more detailed description of statistical aspects may be found within this reference.

This concludes chapter 2 – the theoretical fundamentals within this work. The next chapters will give an overview of what was implemented, and the results that could be derived.

3. Numerical Implementation

In this work, MATLAB and FORTRAN routines were developed with the goal of gravitational field estimation based on optical data. The following chapter gives an overview of which methods and algorithms were used, and how they were combined. All three main software components – the feature detection and matching algorithm, robust sparse bundle adjustment and the software for the estimation of cometary parameters – will be thoroughly described here.

3.1. Feature Detection and Matching Algorithm

As introduced in section 1, the goal of this part of the software is to automatically detect and match tie points that are maximally repeatable together with the highest possible accuracy of the measurement within the imagery data. According to [12], the quality of the matching results generally depends on:

1. the greyvalue distribution of image functions (texture, image gradients),
2. the selection of transformation functions for matching,
3. the patch size of the template (reference window),
4. the amount of geometric distortion between both images,
5. the quality of initial values, especially for shift parameters.

For the first point, a well-established method that can be used to find areas with favorable and distinctive greyvalue distributions is the scale invariant feature transform **(SIFT)**. It automatically detects features in the optical data and tracks them over a consecutive image series while being robust against changes in rotation and scale as well as moderate illumination changes. Since automated image processing is needed with thousands of images available, the detection part of the **SIFT** algorithm is used to find distinctive features that are visible in multiple images.

For the second point, regarding the transformation function for the matching part, a least squares technique is used and will be explained in subsection 3.1.2. The remaining criteria in the above listed items of matching quality will be discussed in subsections 3.1.2 - 3.1.5. Since **SIFT** initially finds the key points in the imagery data for the feature detection and matching algorithm (**FDAM**), it will be briefly explained in the following.

3.1.1. Scale Invariant Feature Transform (SIFT)

According to [80][84][79], the maxima and minima found using a scale-normalized Laplacian of Gaussian image function $\sigma^2\nabla^2 G$ produce **the most stable image features** for key point matching. **SIFT** uses a close approximation to that function, called the difference-of-Gaussian **(DoG)** scale space. Since the detection of maximum stable and repeatable image features is needed for **FDAM**, this is the initial method of choice for the algorithm.

The basic principle of the method is Gaussian filtering of camera images at multiple scales. First, an input image is repeatedly convolved with a variable-scale Gaussian kernel, $G(x, y, \sigma)$, defined as [80]

$$G(x, y, \sigma) = \frac{1}{2\pi\sigma^2} e^{\left(-\frac{x^2+y^2}{2\sigma^2}\right)}. \tag{134}$$

The repeated convolution of the initial image with the Gaussian kernel leads to an increased blurring after each convolution. The resulting images are then stored in the Gaussian scale space $L(x, y, \sigma)$ of the input image via

$$L(x, y, \sigma) = G(x, y, \sigma) * I(x, y), \tag{135}$$

where $*$ is the convolution operation and $I(x, y)$ is the input image in pixel coordinates x and y, for NAVCAM and OSINAC defined as in Figures 23 and 25, subsection 2.1.1. After this initial step, neighboring images in the Gaussian scale space are subtracted to create $D(x, y, \sigma)$, the Difference-of-Gaussian (DoG) scale space (Figure 28). It may be obtained from [80][79]

$$\begin{aligned} D(x, y, \sigma) &= (G(x, y, k\sigma) - G(x, y, \sigma)) * I(x, y) \\ &= L(x, y, k\sigma) - L(x, y, \sigma). \end{aligned} \tag{136}$$

It can be seen that the DoG scale space images are separated in scale by a constant factor k. After σ has become twice the initial value in the repeated convolution operation, the block of the Gaussian scale space is now considered a full octave. The last image is then down-sampled by a factor of 2, which leads to a significant reduction in computation time while no information in the measurement is lost, since the input image was increasingly blurred from the repeated convolution. As suggested in [80], σ is chosen to be 1.6 and the scale factor is determined from $k = 2^{\frac{1}{s}}$, where s denotes the number of blurred

images per octave. These values are obtained from empirical tests described in [80].

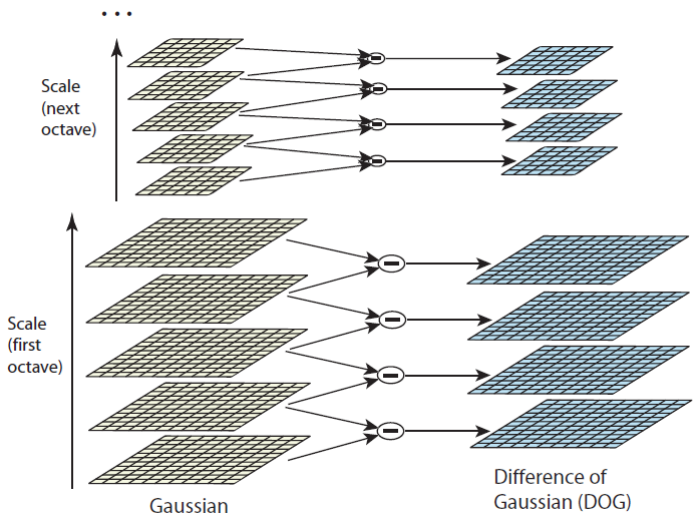

Figure 28: The creation of the Gaussian and difference-of-Gaussian (DoG) scale space from an input image [80].

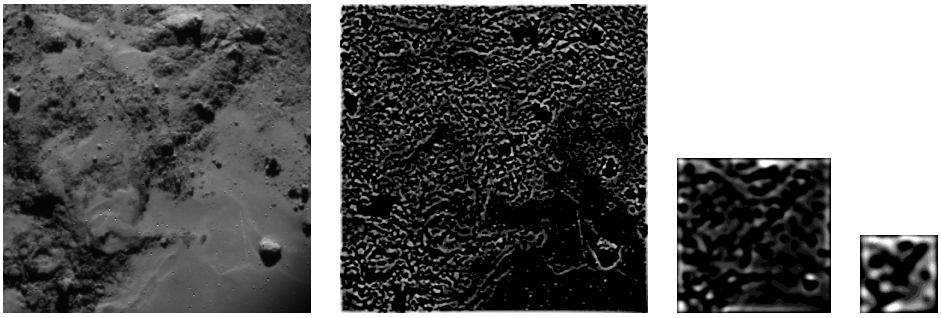

Figure 29: From left to right: An input image extract of the cometary surface taken by the Rosetta NAVCAM in 2014 followed by three corresponding images in the DoG scale space. In each octave, the respective first level is shown. The down-sampling between the first three octaves can be seen in the three images on the right side.

In Figure 29 it can be seen, that the increasingly blurred images create extrema on different scales; this approximates a camera taking images in the same area of the cometary surface from a continuously increasing distance. Thus, the method is capable of finding key point matches in images taken from different orbits. This makes it an excellent starting point for the **FDAM** algorithm; however, the advantage is not unlimited when differences in scale become too large. On top of this, note that the boulder-type feature in the bottom right of the image extract creates a lot of extrema around its shadow.

Since shadows are moving relative to the angle of sunlight incidence, this problem needs to be accounted for and will be covered later.

After the difference-of-Gaussian scale space was created, pixels are compared with their neighboring pixels, including the adjacent scale images. If a pixel turns out to have a minimum or maximum value compared to its 26 neighbors, it is initially detected as a distinctive feature (Figure 30).

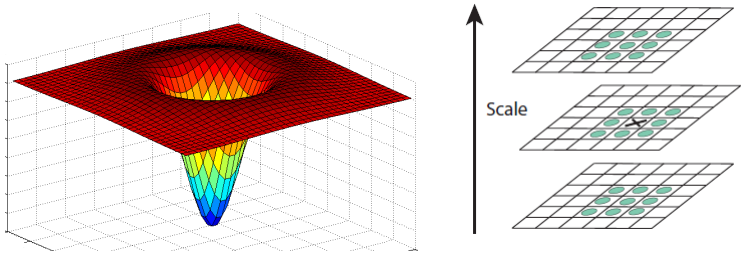

Figure 30: Left: A variable scale difference-of-Gaussian function. Right: Detection of distinctive features from extrema when compared to 26 neighboring values in the difference-of-Gaussian (DoG) scale space [80].

After the features were detected as previously described, some of them need to be rejected again. In order to generally avoid unstable responses to edges in images - such as sharp corners of shadows with large gradients in one direction and small perpendicular gradients - the ratio r of eigenvalues α, β

$$\alpha = r\beta, \tag{137}$$

obtained from the Hessian matrix

$$\mathrm{H} = \begin{bmatrix} D_{xx} & D_{xy} \\ D_{xy} & D_{yy} \end{bmatrix}, \tag{138}$$

can be used together with the trace and the determinant (appendix A.3) of H

$$\frac{\mathrm{tr}\,(\mathrm{H})^2}{\det(\mathrm{H})} < \frac{(r+1)^2}{r}, \tag{139}$$

in order to define a threshold for rejection of those key points. For the localization of the remaining features with sub-pixel accuracy, a Taylor expansion of the DoG scale-space function up to quadratic terms may be used. It has its origin at the sample point that was previously detected and may be written as [80]

$$D(\mathbf{x}) = D + \frac{\partial D^{\mathsf{T}}}{\partial \mathbf{x}}\mathbf{x} + \frac{1}{2}\mathbf{x}^{\mathsf{T}}\frac{\partial^2 D}{\partial \mathbf{x}^2}\mathbf{x}. \tag{140}$$

The derivative of this approximation with respect to $\mathbf{x} = (x, y, \sigma)$ can be set to zero and hence, the subpixel-accurate location of the extremum $\hat{\mathbf{x}}$ can be determined from [80]

$$\hat{\mathbf{x}} = -\left(\frac{\partial^2 D}{\partial \mathbf{x}^2}\right)^{-1}\frac{\partial D}{\partial \mathbf{x}}. \tag{141}$$

If the offset of the extremum is more than 0.5 pixel from the sample point location in any dimension, the interpolation is carried out from the closer sample point [80]. In a last step, additional unstable extrema with low contrast can be rejected through the definition of a threshold that discards key points with a small DoG scale space function value.

After the key point detection, localization, and rejection process, descriptor arrays are assigned to those points that remain in the selection (Figure 32). The descriptor is determined by the main gradient direction and magnitude around the key point. It is then used as a reference in comparison with other key points and enables the method to be invariant to image rotation. Hereafter, the local image gradients in a certain region around the key point are added to a descriptor array for each feature. A nearest neighbor search in the descriptor space finally allows for matching of the key points.

However, since the key point matching process in **FDAM** uses a different technique, this part of **SIFT** will not be explained at a greater level of detail within this work. More information about **SIFT** and its implementation can be found in [80][115][110][83][86].

In Figure 31, the subpixel accurate localization of key points in the DoG scale space extrema can be seen. The scale space is the result of the repeated convolution of the input image with the difference-of-Gaussian image function and thus depends on differences (gradients) in the initial image greyvalues.

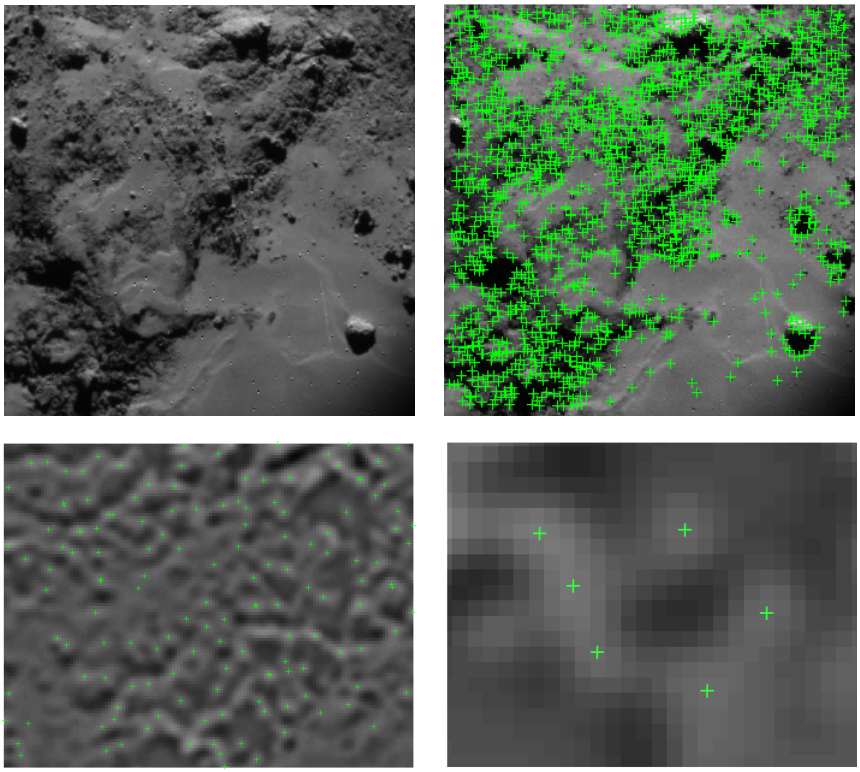

Figure 31: Top row, left side: NAVCAM input image extract. Right side: Detected key points within the data. It can be seen, that the method favors key points in regions where higher image gradients are present. As a consequence, rather flat areas on the surface lead to less detections. Bottom row: Subpixel-accurate location of key points within the DoG scale space by the SIFT key point detector.

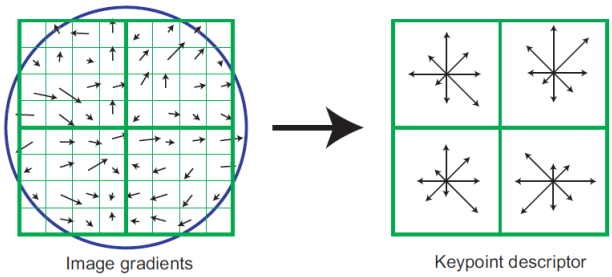

Figure 32: Design of the **SIFT descriptor** - after computation, the locally evaluated image gradients are summarized in histograms and compared in a nearest neighbor search for matching [80].

The greyvalues, in turn, are a measure of the number of photons that impacted the respective pixel on the camera CCD during exposure time; they depend on the illumination conditions and reflectance of the cometary surface. However, since illumination changes over consecutive images, the maximum in the DoG scale space generated from a distinctive feature on the cometary surface in one image can arise with an offset pixel value in a second image if, for example, the angle of incidence changes. Thus, **SIFT** is only used for initial detection. A more accurate matching algorithm that is robust with respect to illumination changes will be introduced later in subsection 3.1.6.

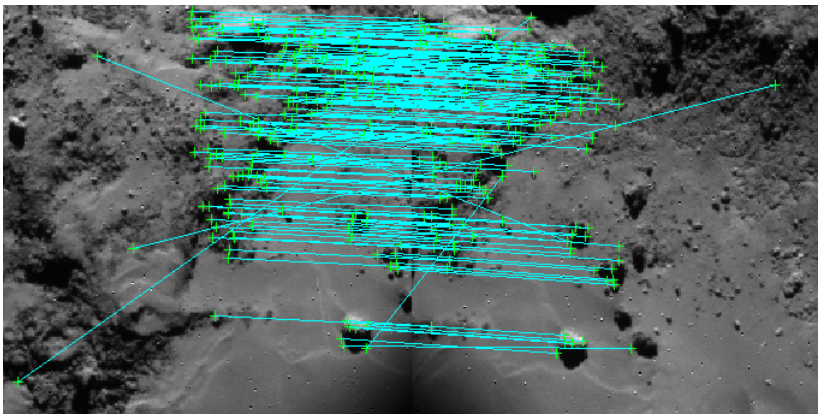

Figure 33: The input image familiar from Figures 29 and 31 (left side) after a full detection and matching cycle with a second image (right side) based on **SIFT** alone. It is clearly visible that outliers are still present which might affect the solution later.

After the initial key point detection and matching, outliers are still present in the correspondences (Figure 33). Generally, as previously introduced, the existence of outliers cannot be avoided in key point matching algorithms, regardless of the method of choice. However, a multitude of possible approaches and techniques for outlier removal is available in computer vision related literature. One common first approach to overcome the problem is to make use of relative geometric information, such as derived from epipolar geometry. The relationship known from equations (68), (72), and (73) - introduced in section 2 - can be used as a starting point. If orbit and attitude data is already available, the a priori geometric information may be used to get an initial estimate for E from (75) and then define a threshold ϵ in order to discard all matches that fulfill the inequality

$$\hat{\mathbf{x}}_2^{\mathsf{T}} \mathrm{E} \hat{\mathbf{x}}_1 > \epsilon. \tag{142}$$

In this way, wrong correspondences that do not fulfill the epipolar constraint (73) can be rejected. However, as described in Figure 19, outliers close to the epipolar lines still remain in the solution with this approach. Thus, additional constraints are needed and will be introduced in subsection 3.1.4. Figures 35 and 34 show the initial detection and matching results by **SIFT** together with a first outlier removal applied, as described, with (142). The method was tested both with images of **67P** as well as on the surface of **Jupiter's moon Europa** (Figure 34). The latter shows the method's capability of finding key point correspondences over different scales.

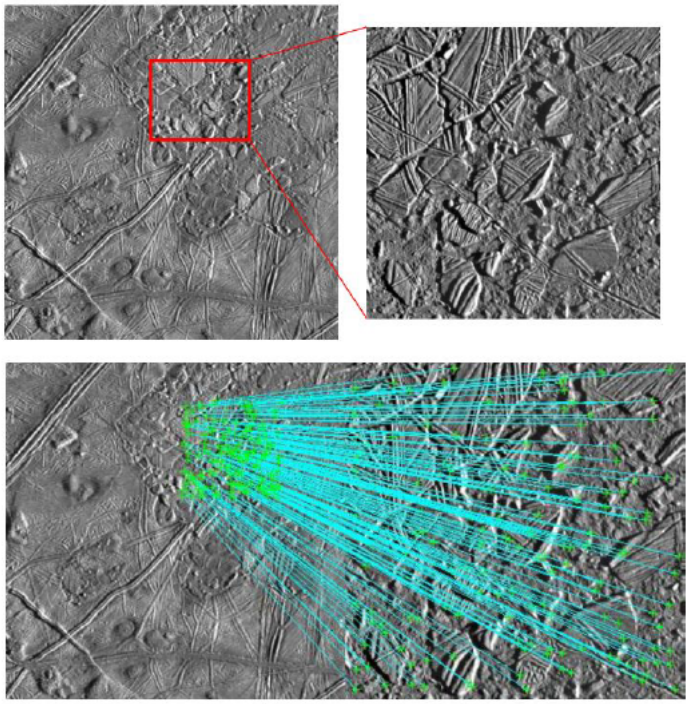

Figure 34: Application of **SIFT** to images where the same area of Europa is visible in different resolutions [67].

3.1.2. Least Squares Matching on a Polynomial Basis

In the last subsection, it was shown that **SIFT** is one of the best tools available to detect stable, repeatable, and distinctive features in imagery data. However, extrema detected in scale space via this method depend on the illumination angle. Furthermore, the gradients used for feature matching in the descriptor array also change with illumination. For this reason, if the angle of incidence changes by too many degrees in between images, **the SIFT algorithm starts to fail**. The conclusion is that, for the specific application within this work, **SIFT** is very useful for the detection of recognizable features on the cometary surface; however, it needs to be supported by an additional method in

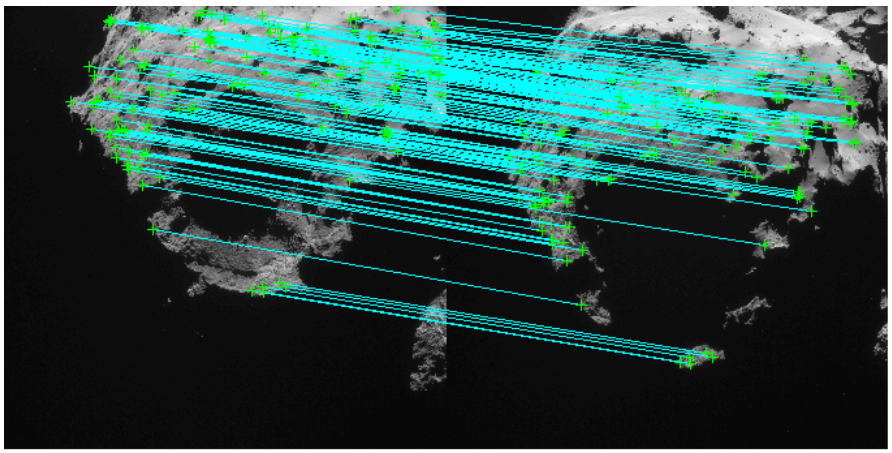

Figure 35: Initial key point matching on the cometary surface, enabling the first step in the **FDAM** algorithm introduced in this work.

the matching process. Here, a **least squares matching based on a polynomial geometric transformation function** is the method of choice, because it is convenient especially in the presence of a curved surface as it is observed at comet 67P (Figure 37).

Assume that after the initial **SIFT** detection and matching step a number of point correspondences - so called **tie points** - are available between two input images. Now, small image patches may be extracted around these tie points by a predefined number of pixels in both image coordinate directions. The two image patches can be described as two scalar-valued greyvalue functions $\{g', g''\}$ that depend on two coordinate functions each. They can be written as

$$g'(x', y') \;\; , \;\; g''(x'', y'') \, . \tag{143}$$

Note that the coordinates of the second patch can be written as a function of the coordinates in patch one [12],

$$x'' = f_x(x', y') \;\; , \;\; y'' = f_y(x', y') \, . \tag{144}$$

As introduced in subsection 2.7, the measurements of the pixel greyvalues must be considered to be affected by random noise. Hence, consider the normal distributed noise functions $e'(x', y'), e''(x'', y'')$ in both images. Now, the geometric model between both image functions may be written as

$$g'(x', y') + e'(x', y') = g''(f_x(x', y'), f_y(x', y')) + e''(x'', y''). \tag{145}$$

Here, the greyvalues of $g''(f_x(x', y'), f_y(x', y'))$ can be interpolated by using splines, since the geometric transformation function has non-integer numbers. Additionally, a two parameter linear contrast stretching yields

$$g'(x', y') + e'(x', y') = r_0 + r_1 \cdot g''(f_x(x', y'), f_y(x', y')) + e''(x'', y''). \tag{146}$$

The observation equation can now be defined as

$$l(x', y') + v(x', y') = r_0 + r_1 \cdot g''(f_x(x', y'), f_y(x', y')) - g'(x', y'), \tag{147}$$

where the noise functions $e'(x', y')$, $e''(x'', y'')$ have been substituted to

$$v(x', y') = e'(x', y') - e''(x'', y''). \tag{148}$$

As introduced in (144), the coordinate functions for both image patches may be defined depending on each other. To find the respective transformation functions, **least squares matching** is a widely used method in computer vision, whereby commonly affine transformations of the patch coordinates are used [99][45][46]. However, [12] has shown in several tests that affine and projective transformations can yield systematic errors for the measured tie point coordinates. For example, the projective approach is only geometrically correct as long as the object surface is a plane.

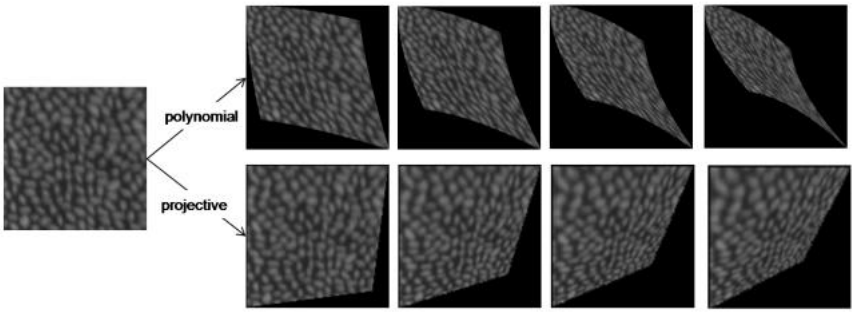

Figure 36: An example of geometric distortions of a synthetic input image patch. It illustrates, that surface patches with curvature can be modeled more accurately through polynomial geometric transformations [12].

Hence, if the surface visible in the image patches is subject to curvature, the geometric model covered through affine or projective transformation is insufficient (Figure 36). With [12], a novel approach, including an advanced least squares matching algorithm, was introduced. It uses **polynomial geometric transformations** and, in this way, allows for a highly accurate reconstruction of curved surfaces (Figure 37). Additionally, it allows for smaller parameter correlations within the estimation of the geometric transformation whereas **only four additional parameters need to be added** in comparison with the projective approach.

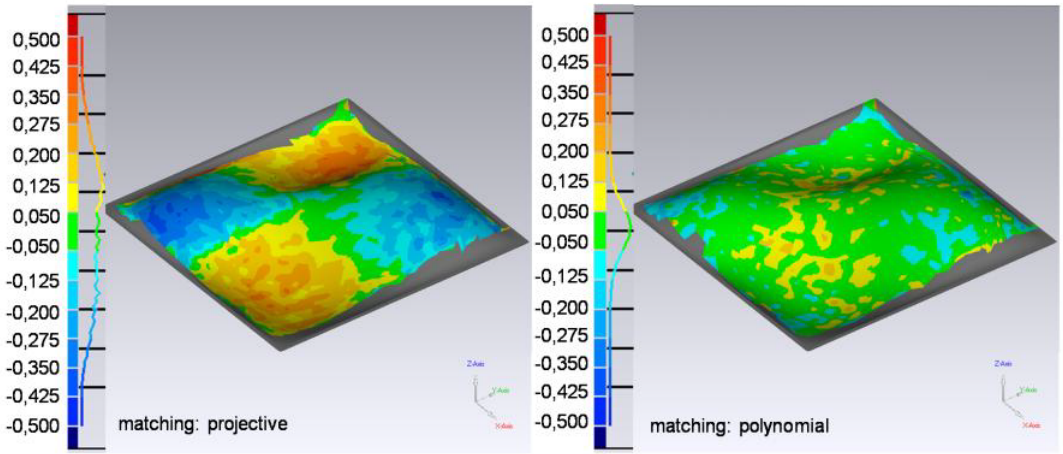

Figure 37: Relative error in three-dimensional reconstruction of a curved surface in comparison with calibrated data from the study accomplished in [12]. Note that in areas of more pronounced curvature, polynomial matching significantly improves the solution.

Since small solar system bodies such as **67P** are irregularly shaped, the strong curvature of the surface must be considered in key point matching. Hence, the geometric

transformation within the coordinates of the extracted image patches **is carried out on a polynomial basis within this work**, as suggested in [12]. The respective transformation functions may be written as

$$\begin{aligned} x'' &= f_x\left(x', y'\right) = \sum_{j=0}^{n} \sum_{i=0}^{j} a_{ij} x'^{(j-i)} y'^{(i)}, \\ y'' &= f_y\left(x', y'\right) = \sum_{j=0}^{n} \sum_{i=0}^{j} b_{ij} x'^{(j-i)} y'^{(i)}, \end{aligned} \tag{149}$$

where the parameter n defines the polynomial order and is set to $n = 2$, as suggested by the authors of [12]. This results in twelve parameters $(a_{00},\ a_{10},\ a_{11},\ a_{20},\ a_{21},\ a_{22})$ and $(b_{00},\ b_{10},\ b_{11},\ b_{20},\ b_{21},\ b_{22})$ to be estimated for the geometric transformation model as well as two additional parameters $(r_0,\ r_1)$ that must be determined for the radiometric transformation. Applied to the observation equation in (147), the linearized correction equation may be written as [12]

$$\begin{aligned} l\left(x', y'\right) + v\left(x', y'\right) = r_0^0 + r_1^0 \cdot g''^0 \left(f_x^0\left(x', y'\right), f_y^0\left(x', y'\right)\right) \\ + \left(\frac{\partial g''}{\partial a_{00}}\right) \mathrm{d}a_{00} + \left(\frac{\partial g''}{\partial a_{10}}\right) \mathrm{d}a_{10} + \left(\frac{\partial g''}{\partial a_{11}}\right) \mathrm{d}a_{11} \\ + \left(\frac{\partial g''}{\partial a_{20}}\right) \mathrm{d}a_{20} + \left(\frac{\partial g''}{\partial a_{21}}\right) \mathrm{d}a_{21} + \left(\frac{\partial g''}{\partial a_{22}}\right) \mathrm{d}a_{22} \\ + \left(\frac{\partial g''}{\partial b_{00}}\right) \mathrm{d}b_{00} + \left(\frac{\partial g''}{\partial b_{10}}\right) \mathrm{d}b_{10} + \left(\frac{\partial g''}{\partial b_{11}}\right) \mathrm{d}b_{11} \\ + \left(\frac{\partial g''}{\partial b_{20}}\right) \mathrm{d}b_{20} + \left(\frac{\partial g''}{\partial b_{21}}\right) \mathrm{d}b_{21} + \left(\frac{\partial g''}{\partial b_{22}}\right) \mathrm{d}b_{22} \\ + \left(\frac{\partial g''}{\partial r_0}\right) \mathrm{d}r_0 + \left(\frac{\partial g''}{\partial r_1}\right) \mathrm{d}r_1 - g'\left(x', y'\right). \end{aligned} \tag{150}$$

The partial derivatives contain the product of the outer and inner function of the second image patch $g''^0\left(x'', y''\right)$. The outer function derivatives correspond to the image gradients

$$g_x = \frac{\partial g''^0\left(x'', y''\right)}{\partial x''},\ g_y = \frac{\partial g''^0\left(x'', y''\right)}{\partial y''}, \tag{151}$$

whereas the inner function derivatives correspond to the geometric transformation model. Thus, the differential quotients of all fourteen unknowns may be written as [12]

$$
\begin{aligned}
&\left(\frac{\partial g''}{\partial a_{00}}\right) = r_1 \cdot \frac{\partial g''^0\,(x'', y'')}{\partial x''}, \qquad \left(\frac{\partial g''}{\partial a_{10}}\right) = r_1 \cdot \frac{\partial g''^0\,(x'', y'')}{\partial x''} \cdot x', \\
&\left(\frac{\partial g''}{\partial a_{11}}\right) = r_1 \cdot \frac{\partial g''^0\,(x'', y'')}{\partial x''} \cdot y', \qquad \left(\frac{\partial g''}{\partial a_{20}}\right) = r_1 \cdot \frac{\partial g''^0\,(x'', y'')}{\partial x''} \cdot x'^2, \\
&\left(\frac{\partial g''}{\partial a_{21}}\right) = r_1 \cdot \frac{\partial g''^0\,(x'', y'')}{\partial x''} \cdot x' \cdot y', \qquad \left(\frac{\partial g''}{\partial a_{22}}\right) = r_1 \cdot \frac{\partial g''^0\,(x'', y'')}{\partial x''} \cdot y'^2, \\
&\left(\frac{\partial g''}{\partial b_{00}}\right) = r_1 \cdot \frac{\partial g''^0\,(x'', y'')}{\partial y'}, \qquad \left(\frac{\partial g''}{\partial b_{10}}\right) = r_1 \cdot \frac{\partial g''^0\,(x'', y'')}{\partial y'} \cdot x', \\
&\left(\frac{\partial g''}{\partial b_{11}}\right) = r_1 \cdot \frac{\partial g''^0\,(x'', y'')}{\partial y'} \cdot y', \qquad \left(\frac{\partial g''}{\partial b_{20}}\right) = r_1 \cdot \frac{\partial g''^0\,(x'', y'')}{\partial y'} \cdot x'^2, \\
&\left(\frac{\partial g''}{\partial b_{21}}\right) = r_1 \cdot \frac{\partial g''^0\,(x'', y'')}{\partial y'} \cdot x' \cdot y', \qquad \left(\frac{\partial g''}{\partial b_{22}}\right) = r_1 \cdot \frac{\partial g''^0\,(x'', y'')}{\partial y'} \cdot y'^2, \\
&\left(\frac{\partial g''}{\partial r_0}\right) = 1, \qquad \left(\frac{\partial g''}{\partial r_1}\right) = g''^0(x'', y'').
\end{aligned}
\tag{152}
$$

From this point, the equation system of linearized correction equations may be formed as [45]

$$
\mathbf{l} + \mathbf{v} = \mathrm{J}\mathbf{x}, \tag{153}
$$

with the Jacobian matrix $\mathrm{J} \in \mathbb{R}^{\mathrm{m}\times\mathrm{u}}$, $\mathbf{x} \in \mathbb{R}^{\mathrm{u}}$, and $(\mathbf{l},\ \mathbf{v}) \in \mathbb{R}^{\mathrm{m}}$, where m denotes the number of pixels in the image patch, and u is the number of unknown parameters - fourteen in total for this particular implementation. The matching of the two image patches may then be computed iteratively using a standard least squares approach as described in subsection 2.7 via

$$
\left(\mathrm{J}^{\mathsf{T}}\mathrm{P}\mathrm{J}\right)\mathbf{x} = -\mathrm{J}^{\mathsf{T}}\mathrm{P}\mathbf{l}, \tag{154}
$$

where P denotes a weight matrix. If necessary, pixels close to the key point observation or possible dark pixels can be given a specific weight in this matrix. Through each iteration step in (154), the covariance matrix $\Sigma_{\mathbf{Z}}$ may be obtained from [45]

$$\Sigma_{\mathbf{Z}} = \hat{\sigma}_0^2 \left(\mathrm{J}^{\mathsf{T}} \mathrm{P} \mathrm{J} \right)^{-1}, \tag{155}$$

with the variance factor $\hat{\sigma}_0^2$ and residual vector $\mathbf{v}$ defined as

$$\hat{\sigma}_0^2 = \frac{1}{r} \mathbf{v}^{\mathsf{T}} \mathrm{P} \mathbf{v}, \tag{156}$$

$$\mathbf{v} = \mathrm{J}\mathbf{x} - \mathbf{l}, \tag{157}$$

where the redundancy $r = n - u$ is the difference between the number of observations n (i.e., the number of pixels in the patch) and the number of parameters used for the transformation. The advantage of this knowledge is that, from the beginning, key point matching uncertainties within the sensor data are available for further use in the bundle adjustment. Hence, measurements with small uncertainties can be weighted higher than those with larger ones, improving the solution in projective geometry by giving the better measurements more importance. In this way, the overall uncertainties concerning the camera position become smaller as well, and the global solution for the physical parameters of the comet may be obtained with a higher accuracy in the end. The standard deviations

$$\hat{\sigma}_{\Delta \mathrm{x}} = \hat{\sigma}_{a_{00}}, \tag{158}$$

$$\hat{\sigma}_{\Delta \mathrm{y}} = \hat{\sigma}_{b_{00}}, \tag{159}$$

are of particular interest because they describe the precision of the matching location within the two patches. When analyzing contributing parameters in (155), one may generally conclude, that the uncertainties of the match point locations will become larger if less observations are made or more fitting parameters are used. Furthermore, small residuals improve the uncertainties to a smaller value.

Note, that the **image gradients** $\{g_x, g_y\}$ found as a factor in each entry of the Jacobian matrix J in (152) and (155) especially improve the solution to a more accurate result. This may be understood as a measure of distinctiveness between the pixel values, which allows for a more precise geometric transformation and constraint.

For a better explanation, imagine an area on the comet that is flat and produces the same pixel value over the entire image patch to be matched - the precise determination

of a tie point obviously would be impossible, as it could be on any place within the patch. Thus, it is of great interest to search for gradients within the imagery data in order to reduce the tie point uncertainties and, in this way, improve the solution for the respective camera position.
At this point, remember Figure 31 from subsection 3.1.1 - "The Scale Invariant Feature Transform". It becomes clearly visible that **SIFT** is helpful for the detection of key points within areas of the cometary surface that precisely fulfill the requirements for accurate key point matching, since it favors **imagery data that includes the presence of gradients**.

Template Patch Size, Geometric Distortion, and Initial Value Quality

Remember the list of matching quality criteria as introduced in subsection 3.1. The first two items were discussed thoroughly and are covered via the **SIFT detection principle** as well as the **advanced polynomial geometric transformation**.

The third item - the patch size of the template is determined according to publications [99][12][45][26][56][47][107]. The best results could be obtained with small image patches of 20 pixels in size for the Rosetta NAVCAM and 24 pixels for the OSINAC. Note that, depending on the distance between comet and spacecraft, fewer pixels in the patches are used for matching if the resolution decreases.

The fourth point - the amount of geometric distortion between image patches - is purely based on an empirical and statistical approach. First, the cometary surface is irregularly shaped, and thus, geometric distortions can be versatile depending on the location of the tie point or the relative camera positioning. On top of this, estimates of tie point location accuracy, as well as the iterative improvement of the objective function, are available and can be used to discard matches with a large amount of geometric distortion. Last but not least, a statistical approach that is **robust with respect to outliers and corrupted measurements** will be used and give measurements with decreased quality less weight.

However, the last item - **the quality of initial values for the tie point location and orientation** - is important to consider and crucial for a least squares matching result. After the initial localization and matching step is carried out through **SIFT**, the assumption should be that there exists a subpixel accurate estimate for the tie point location within the image patch. Therefore, initial values in terms of shift parameters should already be fairly precise. However, the existence of outliers must still be considered within the data. Hence, the accuracy of initial values obtained from **SIFT** can be

used as an additional measure in order to discard low quality tie points. In other words, the step of additionally applying **polynomial least squares matching** after **SIFT** is a way to confirm good matches for further use or to discard wrong correspondences, such as corrupted measurements caused, for example, by a moving shadow. In practice, a combined threshold from

1. **the cost function convergence ratio**,
2. **uncertainties in both image coordinates, and**
3. **required key point shift**

after least squares matching is used in order to confirm the **SIFT** obtained tie points and simultaneously refine the accuracy of the measurement.

3.1.3. Tie Point Reprojection

After the application of **SIFT** and **polynomial least squares matching**, an additional measure for the tie point quality exists. This measure arises from laws of projective geometry in combination with the question of whether the tie point that was successfully detected between two images can be found in a third, independent image as well. However, this approach does not depend on the quality of the matched tie point alone. First - obviously - the area of the cometary surface containing the key point must be visible and illuminated in the third image. Second, geometric distortion, as well as differences in relative scale, may not be very large. The most important requirement, however, is **the accuracy of available a priori information of the relative position and pointing of the respective camera** for all three images involved. A selection of suitable techniques applicable for small solar system bodies on how to gather sufficient a priori information within the camera matrix parameters will be discussed in subsection 3.1.5.

Remember the reprojection equation (65) from subsection 2.5.5. If after a triangulation, the homogeneous vector of a tie point on the cometary surface is known, it can be reprojected into any image plane in that the point is expected to be visible. After application of the inverse algorithm from (85) through (89), in theory, pixel coordinates should be available and a third, independent image patch can be extracted around these coordinates for least squares matching with simultaneous tie point validation.

However, if the knowledge of the homogeneous coordinate or the accuracy within the respective camera matrix in (65) is insufficient, the now corrupted reprojection will lead to a decreased quality of initial values for least squares matching and thus will not

enable a third, independent, and confirming key point match. All conditions necessary to enable a successful tie point validation via this method will be discussed in the following sections.

3.1.4. Conditions for Triangulation

Figure 38 shows an important geometric relationship that evolves from triangulation. It can be seen that the more parallel the rays are, the less accurate the results from a triangulation can be expected to be. Note however, that this is in direct contrast to what is known to be a good condition for least squares matching.

Remember from subsection 3.1.2 that the less geometric distortion present between two image patches, the greater the likelihood that more accurate matching results can be expected. A low geometric distortion between image patches, however, evolves from small changes in the relative position of the camera, which means that the rays become more parallel, in turn. In other words: as conditions for triangulation improve, the prerequisites for precise key point matching deteriorate. On the contrary, if the rays are too parallel, the least squares matching of an image patch will admittedly have a precise result due to the small geometric distortion. However, the subsequently triangulated tie point may result in a large error in the relative position. If it gets reprojected into a third, independent image, the resulting pixel values may now be too far off, leading to insufficient initial values in order to confirm a good match within the third image.

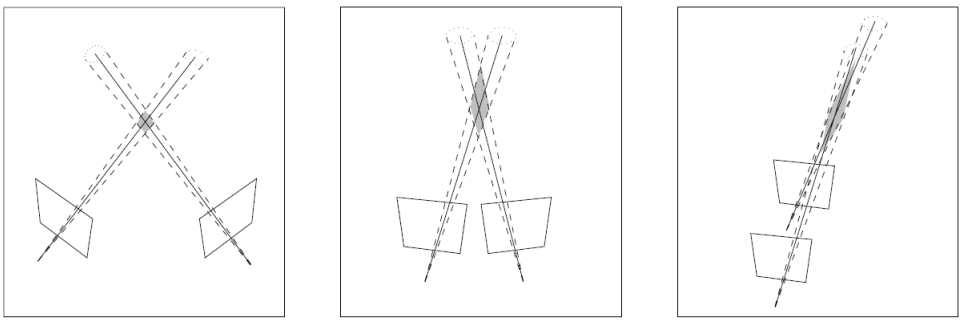

Figure 38: The uncertainty volume of a triangulated point depends on the angular relationship of the pointing direction between two observing cameras as well as on the uncertainty of the respective measurements in pixel space. As the detection line of sight becomes more parallel, the uncertainty volume increases [52].

Therefore, the combination of **least squares matching** with **triangulation and reprojection** for tie point validation through additional, independent measurements

provides a good compromise between sufficient matching conditions and relative collocation for the subsequent three-dimensional structure estimation process. If the final result after a full **matching, triangulation, and reprojection** leads to pixel values that enable the extraction of a suitable image patch in independent images, the conditions for all three operations obviously were sufficient and within limits. In this way, the key point can successfully be confirmed as stable and repeatedly observable. **Therefore, key points that cannot be confirmed in at least one additional image through the method described above are rejected**. The a priori knowledge of camera parameters is also confirmed through this approach, since the camera pose is crucial for the triangulation and reprojection result.

3.1.5. A Priori Knowledge for the Camera Pose

One important requirement for the above description of tie point matching and acquisition is **sufficient a priori knowledge of the camera pose**. If prior to the application of the **FDAM** algorithm only the images are available without additional information, the method cannot be used, as described, in combination with triangulation and reprojection, because of lacking geometric information. Hence, some enabling steps prior to that procedure are necessary, depending on the available data within the respective small body mission. Multiple approaches exist in order to achieve the necessary preconditions for **FDAM**.

SPICE Kernels

Spice (**S**pacecraft, **P**lanet, **I**nstrument, **C**-Matrix, **E**vent) is a software package that has been developed by the Navigation Ancillary Information Facility (**NAIF**) as part of the Jet Propulsion Laboratory (**JPL**). Kernels are accessible for multiple missions within this framework, providing a multitude of useful information. One excerpt of available information within the kernels is the position and orientation of reference frames that have been defined for a respective mission, such as spacecraft or instrument frames. Thus, for example, at a specific value in Ephemeris Time, the position and orientation of the Navcam instrument frame is accessible for the Rosetta mission.

This information can be used to obtain a camera matrix as described in (67) and carry out the triangulation and reprojection operation as previously described. The data available through Spice kernels showed a high degree of accuracy in order to support **FDAM** in the acquisition of tie point matches. The necessity for correction of triangulated and reprojected tie points within the imagery data was well within 5 pixels

for the majority of tie points. Reprojection was also applied with surface points available from shape models to validate the accuracy of the spacecraft orientation and the orbit described through SPICE. In Figure 40, an example of the difference between reprojected and corrected tie points is given. Prior to the application of **FDAM**, additional steps to increase the accuracy of the available orbit data were not necessary. **Thus, SPICE kernel obtained data is used for all required initial values within this work.** More information will be provided in section 4.

Optical Data Alone

Reconstruction of the relative spacecraft position and the surface points is also possible from images of the target body alone, without any amplifying data available prior to the first estimation step. A common starting point is to use **S**peed **U**p **R**obust **F**eatures (**SURF**) - a method that is very similar to **SIFT** in its working principle, however, it has a significantly decreased cost in terms of computation time while only minor degradations in accuracy must be expected [9]. It is accessible, for example, in MATLAB. With **SURF**, a large number of tie point matches can be obtained between multiple images in a fairly short period of time. Key points detected within one single image can be matched to multiple observations in consecutive images. Hence, tie points can already be measured in more than just two views, allowing for a first multiple view geometry estimate.

This set of tie point correspondences may still contain a fairly high amount of outliers. However, in [52] a method is described that allows to get an estimate of an essential matrix from tie point matches in the presence of outliers. By using a **ran**dom **sa**mple **c**onsensus (**RANSAC**) algorithm, randomly chosen sets of tie point correspondences are initially selected. For each set of correspondences, a linear system of equations that results from the epipolar constraint $\hat{\mathbf{x}}'^{\mathsf{T}}\mathrm{E}\hat{\mathbf{x}} = 0$ can be solved. Starting with one pair of points $\hat{\mathbf{x}} = (\hat{x}, \hat{y}, 1)^{\mathsf{T}}$ and $\hat{\mathbf{x}}' = (\hat{x}', \hat{y}', 1)^{\mathsf{T}}$, the epipolar constraint can be written as [52]

$$\hat{x}'\hat{x}e_{11} + \hat{x}'\hat{y}e_{12} + \hat{x}'e_{13} + \hat{y}'\hat{x}e_{21} + \hat{y}'\hat{y}e_{22} + \hat{y}'e_{23} + \hat{x}e_{31} + \hat{y}e_{32} + e_{33} = 0. \tag{160}$$

It follows that for a set of n correspondences, the linear set of equations can be written as [52]

$$\mathrm{A}\mathbf{e} = \begin{bmatrix} \hat{x}'_1\hat{x}_1 & \hat{x}'_1\hat{y}_1 & \hat{x}'_1 & \hat{y}'_1\hat{x}_1 & \hat{y}'_1\hat{y}_1 & \hat{y}'_1 & \hat{x}_1 & \hat{y}_1 & 1 \\ \vdots & \vdots & \vdots & \vdots & \vdots & \vdots & \vdots & \vdots & \vdots \\ \hat{x}'_n\hat{x}_n & \hat{x}'_n\hat{y}_n & \hat{x}'_n & \hat{y}'_n\hat{x}_n & \hat{y}'_n\hat{y}_n & \hat{y}'_n & \hat{x}_n & \hat{y}_n & 1 \end{bmatrix} \mathbf{e} = \mathbf{0}, \tag{161}$$

where $\mathbf{e}$ denotes the vector of arrayed matrix elements e_{ij} of the essential matrix E. By solving this linear system of equations for at least 8 measurements, a first estimate of an essential matrix can be obtained. Remember from subsection 2.5.8, that two singular values of the essential matrix must be equal and the third one equals zero. Since the measurements in (161) are expected to be affected by noise, the result will not exactly fulfill this requirement. However, since the SVD of the obtained essential matrix is given by $\mathrm{E} = \mathrm{U}\mathrm{D}\mathrm{V}^{\mathsf{T}}$, where $\mathrm{D} = \mathrm{diag}\,(a, b, c)$ with $a \geq b \geq c$, an essential matrix $\hat{\mathrm{E}} = \mathrm{U}\hat{\mathrm{D}}\mathrm{V}^{\mathsf{T}}$ may be found by setting $\hat{\mathrm{D}} = \mathrm{diag}\,((a+b)/2, (a+b)/2, 0)$. This matrix $\hat{\mathrm{E}}$ fulfills the requirements of an essential matrix and simultaneously is the closest Frobenius norm solution to the matrix E that was initially obtained from (161). The Frobenius norm of the difference between the two matrices is defined as [52]

$$\left\|\mathrm{E} - \hat{\mathrm{E}}\right\|_{\mathrm{F}} = \sqrt{\sum_{i=1}^{m}\sum_{j=1}^{n}(e_{ij} - \hat{e}_{ij})^2}. \tag{162}$$

For each randomly chosen set of tie point correspondences, this procedure is repeated, and the resulting essential matrix $\hat{\mathrm{E}}$ is used to evaluate the epipolar constraint for **all** acquired tie point matches between the two images. In this way, outliers can be identified iteratively and rejected. In the end, an essential matrix that provides a maximum likelihood estimate can be obtained from a least squares solution from all measurements that remain in the selection.

This method can be used to obtain first estimates of essential matrices between multiple image pairs, improving the knowledge in relative geometry iteratively and rejecting most corrupted measurements with the help of epipolar constraints. After a first estimate of an essential matrix exists, in the next step, the matrix can be decomposed, and camera matrices can be obtained as described in subsection 2.5.8 (Figure 20).

The intermediate result now represents multiple estimates of camera poses as well as all tie point measurements within the imagery data, still including a specific amount of outliers. However, in subsection 3.2.7, a robust algorithm is introduced that produces accurate geometric results despite the presence of outliers.

Summarized, the usage of **SURF** together with **RANSAC** followed by **essential matrix decomposition** and **robust bundle adjustment** allows for the estimation of initial values to let **FDAM** begin producing more accurate results in a second iteration. If orbit reconstruction from optical data without a priori information is desired, this initial iteration step becomes necessary. However, for the Rosetta mission, SPICE kernels already deliver products with a high degree of accuracy. Regarding the reconstruction from optical data alone, a lot of possibilities and techniques are described in [52].

3.1.6. Block Matching and Light Correction

One goal for this work is to find maximum repeatable key points with a high number of possible observations. In fact, from a statistical point of view, the more observations of a tie point that can be made from multiple views, the smaller uncertainties can be expected in both the tie point position as well as the camera pose. Therefore, multiple observations are desired.

In parallel, however, a minimum of elevation or shape modeling is desired, since **the cometary surface and elevation was undergoing significant changes** throughout the mission as introduced in section 1 and analyzed in [29].

In order to achieve this goal, a good compromise is a **block matching of multiple image patches with basic light correction**. As described in subsection 3.1.3, a tie point can be triangulated and reprojected into multiple image planes after its successful detection and matching (Figure 39 left side).

As described in subsection 3.1.2, within the full image patch coordinates, a function $x'' = f_x(x', y'), y'' = f_y(x', y')$ is available and describes the geometric transformation **for each pixel** of the patch. Consequently, surface point triangulation is not only possible at the center of the image patch. A predefined number of points located on the outer edge of the reference patch can be triangulated in addition to the actual tie point located at the center.

These points define a reference grid and, therefore, can be used to obtain a first estimate of the relative orientation of the surface patch with respect to the observing camera (Figure 39, right side).

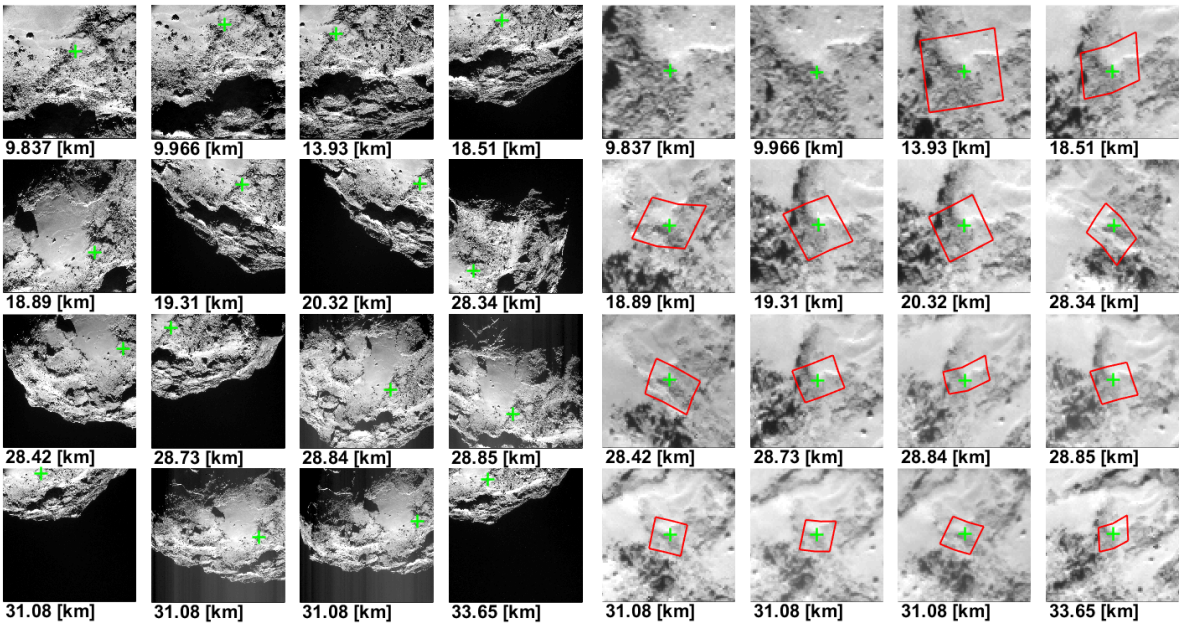

Figure 39: **Left:** Triangulated and reprojected tie point, acquired through **SIFT** from the two images in the left upper corner, taken at closest distance. The reprojected observations can be seen from different views. **Right:** Final tie point matches (green) obtained with the **FDAM** algorithm, covering differences in scale from 9.8km up to 33.7km target center distance. The reference grid (red) highlights the differences in relative scale and orientation. The images were acquired during the prelanding and the comet escort phase by the Rosetta NAVCAM between September 2014 and January 2015.

Knowledge about the relative orientation of the observed surface area within the image patch is valuable for two main reasons. First, in conjunction with the assumption of a specific reflectance function, slopes for each pixel value of the image patch may be estimated, if the relative direction of sunlight incidence is known. Second, as previously introduced, the knowledge of initial values is essential for a successful least squares matching. With the triangulation and reprojection of the reference grid into an additional image, not only the shift parameters are known for initial values, but also an affine transformation can be predefined through start values. Thus, rotation and linear stretching of the patch are already preconditioned. **This technique significantly improved the number of successful match acquisitions** through various scales and geometric distortions (Figure 46). Figure 40 shows subpixel-accurate tie point matches over significant scale differences, corresponding to the image patches extracted from Figure 39. Still, a minor amount of outliers can affect the solution. This remaining percentage of corrupted measurements will be covered through a robust statistical approach within the bundle adjustment. More information on the average performance of **FDAM** will be given in section 4.

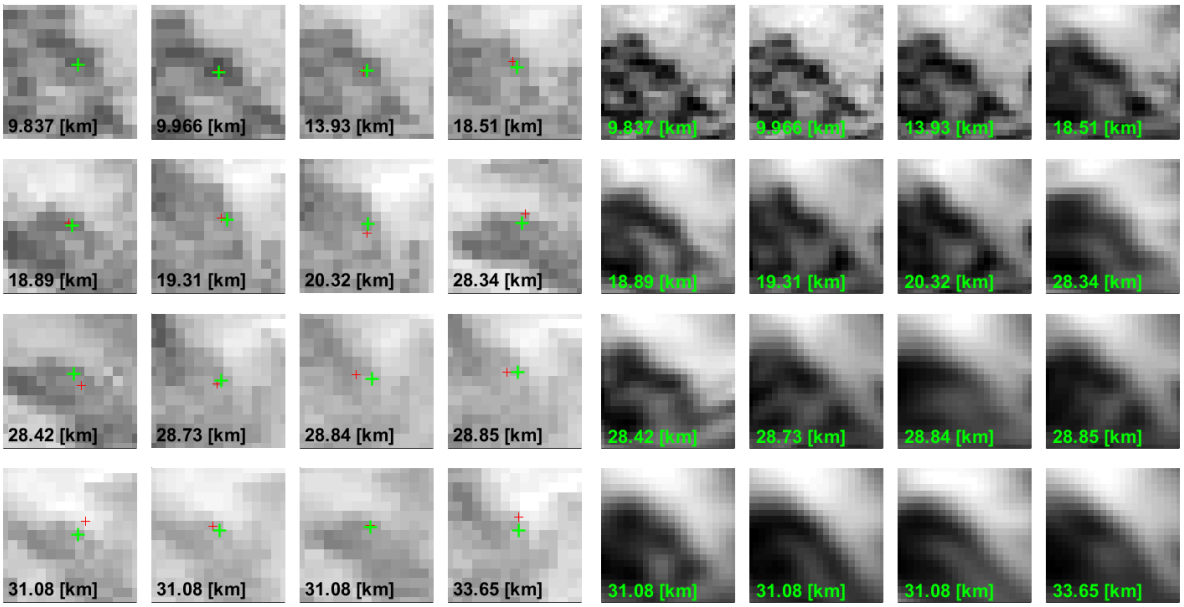

Figure 40: **Left:** Point reprojection (red) and least squares matching corrected tie point measurement (green) within the extracted image patch. **Right:** Geometrically transformed image patches, resulting in the tie point measurement. It can be seen how changes in resolution affect the solution.

Reflectance Models

After a block of multiple image patches through various scales and rotations was successfully matched as described above, changing illumination conditions can still affect the accuracy of the solution. Here, a physical model that allows for the prediction of projected pixel brightness can improve the accuracy within the location of the tie point. Imagine an illuminated sphere as illustrated in Figure 41. If the observing camera and the sphere remain stationary between two consecutive images, the angle of sunlight incidence, however, changes clockwise by 90 degrees, the maximum brightness caused by the reflection from that feature would now appear on top of the projection instead of on the left side, as currently illustrated. Hence, the maximum greyvalue will be measured somewhere different within the CCD, even if the sphere itself is still located at the same relative position; this can lead to an offset in the measured position of the tie point, despite nothing has changed except for the illumination conditions.

The basic idea concerning how to overcome this problem is to have some model that predicts where the maximum brightness would appear if the changes in relative illumination were known. To be precise, not only the new position of the maximum but also the entire distribution of greyvalues depending on altering illumination conditions

are of interest here. Thus, the necessity of knowledge about reflectance depending on surface characteristics, as well as relative geometry of the camera and the Sun, becomes apparent. In principle, the reprojected brightness $\mathbf{I_k}(\mathbf{x})$ within a pixel may be written as [38][24]

$$\mathbf{I_k}(\mathbf{x}) = \mathbf{\Lambda_k}\mathbf{a}(\mathbf{x})\mathbf{R}\left(\alpha, i, e\right) + \mathbf{\Phi_k}, \tag{163}$$

where $\mathbf{\Lambda_k}$ is a multiplier for the scaling of the imagery data, $\mathbf{a}(\mathbf{x})$ is the surface albedo, and $\mathbf{\Phi_k}$ is a background term that can be added to compensate for background haze. $\mathbf{\Lambda_k}$ is a function of the Sun distance, camera conversion, and the integration time for the respective image. The camera conversion depends on how the intensity of the incoming flux on the pixel CCD is converted to the pixel signal rate. However, a linear contrast stretching is already estimated for the whole image patch block through parameters $\{r_0, r_1\}$ in (146). The phase angle together with the surface albedo is assumed constant over the small image patch. No additional phase dependency is necessary, since only relative brightness is used. Thus, for simplicity of the algorithm, no parameter estimation for $\mathbf{\Lambda_k}$, $\mathbf{a}(\mathbf{x})$ and $\mathbf{\Phi_k}$ in (163) is carried out. Only two parameters describing the slopes within the reflectance function are estimated for each pixel of the previously aligned patch block.

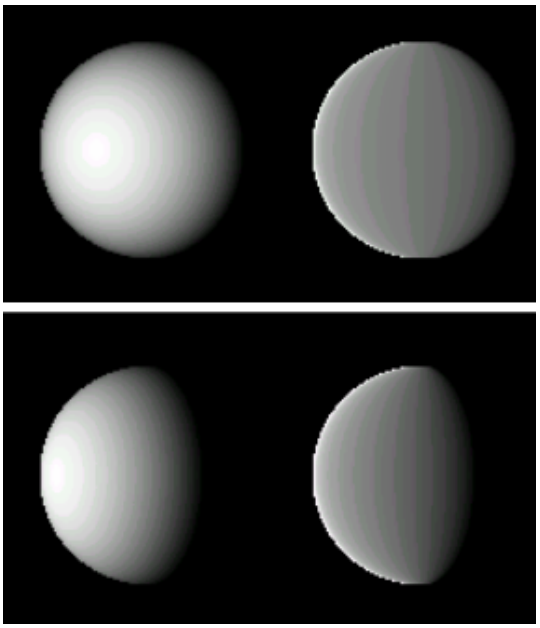

Figure 41: Lambertian reflectance model on the left, Lommel-Seeliger reflectance on the right with phase angles $\alpha = 30°$ top and $\alpha = 60°$ bottom [35].

In general, $\mathbf{R}\left(\alpha, i, e\right)$ depends on three angles that are important quantities whenever **photoclinometry** is used (Figure 42). The **angle of incidence** i is the angle between the surface normal $\mathbf{n}$ and the incidence vector $\mathbf{i}$ towards the Sun. The **angle of emission** e is the angle between the surface normal $\mathbf{n}$ and the vector $\mathbf{e}$ that points towards the observing camera. Another important quantity is the **phase angle** α, which is defined as the angle between sunlight incidence $\mathbf{i}$ and reflected photons towards the camera vector $\mathbf{e}$.

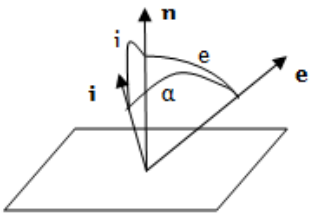

Figure 42: Definition of angles on a surface element [24].

In order to describe the amount of sunlight reflected depending on the three angles, many reflectance models exist. Lambertian reflectance $\mathbf{R_L}$ and Lommel-Seeliger reflectance $\mathbf{R_{LS}}$ are defined as [24]

$$\begin{aligned} \mathbf{R_L}(i) &= \mathbf{n} \cdot \mathbf{i} = \cos(i), \\ \mathbf{R_{LS}}(i,e) &= \frac{\mathbf{n} \cdot \mathbf{i}}{\mathbf{n} \cdot (\mathbf{i} + \mathbf{e})} = \frac{\cos(i)}{\cos(i) + \cos(e)}, \end{aligned} \tag{164}$$

where Lambertian reflectance only depends on the angle of incidence and models pure diffuse reflection. $\mathbf{R_{LS}}$ additionally depends on the angle of emission. The effects of the two reflectance functions are illustrated in Figure 41. The reflectance of a surface element may now be expressed as a linear combination $\mathbf{R}(\alpha, i, e)$ of the two reflectance functions. It can be written as

$$\mathbf{R}(\alpha, i, e) = (1 - \mathrm{L}(\alpha))\,\mathbf{R_L}(i) + \mathrm{L}(\alpha)\,\mathbf{R_{LS}}(i, e), \tag{165}$$

where McEwen's lunar L-function in (165) can be approximated by [38][21][23]

$$\mathrm{L}(\alpha) = e^{-\left(\frac{\alpha}{60}\right)}. \tag{166}$$

This describes a gradual transition from Lambertian reflectance to Lommel-Seeliger reflectance, depending on the phase angle α.

The orientation of the surface normal $\mathbf{n}$ must be known in order to predict pixel brightness from the two reflectance terms. It can be described from two parameters: the slopes $\nabla h = \mathbf{t} = (t_1, t_2)$ within the part of cometary surface that is visible in each

pixel of the image patch block. If the slopes are known, the surface normal can be obtained from

$$\mathbf{n} = -\left(1 + {t_1}^2 + {t_2}^2\right)^{-\frac{1}{2}} \begin{bmatrix} \mathrm{t}_1 \\ \mathrm{t}_2 \\ -1 \end{bmatrix}. \tag{167}$$

The cosine that results from the two angles of incidence i and emission e in (164) may be expressed as [38]

$$\begin{aligned} \cos(i) &= \frac{i_3 - i_1 t_1 - i_2 t_2}{(1 + {t_1}^2 + {t_2}^2)^{\frac{1}{2}}}, \\ \cos(e) &= \frac{e_3 - e_1 t_1 - e_2 t_2}{(1 + {t_1}^2 + {t_2}^2)^{\frac{1}{2}}}. \end{aligned} \tag{168}$$

It follows that $\mathbf{R}(\alpha, i, e)$ in (165) only depends on the a priori knowledge about the vectors towards the Sun and the spacecraft together with the slopes $\nabla h = \mathbf{t} = (t_1, t_2)$. With all the definitions and terms described above, for each pixel within the aligned patch block, the slopes (t_1, t_2) can be estimated while minimizing the difference between predicted and measured pixel brightness. After this procedure, a map of the slopes exists that describes projected pixel brightness based on (163). Hence, a full height map can be reconstructed by solving for the linear system of equations [24][63][74]

$$\begin{aligned} t_{1(i,j)} &= \frac{h_{i-2,j} - 4h_{i-1,j} + 3h_{i,j}}{2\Delta}, \\ t_{2(i,j)} &= \frac{h_{i,j-2} - 4h_{i,j-1} + 3h_{i,j}}{2\Delta}, \end{aligned} \tag{169}$$

where Δ denotes the distance between two adjacent points along the coordinates of the height map grid. However, within this work, generally **no full map reconstruction from photoclinometry is carried out**. The knowledge of the slopes is only used to have a prediction available of what greyvalues can be expected in pixels that show the same area of cometary surface within a different image with altering illumination conditions. The least squares matching process as described in subsection 3.1.2 in principle does not change within this approach; however, the reference patch with highest resolution on the bottom of the block now has greyvalues which are **adapted to the altering illumination conditions of the other patches**. With this method implemented, the uncertainties of the tie point measurement can be reduced, however, this heavily depends on the amount of changes in $\{\alpha, i, e\}$. If the illumination conditions remain similar, no major improvements can be expected while computational cost is still

increased. For this reason, the user of the **FDAM** software package can choose whether the light correction according to (165) is favorable for a specific problem or not and disable or enable the option prior to the computation process. For all NAVCAM images that were processed within this work, the light correction method was successfully applied. Figure 43 shows the improvement in uncertainties along the image coordinates together with the decrease of the objective function through the application of light correction to 3000 test measurements.

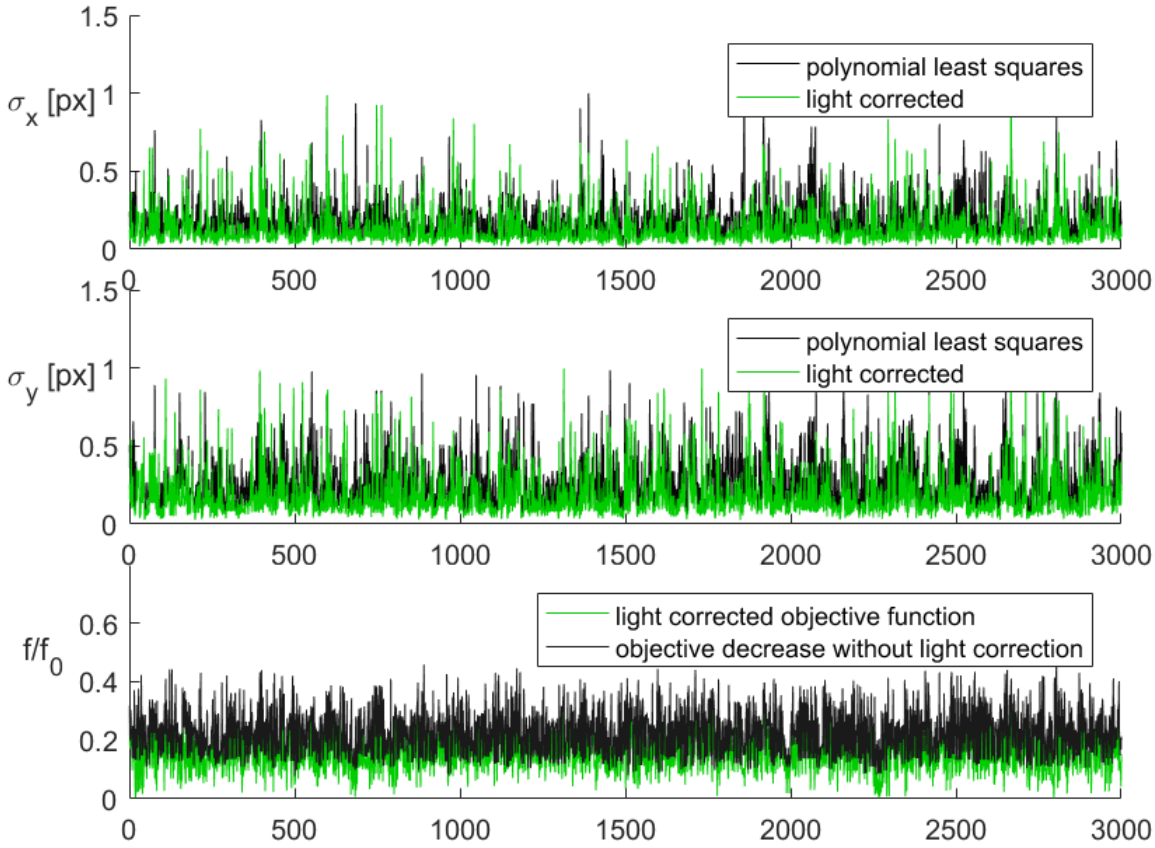

Figure 43: The upper two subplots: Uncertainties in pixel coordinates along the image dimensions with (green) and without (black) light correction according to (165). It can be seen, that for some measurements, there is a significant improvement, whereas for others there is almost none due to small changes in illumination conditions. Bottom: Improvement in the decrease of the objective function.

With light correction, the tie point uncertainties on average **decreased to about 65%** in comparison to the tie point matches obtained without it. The objective function on average **decreased to about 75%**. The cost in terms of computation time is about **twice the time required** to obtain tie point matches from polynomial least squares matching alone.

As introduced before, a full reconstruction is also possible using this method. How-

ever, additional assumptions and model parameters are then necessary. In particular, changing surface conditions - which are to be expected at a comet - are problematic. Nevertheless, especially if surface reconstruction or digital elevation models are desired, **stereophotoclinometry** leads to favorable results [19][16]. Thus, the software package **FDAM** at least provides a small additional tool that allows for basic reconstruction using **stereophotoclinometry**. Figures 44 and 45 show the comparison between measured and simulated projected pixel brightness together with the corresponding estimate of an elevation model.

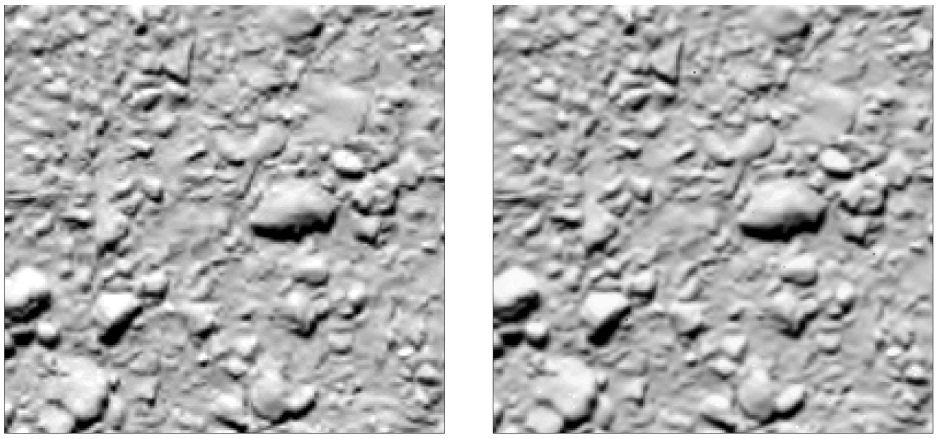

Figure 44: Left: OSINAC image patch original. Right: Reprojected brightness model from Lambertian and Lommel-Seeliger reflectance.

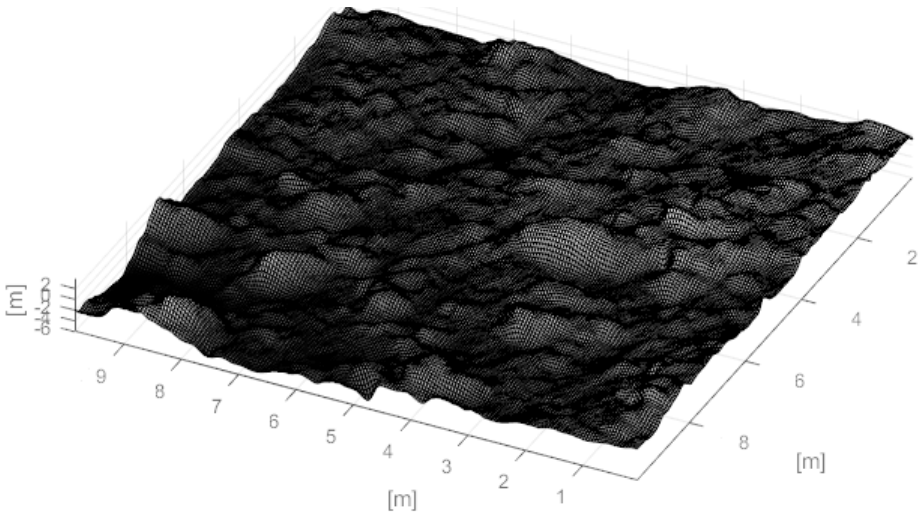

Figure 45: Reconstruction of cometary surface from OSINAC 2016 final descent images with a resolution of 5cm. Changing illumination conditions from various directions can be simulated using the slopes in this model.

The result was obtained from images acquired by the OSINAC during the phase of Rosetta's final descent in September 2016. The small maplet is processed from fifteen consecutive images and has a resolution of 5cm per pixel. The image patch has a size

of about 10×10 meters and thus reveals cometary surface properties at a high level of detail. The corresponding reconstruction of the cometary surface could be obtained with the highest possible resolution and can help to confirm results of the Bistatic Radar Experiment by enabling the estimation of surface roughness at a centimeter level.

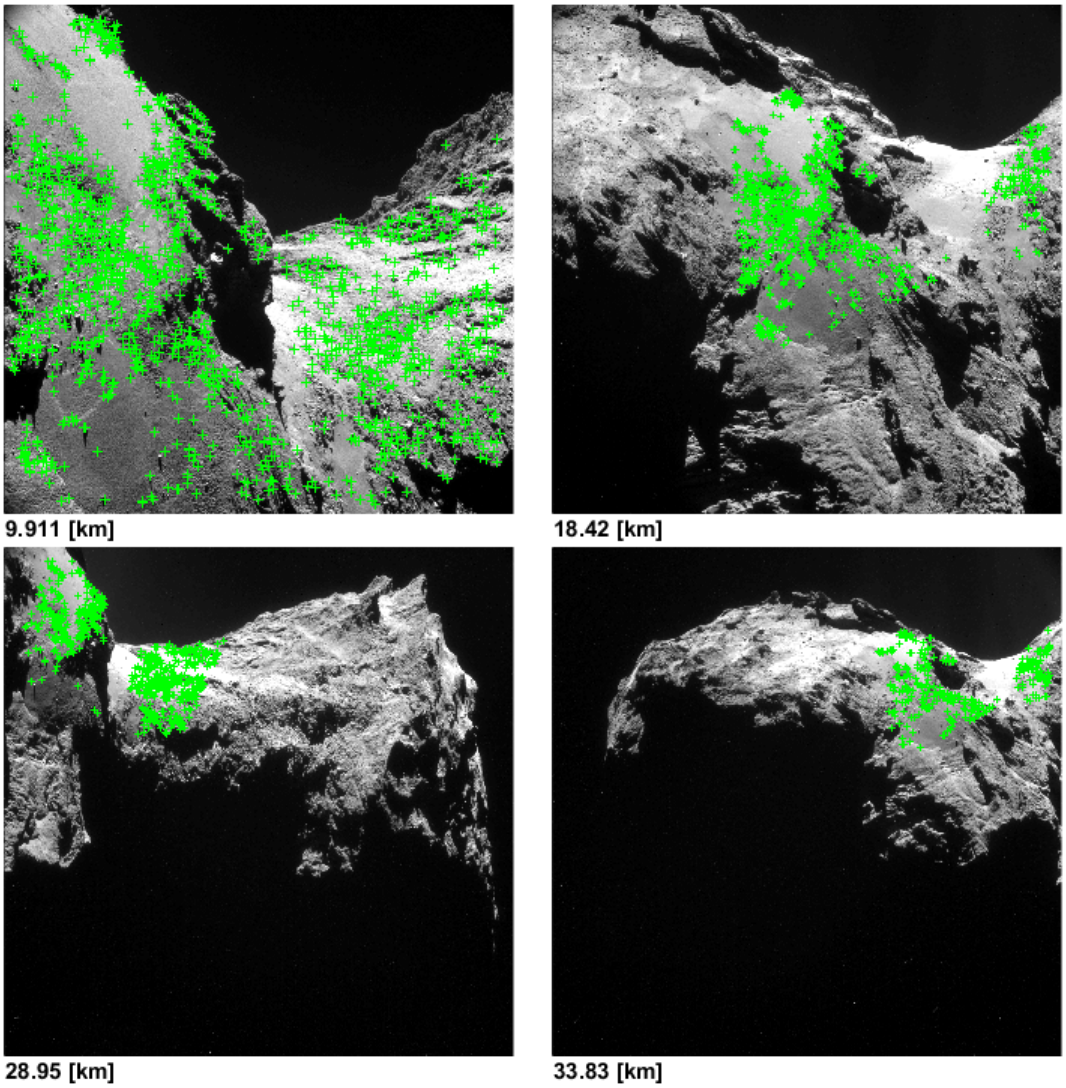

Figure 46: Tie point measurements on the cometary surface obtained from **FDAM** in 2014. The method provides robust results covering different angles and distances. Within the images at greater distances, only the corresponding tie-points to the first image are shown.

In the case of the gravitational field determination, however, only the precise camera positions are of interest. Therefore, within **FDAM**, the prediction of greyvalues is used only to account for changing illumination conditions. Three-dimensional reconstruction is carried out from **stereophotogrammetry** alone. The most promising method to achieve this goal is **bundle adjustment**, which will be thoroughly explained in the

next subsection. Figure 46 shows a final example of results obtained from **FDAM**.

3.2. Robust Bundle Adjustment

After the imagery data has been processed as described in subsection 3.1, the next step is the estimation of relative geometry between camera positions and tie points on the cometary surface. As a prerequisite, there exists the **FDAM** derived measurement vector with column entries

- tie point number $i \in \mathbb{N}$ with $i = (1, 2, ..., n)$,
- image number $j \in \mathbb{N}$ with $j = (1, 2, ..., m)$,
- image plane measurement $\mathbf{x}_{ij} \in \mathbb{R}^2$ in x- and y-direction, pixel coordinates,
- image plane measurement $\mathbf{z}_{ij} \in \mathbb{R}^2$ in x- and y-direction, normalized coordinates,
- 1σ uncertainty in x-direction,
- 1σ uncertainty in y-direction,

for each measurement. The normalized coordinates are obtained from (85) through (89) for all NAVCAM images and (71) for OSINAC images, respectively, since OSINAC Level 4 products are already corrected for nonlinear distortion. Additionally, **start values** are available for both the **surface points** and the **camera matrices** from triangulation and SPICE.

In this subsection, an additional notation standard is introduced, because vectors and matrices are arrayed. A partitioned vector $\mathbf{X} \in \mathbb{R}^{m*n}$ of sub-vectors $\mathbf{x}_i \in \mathbb{R}^n$ will be written capitalized and bold as

$$\mathbf{X} = \left(\mathbf{x}_1^\mathsf{T}, \mathbf{x}_2^\mathsf{T}, \cdots, \mathbf{x}_m^\mathsf{T}\right)^\mathsf{T}. \tag{170}$$

Arrayed matrices remain capitalized non-bold and can be written as

$$\left[\mathrm{A}_1^\mathsf{T}, \mathrm{A}_2^\mathsf{T}, \ldots, \mathrm{A}_n^\mathsf{T}\right]^\mathsf{T} = \begin{bmatrix} \mathrm{A}_1 \\ \mathrm{A}_2 \\ \vdots \\ \mathrm{A}_n \end{bmatrix}, \ \mathrm{diag}\left(\mathrm{A}_i\right) \coloneqq \begin{bmatrix} \mathrm{A}_1 & 0 & \cdots & 0 \\ 0 & \mathrm{A}_2 & \ddots & \vdots \\ \vdots & \ddots & \ddots & 0 \\ 0 & \cdots & 0 & \mathrm{A}_n \end{bmatrix}. \tag{171}$$

Consider the set of 3D points on the cometary surface $\mathbf{x}_i$, which is viewed by a set of cameras with matrices P_j. Denoted by $\mathbf{z}_{ij}$, the coordinates of the i-th point are seen by the j-th camera. The objective is then to solve the following reconstruction problem: Given the set of image coordinates $\mathbf{z}_{ij}$ obtained through **FDAM**, find the set of camera matrices P_j and points $\mathbf{x}_i$ such that $\mathbf{z}_{ij} = \mathrm{P}_j \mathbf{x}_i$.

However, the reprojection will not exactly match the measurement $\mathbf{z}_{ij}$, since the image measurements are noisy. Hence, the goal is to estimate camera matrices and 3D points, which project to the image plane and simultaneously minimize the 2D distance between the reprojected and measured image points for each view in which the 3D point appears. The iterative estimation of structure through minimization of the **reprojection error** [52]

$$\epsilon_{ij} = \mathbf{z}_{ij} - \mathrm{P}_j \mathbf{x}_i, \tag{172}$$

$$\min \sum_{ij} \|\epsilon_{ij}\|_2^2, \tag{173}$$

is called **bundle adjustment** – the simultaneous adjustment of a bundle of rays between each camera center and the set of 3D points. This method provides a **maximum likelihood estimate** for both the surface point and the camera positions. Additionally, the method allows for the assignment of individual covariances to each measurement and can include estimates of a priori information and constraints on camera parameters or point positions.

However, depending on the number of tie points and views, the bundle adjustment framework can rapidly grow to become a large minimization problem because of the number of parameters involved. Nevertheless, the method still runs quite efficiently when implemented carefully. Since the pose of one single view has no influence on the measurements in consecutive images, one may take advantage of the lack of interaction between parameters. Hence, computational cost can be reduced significantly through the generation of sparsity patterns within the iterative solver. All related considerations and implementation details will be discussed in the next subsection.

3.2.1. Sparse Bundle Adjustment Framework

Remember from subsection 2.7 that the augmented normal equations for the Levenberg-Marquardt iteration method with the regularization parameter λ can be formulated as

$$\left(\mathrm{J}^{\mathsf{T}}\Sigma_{\mathbf{Z}}^{-1}\mathrm{J}+\lambda\mathrm{I}\right)\Delta=-\mathrm{J}^{\mathsf{T}}\Sigma_{\mathbf{Z}}^{-1}\epsilon, \tag{174}$$

where J denotes the Jacobi-matrix $\partial\mathbf{f}/\partial\mathbf{P}$, and ϵ is the vector of residuals defined by $\epsilon=\mathbf{f}\left(\mathbf{P}\right)-\mathbf{Z}$. Here, $\mathbf{Z}$ denotes the arrayed measurement vector and $\mathbf{P}$ the arrayed parameter vector of the nonlinear projective model defined by a function $\mathbf{f}\left(\mathbf{P}\right)$. The accuracy of the measurement vector $\mathbf{Z}$ is essential for the accurate determination of camera positions. A measure for this is the variance σ^2, which can be found in the main diagonal of the measurement vector's associated covariance matrix $\Sigma_{\mathbf{Z}}$, obtained from (155).

The function $\mathbf{f}\left(\mathbf{P}\right)$ includes the projective camera model (74) as well as minimum parametrizations of homogeneous 3D-points and camera parameters, such as rotations and translations.

Consider, that the parameter vector $\mathbf{P}$ may be partitioned into arrayed vectors $\mathbf{A}$ and $\mathbf{B}$ with $\mathbf{P}=\left(\mathbf{A}^{\mathsf{T}},\mathbf{B}^{\mathsf{T}}\right)^{\mathsf{T}}$, where $\mathbf{A}$ relates to those parameters describing all the camera poses, whereas $\mathbf{B}$ relates to the description of 3D surface points. The goal is then to find parameters $(\mathbf{A},\mathbf{B})$ that minimize the objective function $F\left(\mathbf{A},\mathbf{B}\right)=\sum_{ij}\left\|\epsilon_{ij}\right\|_2^2$. With the subdivision of the parameters $\mathbf{P}=\left(\mathbf{A}^{\mathsf{T}},\mathbf{B}^{\mathsf{T}}\right)^{\mathsf{T}}$, the Jacobian may also be divided into Jacobian submatrices [52]

$$\begin{aligned}\mathrm{A}&=\left[\frac{\partial\hat{\mathbf{Z}}}{\partial\mathbf{A}}\right],\\ \mathrm{B}&=\left[\frac{\partial\hat{\mathbf{Z}}}{\partial\mathbf{B}}\right],\end{aligned} \tag{175}$$

where $\hat{\mathbf{Z}}=\mathbf{f}\left(\mathbf{P}\right)$ denotes the reprojected normalized tie point coordinates depending on parameters $(\mathbf{A},\mathbf{B})$. The linear system of equations $\mathrm{J}\Delta=\epsilon$ can now be written as

$$\mathrm{J}\Delta=\left[\begin{array}{c|c}\mathrm{A}&\mathrm{B}\end{array}\right]\left[\begin{array}{c}\Delta_{\mathbf{A}}\\ \Delta_{\mathbf{B}}\end{array}\right]=\epsilon. \tag{176}$$

From this point, the normal equations of the Gauss-Newton iteration method $\mathrm{J}^{\mathsf{T}}\Sigma_{\mathbf{Z}}^{-1}\mathrm{J}\Delta=-\mathrm{J}^{\mathsf{T}}\Sigma_{\mathbf{Z}}^{-1}\epsilon$ may be formulated as [52]

$$\begin{bmatrix} \mathrm{A}^{\mathsf{T}}\Sigma_{\mathbf{Z}}^{-1}\mathrm{A} & \mathrm{A}^{\mathsf{T}}\Sigma_{\mathbf{Z}}^{-1}\mathrm{B} \\ \mathrm{B}^{\mathsf{T}}\Sigma_{\mathbf{Z}}^{-1}\mathrm{A} & \mathrm{B}^{\mathsf{T}}\Sigma_{\mathbf{Z}}^{-1}\mathrm{B} \end{bmatrix} \begin{bmatrix} \Delta_{\mathbf{A}} \\ \Delta_{\mathbf{B}} \end{bmatrix} = \begin{bmatrix} \mathrm{A}^{\mathsf{T}}\Sigma_{\mathbf{Z}}^{-1}\epsilon \\ \mathrm{B}^{\mathsf{T}}\Sigma_{\mathbf{Z}}^{-1}\epsilon \end{bmatrix}. \tag{177}$$

In order to introduce the regularization parameter λ of the Levenberg-Marquardt method in (174), the main diagonal of this matrix is multiplied by a factor $1+\lambda$. Compared to the normal equations of the Gauss-Newton iteration method, the term $\lambda\mathrm{I}$ is added. When λ is small, the Levenberg-Marquardt algorithm becomes basically the same as the Gauss-Newton method, and the iteration quickly converges in the neighborhood of the solution. However, if λ is large, the augmented normal equations become $\lambda\Delta = -\mathrm{J}^{\mathsf{T}}\Sigma_{\mathbf{Z}}^{-1}\epsilon$, which results in small iteration steps Δ, that converge more carefully towards the solution and eventually lead to a decrease in the cost function.

The matrices complemented by the regularization parameter will be denoted by $\mathrm{U}^* = \left(\mathrm{A}^{\mathsf{T}}\Sigma_{\mathbf{Z}}^{-1}\mathrm{A}\right)^*$ and $\mathrm{V}^* = \left(\mathrm{B}^{\mathsf{T}}\Sigma_{\mathbf{Z}}^{-1}\mathrm{B}\right)^*$. In this way, the notation may be shortened to [52]

$$\begin{bmatrix} \mathrm{U}^* & \mathrm{W} \\ \mathrm{W}^{\mathsf{T}} & \mathrm{V}^* \end{bmatrix} \begin{bmatrix} \Delta_{\mathbf{A}} \\ \Delta_{\mathbf{B}} \end{bmatrix} = \begin{bmatrix} \mathrm{A}^{\mathsf{T}}\Sigma_{\mathbf{Z}}^{-1}\epsilon \\ \mathrm{B}^{\mathsf{T}}\Sigma_{\mathbf{Z}}^{-1}\epsilon \end{bmatrix} = \begin{bmatrix} \epsilon_{\mathbf{A}} \\ \epsilon_{\mathbf{B}} \end{bmatrix}. \tag{178}$$

Consider now the measurement vector subdivided into $\mathbf{Z}_j = \left(\mathbf{z}_{1j}^{\mathsf{T}}, \mathbf{z}_{2j}^{\mathsf{T}}, \ldots, \mathbf{z}_{nj}^{\mathsf{T}}\right)^{\mathsf{T}}$ with $\mathbf{Z} = \left(\mathbf{Z}_1^{\mathsf{T}}, \mathbf{Z}_2^{\mathsf{T}}, \ldots, \mathbf{Z}_m^{\mathsf{T}}\right)^{\mathsf{T}}$, where $\mathbf{z}_{ij}$ denotes the measurement of the i-th point in the j-th image. Additionally, consider the partitioning of the parameter vectors $\mathbf{A} = \left(\mathbf{a}_1^{\mathsf{T}}, \mathbf{a}_2^{\mathsf{T}}, \ldots, \mathbf{a}_m^{\mathsf{T}}\right)^{\mathsf{T}}$ and $\mathbf{B} = \left(\mathbf{b}_1^{\mathsf{T}}, \mathbf{b}_2^{\mathsf{T}}, \ldots, \mathbf{b}_n^{\mathsf{T}}\right)^{\mathsf{T}}$ with $\mathbf{P} = \left(\mathbf{A}^{\mathsf{T}}, \mathbf{B}^{\mathsf{T}}\right)^{\mathsf{T}}$ corresponding to the subdivision of the measurement vector $\mathbf{Z}$. Knowing that the projection $\hat{\mathbf{z}}_{ij}$ only depends on the parameters of the j-th camera and the i-th surface point, one may set [52]

$$\begin{aligned} \frac{\partial \hat{\mathbf{z}}_{ij}}{\partial \mathbf{a}_k} &= 0 \text{ unless } j = k, \\ \frac{\partial \hat{\mathbf{z}}_{ij}}{\partial \mathbf{b}_k} &= 0 \text{ unless } i = k, \end{aligned} \tag{179}$$

in the augmented normal equations of the algorithm. This results in the majority of entries in the Jacobian matrices A and B being zero. Thus, a significant improvement concerning computational loads can be achieved by taking advantage of the sparsity

of the linear system of equations. The resulting Jacobian matrices have a predefined sparsity pattern, which will be explained in the following. Referring to (179), one finds that $\mathrm{B}_j = \left[\partial \hat{\mathbf{Z}}_j / \partial \mathbf{B}\right]$ becomes a block diagonal matrix [52]

$$\mathrm{B}_j = \mathrm{diag}\left(\mathrm{B}_{1j}, \mathrm{B}_{2j}, \ldots, \mathrm{B}_{nj}\right), \text{ where } \mathrm{B}_{ij} = \partial \hat{\mathbf{z}}_{ij} / \partial \mathbf{b}_i. \tag{180}$$

Consequently, $\mathrm{A}_j = \left[\partial \hat{\mathbf{Z}}_j / \partial \mathbf{a}_j\right]$ may be arrayed as [78]

$$\mathrm{A}_j = \left[\mathrm{A}_{1j}^{\mathsf{T}}, \mathrm{A}_{2j}^{\mathsf{T}}, \ldots, \mathrm{A}_{nj}^{\mathsf{T}}\right]^{\mathsf{T}}, \text{ where } \mathrm{A}_{ij} = \partial \hat{\mathbf{z}}_{ij} / \partial \mathbf{a}_j. \tag{181}$$

Since the measurements $\mathbf{Z}_j$ are independent and, therefore, uncorrelated, $\Sigma_{\mathbf{Z}_j}$ also has a diagonal structure of the form

$$\Sigma_{\mathbf{Z}_j} = \mathrm{diag}\left(\Sigma_{\mathbf{z}_{1j}}, \Sigma_{\mathbf{z}_{2j}}, \ldots, \Sigma_{\mathbf{z}_{nj}}\right). \tag{182}$$

In the following, an example of five surface points seen in three views will be given. It will be considered that each point is visible in all views. The corresponding Jacobian matrix for a sparse bundle adjustment then has the form

$$
\mathrm{J} = \left[\begin{array}{c|c|c} \mathrm{A} & \mathrm{B} \end{array}\right] = \left[\begin{array}{ccc|ccccc}
\mathrm{A}_{11} & 0 & 0 & \mathrm{B}_{11} & & 0 & \cdots & 0 \\
\mathrm{A}_{21} & & & & \mathrm{B}_{21} & & & \vdots \\
\mathrm{A}_{31} & \vdots & \vdots & 0 & & \mathrm{B}_{31} & & 0 \\
\mathrm{A}_{41} & & & \vdots & & & \mathrm{B}_{41} & \\
\mathrm{A}_{51} & 0 & 0 & 0 & \cdots & 0 & & \mathrm{B}_{51} \\
\hline
0 & \mathrm{A}_{12} & 0 & \mathrm{B}_{12} & & 0 & \cdots & 0 \\
 & \mathrm{A}_{22} & & & \mathrm{B}_{22} & & & \vdots \\
\vdots & \mathrm{A}_{32} & \vdots & 0 & & \mathrm{B}_{32} & & 0 \\
 & \mathrm{A}_{42} & & \vdots & & & \mathrm{B}_{42} & \\
0 & \mathrm{A}_{52} & 0 & 0 & \cdots & 0 & & \mathrm{B}_{52} \\
\hline
0 & 0 & \mathrm{A}_{13} & \mathrm{B}_{13} & & 0 & \cdots & 0 \\
 & & \mathrm{A}_{23} & & \mathrm{B}_{23} & & & \vdots \\
\vdots & \vdots & \mathrm{A}_{33} & 0 & & \mathrm{B}_{33} & & 0 \\
 & & \mathrm{A}_{43} & \vdots & & & \mathrm{B}_{43} & \\
0 & 0 & \mathrm{A}_{53} & 0 & \cdots & 0 & & \mathrm{B}_{53}
\end{array}\right]. \tag{183}
$$

The matrices in the previously defined shortened notation (178) without the regularization factor λ denoted by the * can now be computed with reduced computational cost via

$$
\mathrm{U}_j = \sum_{i=1}^{n} \mathrm{A}_{ij}^{\mathsf{T}} \Sigma_{\mathbf{z}_{ij}}^{-1} \mathrm{A}_{ij}, \quad j = (1, 2, ..., m)\,, \tag{184}
$$

$$
\mathrm{V}_i = \sum_{j=1}^{m} \mathrm{B}_{ij}^{\mathsf{T}} \Sigma_{\mathbf{z}_{ij}}^{-1} \mathrm{B}_{ij}, \quad i = (1, 2, ..., n)\,, \tag{185}
$$

$$
\mathrm{W}_{ij} = \mathrm{A}_{ij}^{\mathsf{T}} \Sigma_{\mathbf{z}_{ij}}^{-1} \mathrm{B}_{ij}. \tag{186}
$$

With the example of five points measured in three views, the left side of the normal equations $\mathrm{J}^{\mathsf{T}} \Sigma_{\mathbf{Z}}^{-1} \mathrm{J}$ then has the form

$$
\mathrm{J}^{\mathsf{T}}\Sigma_{\mathbf{Z}}^{-1}\mathrm{J} = \left[\begin{array}{ccc|cccc}
\mathrm{U}_1 & 0 & 0 & & & & \\
0 & \mathrm{U}_2 & 0 & & \mathrm{W} & & \\
0 & 0 & \mathrm{U}_3 & & & & \\
\hline
 & & & \mathrm{V}_1 & & 0 \cdots & 0 \\
 & & & & \mathrm{V}_2 & & \vdots \\
 & \mathrm{W}^{\mathsf{T}} & & 0 & & \mathrm{V}_3 & 0 \\
 & & & \vdots & & & \mathrm{V}_4 \\
 & & & 0 & \cdots & 0 & \mathrm{V}_5
\end{array}\right]. \tag{187}
$$

Equation (178) is now multiplied from the left by the matrix

$$
\left[\begin{array}{cc} \mathrm{I} & -\mathrm{W}\mathrm{V}^{*-1} \\ 0 & \mathrm{I} \end{array}\right],
$$

which yields

$$
\left[\begin{array}{cc} \mathrm{U}^* - \mathrm{W}\mathrm{V}^{*-1}\mathrm{W}^{\mathsf{T}} & 0 \\ \mathrm{W}^{\mathsf{T}} & \mathrm{V}^* \end{array}\right] \left[\begin{array}{c} \Delta_{\mathbf{A}} \\ \Delta_{\mathbf{B}} \end{array}\right] = \left[\begin{array}{c} \epsilon_{\mathbf{A}} - \mathrm{W}\mathrm{V}^{*-1}\epsilon_{\mathbf{B}} \\ \epsilon_{\mathbf{B}} \end{array}\right]. \tag{188}
$$

Since the top right hand block of the matrix on the left side in the augmented normal equations (188) now has vanished, one may compute first $\Delta_{\mathbf{A}} = \left(\Delta_{\mathbf{a}_1}^{\mathsf{T}}, \Delta_{\mathbf{a}_2}^{\mathsf{T}}, \ldots, \Delta_{\mathbf{a}_m}^{\mathsf{T}}\right)^{\mathsf{T}}$ from

$$
\mathrm{S}\Delta_{\mathbf{A}} = \left(\mathbf{e}_1^{\mathsf{T}}, \mathbf{e}_2^{\mathsf{T}}, \ldots, \mathbf{e}_m^{\mathsf{T}}\right)^{\mathsf{T}}, \tag{189}
$$

where $\mathrm{S} \in \mathbb{R}^{m \times m}$ is a block matrix with blocks S_{jk}

$$\mathrm{S}_{jj} = -\sum_{i=1}^{n} \mathrm{Y}_{ij}\mathrm{W}_{ij}^{\mathsf{T}} + \mathrm{U}_{j}^{*}, \quad j = (1, 2, ..., m)\,, \tag{190}$$

$$\mathrm{S}_{jk} = -\sum_{i=1}^{n} \mathrm{Y}_{ij}\mathrm{W}_{ik}^{\mathsf{T}} \text{ if } j \neq k, \tag{191}$$

$$\mathrm{Y}_{ij} = \mathrm{W}_{ij}\mathrm{V}_{i}^{*-1}. \tag{192}$$

The right side of (189) can be obtained from

$$\mathbf{e}_{j} = \epsilon_{\mathbf{a}j} - \sum_{i=1}^{n} \mathrm{Y}_{ij}\epsilon_{\mathbf{b}i}, \quad j = (1, 2, ..., m)\,, \tag{193}$$

with

$$\epsilon_{\mathbf{a}j} = \sum_{i=1}^{n} \mathrm{A}_{ij}^{\mathsf{T}}\Sigma_{\mathbf{z}_{ij}}^{-1}\epsilon_{ij}, \quad j = (1, 2, ..., m)\,, \tag{194}$$

$$\epsilon_{\mathbf{b}i} = \sum_{j=1}^{m} \mathrm{B}_{ij}^{\mathsf{T}}\Sigma_{\mathbf{z}_{ij}}^{-1}\epsilon_{ij}, \quad i = (1, 2, ..., n)\,. \tag{195}$$

After this step, each $\Delta_{\mathbf{b}_i}$ in turn can be obtained from

$$\Delta_{\mathbf{b}_i} = \mathrm{V}_{i}^{*-1}\left(\epsilon_{\mathbf{b}i} - \sum_{j=1}^{m} \mathrm{W}_{ij}^{\mathsf{T}}\Delta_{\mathbf{a}_j}\right), \quad i = (1, 2, ..., n)\,. \tag{196}$$

3.2.2. Covariance

The associated covariance matrix of the estimated parameters generally can be obtained from the pseudo-inverse

$$\Sigma_{\mathbf{P}} = \left(\mathrm{J}^{\mathsf{T}}\Sigma_{\mathbf{Z}}^{-1}\mathrm{J}\right)^{+}. \tag{197}$$

More information about the pseudo-inverse of a matrix can be found in appendix A.5. For the subsequent orbit determination process, it is important to know the uncertainties of the derived camera positions. Hence, the values on the main diagonal of $\Sigma_{\mathbf{A}}$ are of special interest. They can be obtained from

$$\Sigma_{\mathbf{A}} = \left[\mathrm{U} - \mathrm{W}\mathrm{V}^{-1}\mathrm{W}^{\intercal}\right]^{+}, \tag{198}$$

which equals S^{+}, but without the regularization parameter λ. A more in depth derivation of subsections 3.2.1 and 3.2.2 may be found in [52].

3.2.3. Parametrization Constraints

As formerly discussed, the parameters of the observing camera are estimated simultaneously along with the position of the surface points in the bundle adjustment. To be more precise, the **position** and the **rotation** of the camera - in one word the **camera pose** - concludes the total of six camera parameters $\mathbf{a}_j$ for each view $j = (1, 2, ..., m)$ that need to be adjusted. For the surface points in parallel, there are three coordinates in $\mathbf{b}_i$ per point $i = (1, 2, ..., n)$ that need to be estimated. However, remember from (54), that each camera matrix has twelve entries and the reprojection equation (65) includes the surface points expressed in homogeneous vectors with four entries. Adjusting all these entries as parameters in bundle adjustment would lead to an overparametrized optimization problem.

Imagine that for a given parameter set, a change in the values of the parameters would not necessarily change the underlying projective geometry and thus would have no effect on the cost function. In other words, an infinite number of parameter values would be possible in order to describe the same projective relationship. This problem is called gauge freedom and is thoroughly discussed in [52][82][1].

A good example - as mentioned in section 1 - is the overall scale of an observed scene in homogeneous vectors; it is undetermined and, thus, subject to gauge freedom if the parameter set is not chosen carefully. Gauge freedom in the parametrization of an optimization problem causes the normal equations to be singular and, hence, allows for multiple solutions or leads to a slower convergence. Similarly, evaluating the covariance matrix of an estimated homogeneous vector is without result, unless the scale of the vector is constrained. Therefore, the question about what defines a good parametrization is very important in bundle adjustment. Generally, it should be singularity-free, locally

continuous, differentiable and one-to-one – in other words, a diffeomorphism. Hence, the parametrizations of **camera position**, **camera rotation**, and **surface points** will be explained in the next subsections.

3.2.4. Parametrization of Angle-Axis-Rotations

The idea of the angle-axis representation is about finding a parametrization of rotations in space with only three parameters. The rotation matrix may be defined from a vector $\mathbf{t}$ via the mapping $\mathbf{t} \mapsto \mathrm{R}(\mathbf{t})$ which is obtained from the Euler-function of a skew-symmetric matrix [1][52]

$$\mathrm{R}(\mathbf{t}) = e^{[\mathbf{t}]_\times} = \mathrm{I} + [\mathbf{t}]_\times + \frac{[\mathbf{t}]_\times^2}{2!} + \frac{[\mathbf{t}]_\times^3}{3!} + \frac{[\mathbf{t}]_\times^4}{4!} + ... \tag{199}$$

$$= \mathrm{I} + \|\mathbf{t}\| \left[\hat{\mathbf{t}}\right]_\times + \|\mathbf{t}\|^2 \frac{\left[\hat{\mathbf{t}}\right]_\times^2}{2!} - \|\mathbf{t}\|^3 \frac{\left[\hat{\mathbf{t}}\right]_\times}{3!} - \|\mathbf{t}\|^4 \frac{\left[\hat{\mathbf{t}}\right]_\times^2}{4!} + ... \tag{200}$$

$$= \mathrm{I} + \sin\|\mathbf{t}\| \left[\hat{\mathbf{t}}\right]_\times + (1 - \cos\|\mathbf{t}\|) \left[\hat{\mathbf{t}}\right]_\times^2, \tag{201}$$

where $[\mathbf{t}]_\times^3 = -\|\mathbf{t}\|^2 [\mathbf{t}]_\times = -\|\mathbf{t}\|^3 \left[\hat{\mathbf{t}}\right]_\times$, and $\hat{\mathbf{t}}$ denotes a unit vector in the direction of $\mathbf{t}$. The resulting rotation matrix $\mathrm{R}(\mathbf{t})$ represents a rotation through an angle $\|\mathbf{t}\|$ about the axis defined by the vector $\mathbf{t}$; it fulfills the relation $\mathrm{R}(\mathbf{t})^{-1} = \mathrm{R}(-\mathbf{t})$ for inverse rotations. To find a mapping from a given rotation matrix to the angle-axis representation, reference appendix A.4 definition (239) for

$$\mathrm{tr}\left(\left[\hat{\mathbf{t}}\right]_\times\right) = 0, \tag{202}$$

$$[\mathbf{t}]_\times^2 = \mathbf{t}\mathbf{t}^\mathsf{T} - \|\mathbf{t}\|^2 \mathrm{I}, \tag{203}$$

$$\left[\hat{\mathbf{t}}\right]_\times^2 - \left(\left[\hat{\mathbf{t}}\right]_\times^2\right)^\mathsf{T} = 0. \tag{204}$$

Together with (201), it can be seen that the $\sin\|\mathbf{t}\|$ term can not be found within the main diagonal entries of R. Hence, the angle $\|\mathbf{t}\|$ and the rotation axis $\hat{\mathbf{t}}$ may be determined from

$$2\cos\|\mathbf{t}\| = \mathrm{tr}(\mathrm{R}) - 1, \tag{205}$$

$$2\sin\|\mathbf{t}\|\hat{\mathbf{t}} = (\mathrm{R}_{32} - \mathrm{R}_{23}, \mathrm{R}_{13} - \mathrm{R}_{31}, \mathrm{R}_{21} - \mathrm{R}_{12})^\mathsf{T}, \tag{206}$$

where $\hat{\mathbf{t}}$ denotes the eigenvector corresponding to the unit eigenvalue of R, which can be found via

$$(\mathrm{R} - \mathrm{I})\,\hat{\mathbf{t}} = \mathbf{0}. \tag{207}$$

The angle $\|\mathbf{t}\|$ should be calculated by using a two-argument **arctan** function, for example **atan2**, since computation from **arcsin** or **arccos** alone is numerically unstable. Remember from (65), that homogeneous points on the image plane are calculated via multiplication with the camera matrix P, which contains twice the rotation $\mathrm{R}(\mathbf{t})$. In order to reduce computational load in the bundle adjustment algorithm, the part involving the computation of the full rotation matrix in each iteration step may be omitted. From equation (201), one sees that [52]

$$\begin{aligned}\mathrm{R}(\mathbf{t}) &= \mathrm{I} + \sin\|\mathbf{t}\| \left[\hat{\mathbf{t}}\right]_\times + (1 - \cos\|\mathbf{t}\|) \left[\hat{\mathbf{t}}\right]_\times^2 \\ &= \mathrm{I} + \frac{\sin\|\mathbf{t}\|}{\|\mathbf{t}\|} [\mathbf{t}]_\times + \frac{1 - \cos\|\mathbf{t}\|}{\|\mathbf{t}\|^2} [\mathbf{t}]_\times^2 ,\end{aligned} \tag{208}$$

and, thus, the multiplication of a rotation matrix $\mathrm{R}(\mathbf{t})$ with a vector $\mathbf{x}$ may be carried out without the full derivation of $\mathrm{R}(\mathbf{t})$ via [52]

$$\begin{aligned}\mathrm{R}(\mathbf{t})\,\mathbf{x} &= \left[\mathrm{I} + \frac{\sin\|\mathbf{t}\|}{\|\mathbf{t}\|} [\mathbf{t}]_\times + \frac{1 - \cos\|\mathbf{t}\|}{\|\mathbf{t}\|^2} [\mathbf{t}]_\times^2\right] \mathbf{x}, \\ &= \mathbf{x} + \frac{\sin\|\mathbf{t}\|}{\|\mathbf{t}\|}\mathbf{t} \times \mathbf{x} + \frac{1 - \cos\|\mathbf{t}\|}{\|\mathbf{t}\|^2}\mathbf{t} \times (\mathbf{t} \times \mathbf{x}) .\end{aligned} \tag{209}$$

3.2.5. Parametrization of Homogeneous Vectors from Quaternions

Another method for the parametrization of three-dimensional rotations is given through **quaternions**. However, they can also be a useful tool for the parametrization of homogeneous vectors. The surface of 67P may be described as a set of homogeneous points. A homogeneous vector $\mathbf{q} \in \mathbb{R}^4$ corresponding to a point in 3D space $\mathbf{x} \in \mathbb{R}^3$ may be parametrized through $\mathbf{t}$ by using the quaternion notation [52]

$$\mathbf{t} \leftrightarrow \mathbf{q} = \left[\mathrm{sinc}\left(\frac{\|\mathbf{t}\|}{2}\right)\mathbf{t}^\mathsf{T}, \cos\left(\frac{\|\mathbf{t}\|}{2}\right)\right]^\mathsf{T}. \tag{210}$$

This is a redundant representation in that it contains four parameters where only three need to be adjusted. In this way, and for computational purposes, it is possible to represent homogeneous vectors in projective space with a **minimum number of parameters**, similar to the angle-axis representation for the parametrization of a rotation. The mapping $\mathbf{t} \leftrightarrow \mathbf{q}$ maps the parameters smoothly and one-to-one onto the set of quaternions $\mathbf{q}$. Therefore, it provides an optimal parametrization for homogeneous points in an iterative optimization process like bundle adjustment [52].

In order to find a transformation back from the quaternion notation $\mathbf{q} = (q_1, q_2, q_3, q_4)$ to the vector $\mathbf{t}$, define $\mathbf{q}_{13} \coloneqq (q_1, q_2, q_3)$. Then, together with $\mathbf{q}_{13} = \|\mathbf{q}_{13}\|\hat{\mathbf{q}}_{13}$, $\mathbf{t}$ can be determined through [52]

$$\begin{aligned} \frac{\|\mathbf{q}_{13}\|}{q_4} &= 2\tan\left(\frac{\|\mathbf{t}\|}{2}\right), \\ \mathbf{t} &= 2\frac{\mathbf{q}_{13}}{\|\mathbf{q}_{13}\|}\arctan\left(\frac{\|\mathbf{q}_{13}\|}{2q_4}\right). \end{aligned} \tag{211}$$

3.2.6. Parametrization of the n-Sphere

In this subsection, the parametrization of the camera reference frame's translation is discussed. Remember from subsection 3.2.3 that the overall scale in homogeneous vectors is undetermined and, thus, subject to gauge freedom. Although minimum parametrizations for rotations of the camera and the homogeneous coordinates of tie points on the cometary surface were given through subsections (3.2.4) and (3.2.5), this problem has still not been taken care of up to this point. Consider the result of a bundle adjustment with n points seen in m views

$$\mathrm{P_j} = \left[\ \mathrm{R_j}\ \middle|\ \mathbf{t}_\mathrm{j}\ \right], \quad j = (1, 2, ..., m)\,. \tag{212}$$

If no additional constraints are defined, the framework still has seven open degrees of freedom: three for the position of the overall scene in space, three for the rotation, and one for the scale. The first six open degrees of freedom can easily be removed by fixing one of the views

$$\mathrm{P}_1 \stackrel{!}{=} \left[\begin{array}{c|c} \mathrm{R}_1 & \mathbf{t}_1 \end{array} \right]. \tag{213}$$

In other words, the parameters for the translation and the rotation of P_1 are excluded from the iterative estimation process, they remain fixed and thus define the position and rotation of the overall scene. In practice, the camera with the most tie point observations is chosen for this, since in this way the computational cost is reduced to the minimum. Moreover, the camera position with the highest number of observations has the highest influence to constrain the bundle. However, the set of relative translations $\mathbf{t}_\mathrm{j}$, $\forall j > 1$ still is subject to scale ambiguity. One method to fix this last open degree of freedom is to set

$$\|\mathbf{T}\|_2 \stackrel{!}{=} 1, \quad \text{with} \quad \mathbf{T} = \left[\mathbf{t}_1^\mathsf{T}, \mathbf{t}_2^\mathsf{T}, \cdots \mathbf{t}_m^\mathsf{T}\right]^\mathsf{T}. \tag{214}$$

However, all $\mathbf{t}_\mathrm{j}$, $\forall j > 1$ would change their values while optimizing the objective and consequently violate the constraint defined through (214) by each iteration step in the Levenberg-Marquardt algorithm. Here, a method from [52] allows one to adjust $\mathbf{T}$ with a given Jacobian matrix in a way that the constraint (214) remains valid after the update. This operation can be achieved by taking advantage of the properties of a **Housholder matrix**.

Consider a sphere of dimension N, which consists of the set with $(N+1)$ arrayed parameter vectors $\mathbf{a}_j$ of unit length, $\|\mathbf{A}\|_2 \stackrel{!}{=} 1$. Only the translation parameters in $\mathbf{a}_j$ will be considered. Let $\mathrm{H}_{\mathbf{v}(\mathbf{A})}$ be a Householder matrix defined as [52]

$$\mathrm{H}_{\mathbf{v}(\mathbf{A})} = \mathrm{I} - 2\frac{\mathbf{v}\mathbf{v}^\mathsf{T}}{\mathbf{v}^\mathsf{T}\mathbf{v}}, \tag{215}$$

$$\mathrm{H}_{\mathbf{v}(\mathbf{A})}\mathbf{A} = (0, 0, \ldots 0, 1)^\mathsf{T}, \tag{216}$$

where

$$\mathbf{v}(\mathbf{A}) = \mathbf{A} \pm \|\mathbf{A}\|_2 \mathbf{e}_1, \tag{217}$$

$$\mathbf{e}_1, = (1, 0, \ldots 0, 0)^\mathsf{T}. \tag{218}$$

Multiplication of $\mathrm{H}_\mathbf{v}$ with a vector $\mathbf{x}$ is most efficiently carried out through

$$\mathrm{H}_{\mathbf{v}}\mathbf{x} = \mathbf{x} - 2\frac{\mathbf{v}\left(\mathbf{v}^{\mathsf{T}}\mathbf{x}\right)}{\mathbf{v}^{\mathsf{T}}\mathbf{v}}. \tag{219}$$

Now, consider the cost function $F(\mathbf{A}, \mathbf{B})$ that originally depends on the parameter set $\mathbf{A} \in \mathbb{R}^{3m}$, which contains three translation parameters for each view $j = (1, 2, \ldots m)$ and is subject to scale ambiguity. Here, the fixed camera already has been excluded. With the transformation [52]

$$\mathbf{A} = \mathrm{H}_{\mathbf{v}(\mathbf{A})} f(\mathbf{y}), \ \mathbf{y} \in \mathbb{R}^{3m-1}, \tag{220}$$

$$f(\mathbf{y}) = \left[\operatorname{sinc}\left(\frac{\|\mathbf{y}\|}{2}\right)\mathbf{y}^{\mathsf{T}}, \cos\left(\frac{\|\mathbf{y}\|}{2}\right)\right]^{\mathsf{T}}, \tag{221}$$

the Jacobian matrix may be computed with respect to a minimal parameter set $\mathbf{y}$ via [52]

$$\mathrm{A} = \frac{\partial \hat{\mathbf{Z}}}{\partial \mathbf{y}} = \frac{\partial \hat{\mathbf{Z}}}{\partial \mathbf{A}}\frac{\partial \mathbf{A}}{\partial \mathbf{y}} = \frac{\partial \hat{\mathbf{Z}}}{\partial \mathbf{A}}\mathrm{H}_{\mathbf{v}(\mathbf{A})}\left[\begin{array}{c|c} \mathrm{I} & \mathbf{0} \end{array}\right]. \tag{222}$$

It can be seen that, for this approach, no additional Jacobian computation is necessary. The scale constraint in (214) can be achieved by multiplication with a Householder matrix. With this implementation, the parameter set is **unambiguous in scale** and hence gauge freedom can finally be removed from the framework.

However - as a logical consequence - the sparsity structure in (187) is lost for all translations, since the updates in camera positions depend on each other to maintain the overall constraint $\|\mathbf{A}\|_2 \stackrel{!}{=} 1$. Hence, depending on the number of views involved, the computational cost can grow heavily after this step.

Another possibility to remove gauge freedom in the camera translations is to **add a priori information** to the bundle adjustment framework. This method will be explained in more detail in subsection 3.2.8.

The inclusion of a priori information requires fairly accurate knowledge of the camera positions before the estimation process; however, this cannot be assumed as granted in any case. Therefore, the bundle adjustment software package developed within this work allows the user to choose, prior to the iteration, whether there shall be a **mini-**

mum parametrization as described in this subsection, or if the overall scale shall be determined by **adding a priori information**, maintaining the sparsity structure in (187).

3.2.7. Robust Student's t Approach in the Presence of Outliers

In all bundle adjustment related discussions up to this point, the assumption has been, that measurements obtained through the **FDAM** algorithm are affected by normal distributed noise only. Generally, and as introduced in subsection 2.7, any least squares optimization is only valid under this assumption. However, as discussed in subsection 3.1.6, noisy measurements - so called **outliers** - still have to be considered to be present within a small percentage of the data. In general, it is virtually impossible to ensure that automated algorithms always generate correct tie point correspondences, especially in a challenging environment like comet 67P. Here, illumination conditions are constantly changing while distinctive features are altering or even moving (Figure 47).

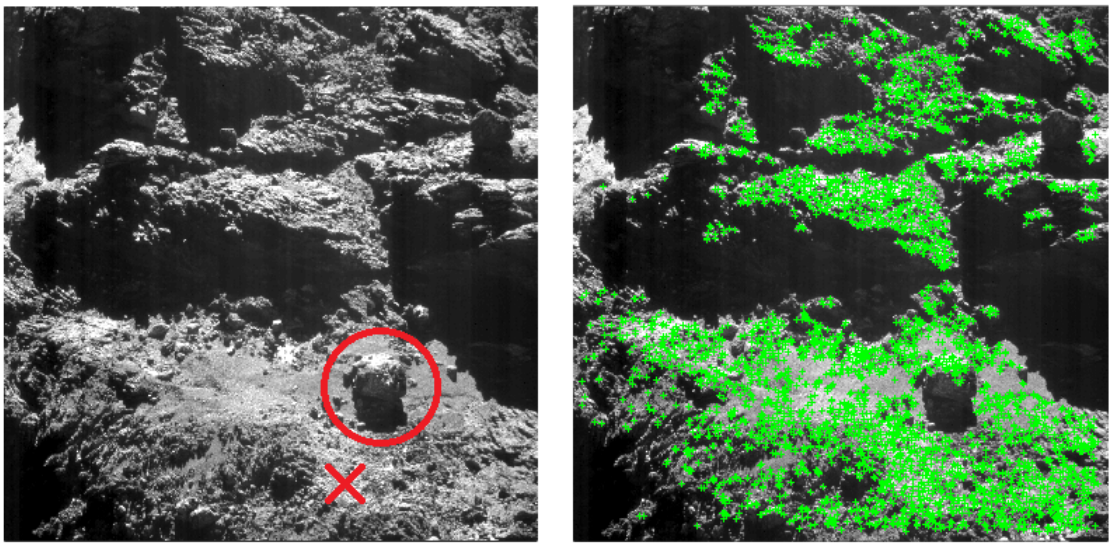

Figure 47: Key points detected within close proximity orbits in 2016. Each key point visible on the right hand side is detected and measured in at least 10 additional images from 2016. In the lower right of the image pair, the 30 meter sized boulder like feature that moved more than 100 meters on the cometary surface during perihelion can be seen. Its original position is also marked in the image. The feature was already introduced in subsection 1.3.2 (Figure 6) as a motivation for the necessity of robustness in bundle adjustment and now carries multiple tie points.

The problem with geometry estimation in the presence of outliers is that they don't follow along any a priori known statistical distribution [5].

Despite the fact that there might not be many outliers left, even a single mismatch in the least squares bundle adjustment can lead to a large phantom error that dominates other valid data and, as a result, drags single camera centers hundreds of meters away from the true position (Figure 49). Hence, close attention must be paid to the treatment of outliers to obtain a reliable solution for the camera positions.

One common approach is to make use of so called σ-edit rules. It is assumed in this method that, after one ore more iterations of the bundle adjustment, observations that exceed a predefined threshold in reprojection residuals are removed from the data [23]. Typically, measurements that exceed a range between 1 and 2 standard deviations are discarded. This approach can be problematic however, since the noisy measurements still affect the initial iteration step - which is then, in turn, used to identify outliers.

In [5], a method that shows superior stability and accuracy is introduced. With this approach, the reprojection error in pixel space is modeled as distributed along the **Student's t-distribution**. The idea behind this method is that extreme observations - such as outliers - **are much more likely** in the Student's t model than in the Gaussian model. The main reason for this is that the Student's t-distribution has much thicker tails than a Gaussian distribution (Figure 48).

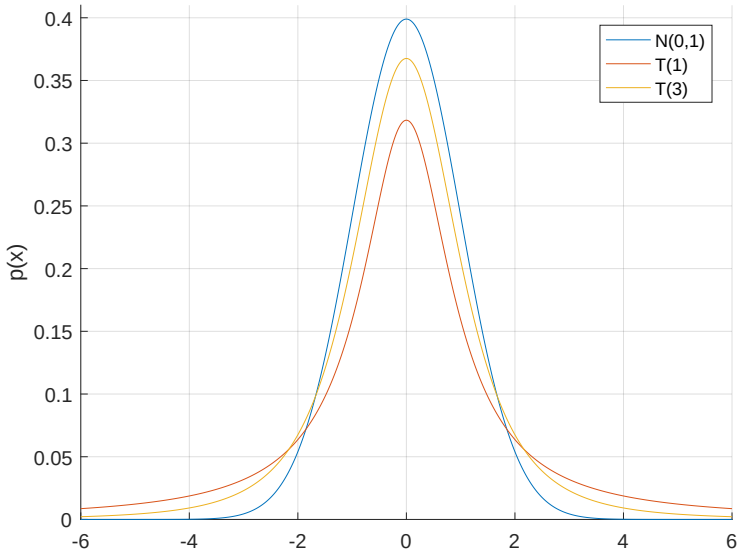

Figure 48: A comparison between the Gaussian distribution with standard deviation $\sigma = 1$ and expected value zero and the t-distribution for one and three degrees of freedom. It can be seen, that the Student's t-distribution has thicker tails than a Gaussian distribution.

Hence, large residuals will not affect the overall solution as much as in the least squares approach. In all empirical tests within this work, the method showed superior results in comparison with the least squares bundle adjustment or σ-edit rules in the presence of outliers (Figure 49).

With the mean parameter μ, the number of degrees of freedom s and the dimension m of the residual vector ϵ, the generalized Student's t-distribution is

$$\mathbf{p}\left(\epsilon|\mu\right) = \frac{\Gamma\left(\frac{s+m}{2}\right)}{\Gamma\left(\frac{s}{2}\right)\mathrm{Det}\left[\pi s\mathrm{R}\right]^{\frac{1}{2}}}\left(1+\frac{\|\epsilon-\mu\|^2_{\mathrm{R}^{-1}}}{s}\right)^{\frac{-(s+m)}{2}}. \tag{223}$$

Here, R is a positive definite matrix and $\sqrt{\mathrm{R}}$ describes a Choleski factor with $\sqrt{\mathrm{R}}\sqrt{\mathrm{R}}^{\mathsf{T}} = \mathrm{R}$. $\Gamma\left(x\right)$ denotes the Gamma function as defined in appendix A.1. In (223), the norm of a vector $\mathbf{u} \in \mathbb{R}^{\mathrm{N}}$ is defined as $\|\mathbf{u}\|_{\mathrm{M}} \coloneqq \sqrt{\mathbf{u}^{\mathsf{T}}\mathrm{M}\mathbf{u}}$, where $\mathrm{M} \in \mathbb{R}^{\mathrm{N}\times\mathrm{N}}$ denotes a positive definite matrix. Now, the minimization of the negative log likelihood

$$-\log\mathbf{p}\left(\{\epsilon_{ij}\}\right) - \log\mathbf{p}\left(\left\{\mathbf{a}_j^0 - \mathbf{a}_j\right\}\right) - \log\mathbf{p}\left(\left\{\mathbf{b}_i^0 - \mathbf{b}_i\right\}\right) \tag{224}$$

is equivalent to maximizing the likelihood of the statistical model. With all terms discarded that do not depend on $\{\mathbf{a}_j\}$ and $\{\mathbf{b}_i\}$, the derived objective is [5]

$$\begin{aligned} F(\mathbf{P}) = &\frac{1}{2}\sum_{(i,j)\in\xi}\left(s_{ij}+2\right)\log\left[1+\frac{1}{s_{ij}}\|\mathbf{z}_{ij}-\hat{\mathbf{z}}\left(\mathbf{a}_j,\mathbf{b}_i\right)\|^2_{\Sigma^{-1}_{\mathbf{z}_{ij}}}\right] \\ &+\frac{1}{2}\sum_j\left(r_j+6\right)\log\left[1+\frac{1}{r_j}\|\mathbf{a}_j^0-\mathbf{a}_j\|^2_{\Omega_j^{-1}}\right] \\ &+\frac{1}{2}\sum_i\left(q_i+3\right)\log\left[1+\frac{1}{q_i}\|\mathbf{b}_i^0-\mathbf{b}_i\|^2_{\Phi_i^{-1}}\right], \end{aligned} \tag{225}$$

with ξ being the control network of indices, which means that if $(i,j) \in \xi$, then feature i is detected in image j. The measurement $\mathbf{z}_{ij}$ is obtained from **FDAM** and $\hat{\mathbf{z}}\left(\mathbf{a}_j,\mathbf{b}_i\right)$ denotes the associated reprojection from the camera model as described in subsection 3.2.1. It follows, that

$$\mathbf{z}_{ij} = \hat{\mathbf{z}}\left(\mathbf{a}_j, \mathbf{b}_i\right) + \epsilon_{ij} \tag{226}$$

where ϵ_{ij} describes the reprojection error, but is now assumed to be distributed according to the **Student's t-distribution**. The second and the third term in (225) may be used to take ground truth or a priori orbit information into account. Here, $\mathbf{a}_j^0$ denotes known camera parameters such as position and pointing, whereas $\mathbf{b}_i^0$ contains ground control points, and the matrices Ω_j and Φ_i are the associated covariances. The values $\{s_{ij}, r_j, q_i\} \in \mathbb{N}$ are known degrees of freedom within the statistical model associated with the observations $\mathbf{z}_{ij}$, prior camera parameters $\mathbf{a}_j^0$, and ground control points $\mathbf{b}_i^0$. The constants 2, 6, and 3 in each term denote the dimensions of pixel coordinates, camera parameters, and surface points, respectively.

With the objective $F(\mathbf{P})$ now being defined through (225), the previously described Levenberg-Marquardt method is applied to converge to a solution for $\mathbf{P}$. Matrix (187) is then augmented by

$$\mathrm{H}^k = \left(\tilde{\mathrm{J}}^k\right)^{\mathsf{T}} \Sigma_{\mathbf{Z}}^{-1} \left(\tilde{\mathrm{J}}^k\right) + \mathrm{diag}\left(\left\{\varrho_j^k \Omega_j\right\}\right) + \mathrm{diag}\left(\left\{g_i^k \Phi_i\right\}\right) + \lambda^k \mathrm{I}, \tag{227}$$

and changes with each iteration step k. Remember also the partitioned Jacobian matrix from (176). Within the Student's t approach, the entries of the Jacobian are now multiplied with updated individual weights, dependent on the respective residuals after each iteration. Denote the weighted Jacobian matrices by

$$\tilde{\mathrm{J}}^k = \left[\ \tilde{\mathrm{A}}^k \ \middle|\ \tilde{\mathrm{B}}^k\ \right], \tag{228}$$

$$\tilde{A}_{ij}^k = \rho_{ij}^k A_{ij}^k, \tag{229}$$

$$\tilde{B}_{ij}^k = \rho_{ij}^k B_{ij}^k. \tag{230}$$

Finally, the weighted entries in the Jacobian matrices $\tilde{\mathrm{A}}^k$ and $\tilde{\mathrm{B}}^k$ are deduced to

$$
\begin{aligned}
\rho_{ij}^{k} &= \sqrt{\frac{s_{ij}+2}{s_{ij}+\|\mathbf{z}_{ij}-\hat{\mathbf{z}}\left(\mathbf{a}_j,\mathbf{b}_i\right)\|^2_{\Sigma^{-1}_{\mathbf{z}_{ij}}}}}, \\
\varrho_{j}^{k} &= \frac{r_j+6}{r_j+\|\mathbf{a}_j^0-\mathbf{a}_j^k\|^2_{\Omega_j^{-1}}}, \\
g_{i}^{k} &= \frac{q_i+3}{q_i+\|\mathbf{b}_i^0-\mathbf{b}_i^k\|^2_{\Phi_i^{-1}}}.
\end{aligned}
\tag{231}
$$

Note that within this work, no ground control points are used, and thus, all Φ_i related terms may simply be set to $\mathbf{0}$. Therefore, the last term in (225) vanishes.

In Figure 49, the result of a performance test is shown. For an **FDAM** derived dataset including more than 600 camera positions, the algorithm initially converged from original data. Thereafter, the relative geometry obtained was considered to fit the "true" geometry without any errors to enable the test. In other words, $\mathbf{z}_{ij} \stackrel{!}{=} \hat{\mathbf{z}}\left(\mathbf{a}_j,\mathbf{b}_i\right), \epsilon_{ij} \stackrel{!}{=} 0$ was set, meaning that the reprojections were assumed to equal the measurements exactly. In the next step, to allow for a realistic test, normally distributed noise with a σ obtained from the convergence with original data was added to these measurements. Thereafter, a percentage of outliers was added on top. The outliers were simulated as equally distributed false measurements, meaning that they could randomly carry any arbitrary pixel value covering the whole CCD of the camera. Finally, another random error of $\pm 50\,[\mathrm{m}]$ was added to the camera positions to simulate small errors in the a priori camera knowledge for the test. In this way, it was assumed that the available orbit relative to the comet is still subject to minor inaccuracies.

Now, the least squares algorithm could run in comparison with the Student's t approach in a clean but artificially noise affected environment, while the "true" geometry was known. In Figure 49, it can be seen that the Student's t method clearly outperforms least squares bundle adjustment. With 0.1% outliers being present in the data, the majority of the camera positions still resulted in an error of less than $\pm 10\,[\mathrm{m}]$, which means that a **significant improvement in the accuracy of the camera positions** could be observed. Even with 0.5% outliers, which equals one outlier per image on average, the method still converges towards the correct solution with acceptable results. Note that from empirical observations of the reprojection residuals, it can be assumed that the data obtained through **FDAM** contains less than 0.1% outliers.

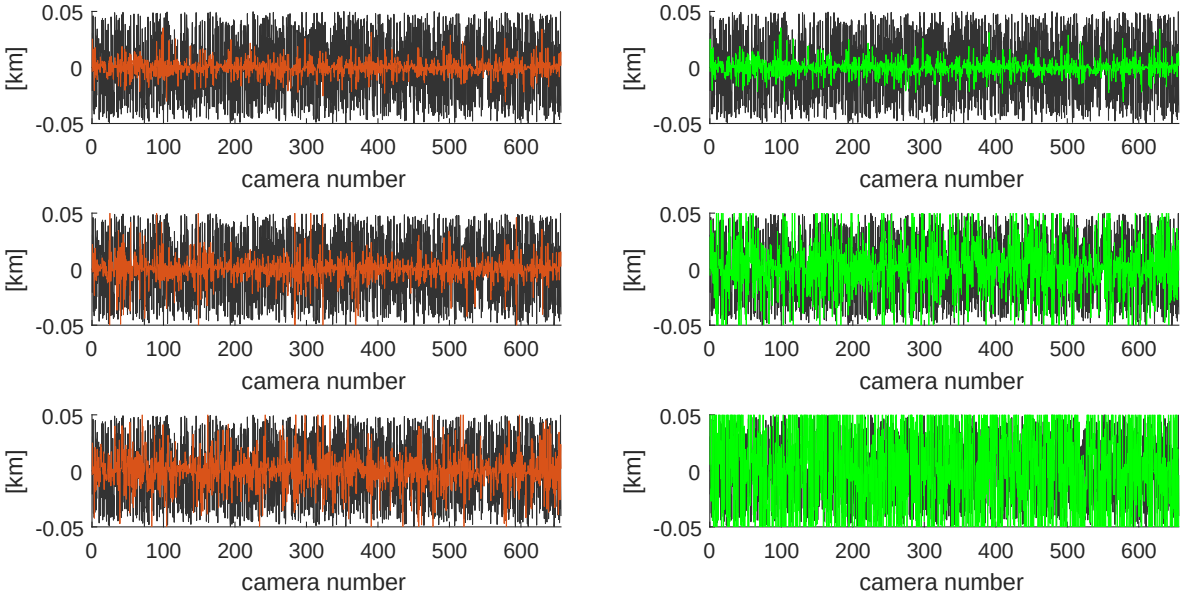

Figure 49: **Grey**: Artificially and randomly corrupted a priori camera positions with a maximum error of $\pm 50\,[\mathrm{m}]$. **Orange**: Corrected camera positions after Student's t algorithm convergence. **Green**: Corrected camera positions after least squares convergence. **Top**: No outliers lead to the same result for the Student's t and the least squares approach with comparable computational cost. **Center**: 0.1% generated outliers. **Bottom**: 0.5% generated outliers.

For least squares bundle adjustment, with 0.1% outliers present, already an acceptable solution could no longer be achieved. With 0.5% outliers present, some of the camera positions were dragged hundreds of meters or even kilometers apart. In [5][4], it was shown, that in empirical studies the Student's t approach outperformed least squares bundle adjustment even if the latter was carried out with preprocessed data, meaning that outliers were removed based on some $\sigma-$edit rule. In other words, leaving outliers within the data and starting a Student's t bundle adjustment resulted in more accurate estimation than when removing outliers and carrying out the least-squares bundle adjustment approach.

For this reason, within this work, **the Student's t approach is the method of choice.** All camera positions that will be used to support the estimation of cometary gravitational coefficients were obtained with this method. In this way, a challenging optical scenario with a continuously changing object is countered by a robust statistical approach, leading to reliable results despite the presence of some outliers. More information can be found in [52][1][106][5][4][97][20].

3.2.8. Gauge Freedom within the Student's t Approach

In subsection 3.2.6, a method was introduced which counters the problem that in reconstruction from optical data alone, the overall scale is undetermined. By fixing one camera and setting constraints so that the norm of all translations must not change between iteration steps, the scale was constrained with added computational cost, since the sparsity structure in the Levenberg-Marquardt algorithm was partially lost. However, in (225), an additional possibility arises to counter gauge freedom in the bundle adjustment process. The term

$$\ldots + \frac{1}{2}\sum_j (r_j + 6) \log\left[1 + \frac{1}{r_j}\|\mathbf{a}_j^0 - \mathbf{a}_j\|^2_{\Omega_j^{-1}}\right] + \ldots \tag{232}$$

is used to add a priori information on the camera position. Using this approach has two advantages: First, the sparsity structure in (187) can be maintained, since the Jacobian is not multiplied with a Householder matrix. Second, (232) enables for the simultaneous estimation of cometary parameters together with the pure geometric optimization of reprojection error, since $\mathbf{a}_j^0$ contains camera positions that resulted from an orbit determination. Together with the covariance Ω_j of the camera position and orientation, the full Bayesian probability framework can be maintained. In this way, a robust bundle adjustment can be combined with the estimation of the cometary rotation and gravitational field, while the sparsity of the framework is retained. Thus, this approach is **the method of choice to determine the overall scale** of the optimization problem. The method in subsection 3.2.6, however, can still be necessary, if the data of the orbit is known to be imprecise or simply not available.

3.3. Cometary Parameter Estimation

Since one goal of this work is the estimation of the gravitational field of the comet, the development of an orbit determination software was necessary. Existing RSI routines were subsequently extended whereas, in some particular applications, new routines were developed. The following subsection gives a brief overview about what was developed and how the results in section 4 were generated.

3.3.1. Time Frame

As introduced in subsection 2.2.4, the coefficients of the gravitational field have increasing influence on the spacecraft's trajectory, the closer the spacecraft gets to the cometary surface. Hence, the choice of the respective mission phase is crucial for the results. For this reason, the closest data arcs in August and September 2016 were chosen for evaluation. The close proximity of the spacecraft to the comet was driven by the search of the lander Philae, whose position on the cometary surface was still not determined up to that point in time. The lander search finally resulted in a success (Figure 50), when the lander could be detected at its final rest within an Osiris-Nac image.

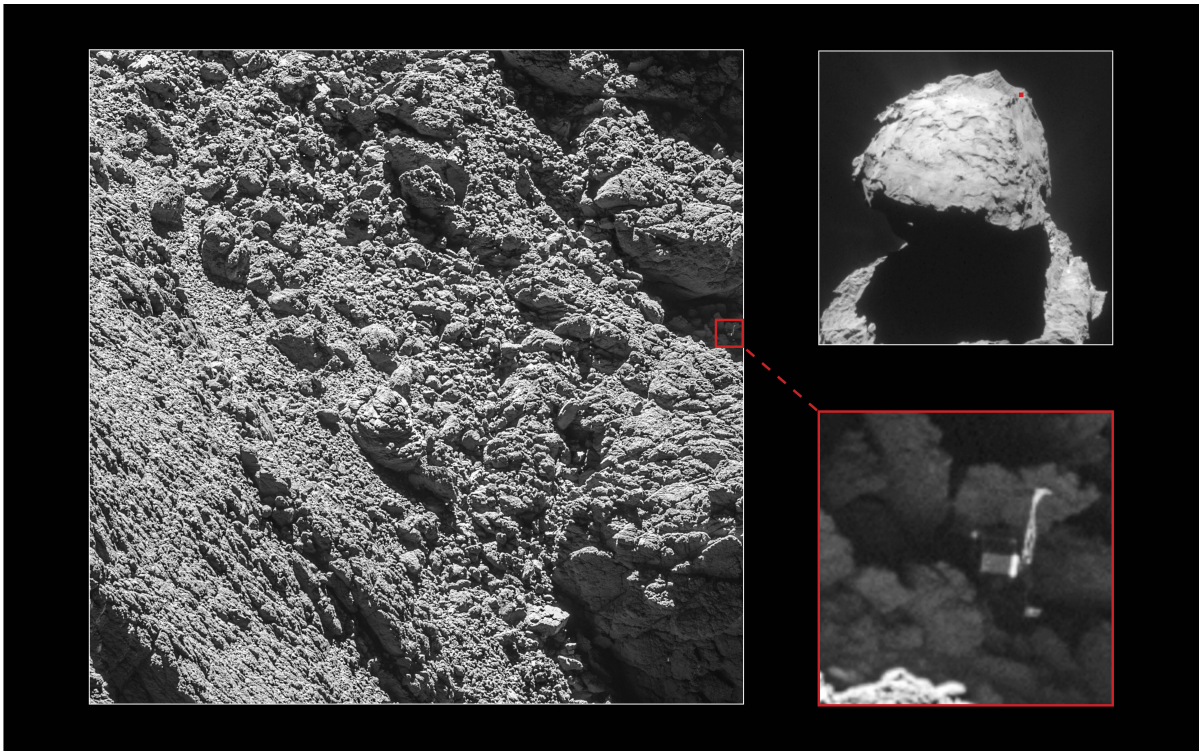

Figure 50: An Osinac image showing the landing unit Philae at its final rest. Copyright: ESA/Rosetta/MPS for Osiris Team MPS/UPD/LAM/IAA/SSO/INTA/UPM/DASP/IDA

Unfortunately, due to the lander search, the closest proximity of the spacecraft was in the same area above the cometary surface through most of the arcs. Hence, in the end, the estimated gravitational field might be biased towards the side of Philae's position. A total of 28 consecutive data arcs were processed, starting from 2016-08-15T09:00:13 UTC. For the evolution of the rotational period, longer time frames including 2014, 2015 and 2016 were evaluated. For this purpose however, orbit data from the Spice toolkit were used to compare the optical data derived position of the spacecraft in the body

fixed frame with the SPICE position in the inertial frame.

3.3.2. Gravitational Forces

The Sun, Pluto, and all eight planets, including their moons, were considered as perturbing gravitational forces acting on the spacecraft. The equation of motion was then integrated in a J2000 oriented reference frame using the solver *ode45* which is available in MATLAB. The reference frame has its origin in the center of gravity of 67P, however, it is non-rotating. Since 67P's center of gravity itself is subject to acceleration within the solar system, the comet centered reference frame must be considered non-inertial. Therefore, perturbing accelerations that act on the spacecraft were considered according to (14).

3.3.3. Orbit Control Mode (OCM) and Wheel Offloadings (WoL)

For the purpose of precise orbit determination, the time frame of the mission must be subdivided into data arcs. During the orbiting phases of the mission, the thrusters of the spacecraft were used frequently [92]. When a thruster is active, a significant perturbing force has an influence on the spacecraft trajectory. During that time, it is difficult to distinguish the acceleration caused by cometary gravity from the $\Delta\mathbf{v}$ induced by the thrusters. The usage of the twelve pairs of thrusters can be categorized in **orbit control mode** and **wheel offloading**. The first type includes orbit correction maneuvers to keep the spacecraft on the reference orbit or to set a new reference orbit. Wheel offloadings are only used to rundown the angular momentum of the reaction wheels inside the spacecraft; they are carried out more frequently, but have less fuel consumption and consequently result in a smaller $\Delta\mathbf{v}$. For this reason, **no orbit determination is carried out during OCMs; however, for gravity field estimations, during WoLs the orbit integration is continued**. In order to compensate for the resulting $\Delta\mathbf{v}$, the small differences in the spacecraft velocity are scaled within the orbit determination tool. Since the influence of the WoLs is very small, the Tikhonov-regularization as described in subsection 2.7.2 was fully implemented and led to a more stable iteration of the Levenberg-Marquardt algorithm.

3.3.4. Outgassing

The most difficult perturbing force in orbit prediction around the comet is outgassing. In general, the flow direction of the gas species is away from the cometary nucleus. The

resulting force mainly acts radial from the cometary nucleus, which is similar to the parameter GM, however, in opposite direction. Hence, the perturbing force is directly correlated with the GM value in (23), which is part of the estimated parameters as well. If the outgassing perturbing force is estimated too low, as a consequence, the cometary mass will also be underestimated.

An instrument on Rosetta that successfully obtained outgassing related measurements at the comet is the Rosetta Orbiter Spectrometer for Ion and Neutral Analysis (ROSINA). Its main objective is to determine the major atmospheric and ionospheric compositions in the coma and to investigate the gas dynamics around the comet [109]. It has two mass spectrometers, the Reflectron-type Time-Of-Flight mass spectrometer (RTOF), and the Double Focusing Mass Spectrometer (DFMS), which are capable of measuring ions and neutrals. Additionally, it contains the COmet Pressure Sensor (COPS), which has two pressure/density gauges: the nude gauge and the ram gauge. The nude gauge has an almost spherical field of view and measures the total neutral pressure of the coma, whereas the ram gauge measures the ram pressure. If the ram gauge is pointing opposite to the direction of the outgassing flow, information about the gas velocity can be revealed from the ratio between the ram gauge and the nude gauge pressure measurement. More information about ROSINA can be found in [109][2].

Figure 51 shows ROSINA measurements acquired during the 28 data arcs of interest, starting in 2016-08-15T09:00:13 UTC. The upper subplot shows the spacecraft distance with respect to the cometary nucleus, including each start point of the 28 arcs together with all wheel offloadings that have an influence on the optical measurements processed within this work. In the bottom plot, ROSINA derived data can be seen. Apparently, the particle density around the spacecraft increases by more than a factor of 10 when the spacecraft is close to the nucleus. Additionally, it becomes clear that the gas velocity is not constant and decreases in close proximity. The sublimated gas from the cometary surface accelerates in radial adiabatic expansion [13]. In this way, it converges towards a relative velocity, equally above all points on the nucleus surface, called the terminal velocity. This convergence process is known to happen very quickly, with the gas reaching the terminal velocity after a few nucleus radii. It is assumed that the terminal velocity varies around 600m/s at 3.5AU up to 800m/s close to perihelion in [13], larger ranges from 400m/s up to more than 1000m/s are described in [109]. It is commonly assumed that Rosetta operates in a range relative to the nucleus, where the terminal velocity is already reached. Figure 51, however, illustrates that for the very close orbits towards the end of the mission, this assumption is not valid. Note that the ratio of ram gauge to nude gauge pressure - which is proportional to the average gas flow velocity around the spacecraft - is not available through all times of interest.

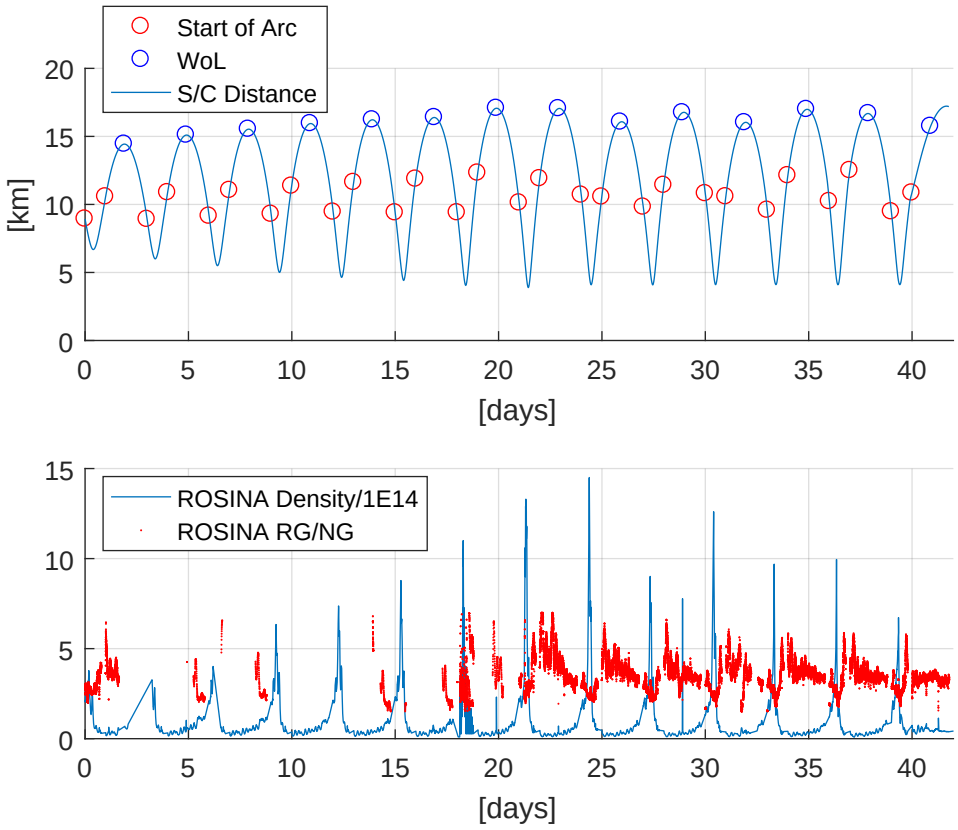

Figure 51: **Top**: The spacecraft distance during the close orbits beginning at 2016-08-15T09:00:13 UTC including the start of the data arcs and wheel offloadings. **Bottom**: Derived COPS density and the ratio of the ROSINA Ram Gauge to Nude Gauge.

Another interesting finding is that ROSINA is able to measure the consumed fuel particles of the individual spacecraft thrusters around the spacecraft. Around days 20 and 28, sudden density peaks can be seen in the lower plot of Figure 51. Note that the peaks appear at times when WoLs were executed, which is visible in the upper plot.

In this case, however, the measured gas velocity is influenced from both the cometary outgassing and the thruster particles. Since at times not only cometary atmosphere particles are measured, and additionally, velocity measurements are not available over the entire time frame, **both the gas velocity and density measurements need to be smoothed and extrapolated**.

In order to account for this within the implementation of the drag force model, the particle density and gas velocity data points are fitted to a spherical harmonics expansion. In this way, the measurements visible in Figure 51 are smoothed and extrapolated. The result can be seen in Figure 52. Note that the extrapolated gas velocity is available

over the entire time frame, and the peaks in particle density vanished.

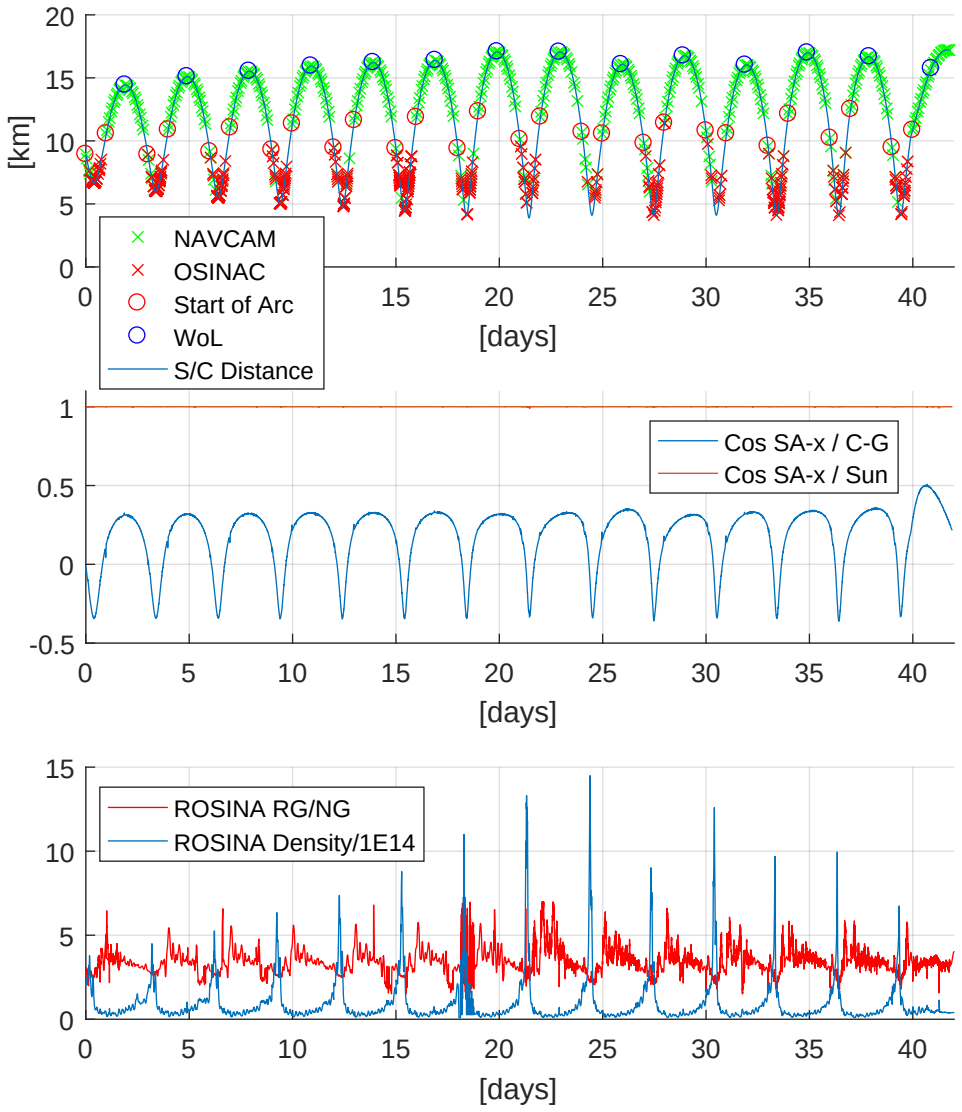

Figure 52: **Top**: NAVCAM images (green) and OSINAC images (red) which were taken beginning at 2016-08-15T09:00:13 UTC. **Center**: Cosine between the spacecraft solar array normal and the vector from the comet center of mass towards the spacecraft / the vector towards the Sun. **Bottom**: Extrapolated and smoothed ROSINA data.

Figure 52 also shows the cosine between the spacecraft solar array normal and the vector from the comet center of mass towards the spacecraft. Any time this value is not equal to zero, the solar arrays expose an increased area towards the outgassing flow. The same principle applies to the high gain antenna, however, with a much smaller area being exposed. Especially when the spacecraft is in close proximity, these values do not

equal zero, leading to additional drag force.

In order to model the drag force correctly, the gas velocity is assumed to be around 550m/s with variations proportional to the changes in the RG/NG ratio. This base velocity reference is taken from [109], who analyzed the outgassing velocity from measurements in October 2014. In this way, only the drag coefficient C_D in (45) must be scaled over all 28 arcs, with the affected area A being proportional to the exposed area of the solar arrays, the spacecraft bus, and the high gain antenna. Hence, the need for additional parameters that must be estimated can be minimized. The velocity vector of the outgassing flow is always assumed along the axis between the comet center of mass and the spacecraft, which is certainly not correct when the spacecraft is close to one of the two lobes [22]. Additionally, outbursts are not modeled within the spherical harmonics smoothing. The implementation within this work reflects the best knowledge available from the ROSINA measurements, however, **a more advanced model of the flow direction in the cometary atmosphere including outbursts probably could further enhance the precise orbit determination results** in future research. More information about ROSINA and COPS can be found in [2][104].

3.3.5. Solar Radiation Pressure

The solar radiation pressure is scaled as one single parameter over the entire time frame. In Figure 52, it can be seen that the cosine between the spacecraft solar array normal and the Sun is constant. The panels are continuously pointing straight towards the Sun. As a result, the majority of terms in (43) vanishes, and solar drag can be assumed as almost constant. Attempts at scaling one solar radiation pressure parameter per arc led to 28 almost equal values, strengthening the assumption that one parameter is sufficient.

3.3.6. Rotational Parameters

Over the entire mission, comet Churyumov-Gerasimenko was continuously changing its rotational parameters due to outgassing processes. Within a time frame of 40 days, it is no longer valid to assume that the rotational period is constant; this will be shown more in depth in section 4. Hence, for the precise orbit determination purpose, four parameters are scaled to describe a third order polynomial interpolating the changes in the comet's angular velocity. Prior to this step, Euler's rotation equations (235) were numerically solved to confirm that a third order polynomial is sufficient for the designated time frame and no non-principal axis rotation must be considered for this period. In this way, computational cost could be reduced significantly. However, within the or-

bit determination tool, the rotational state of the target body may also be determined by a full integration of (235), if necessary.

3.3.7. Initial State

The initial state vector is taken from the SPICE toolkit as a start value and then adjusted iteratively through six parameters per data arc.

This concludes section 3 – the description of the numerical implementations within this work. All derived results will be explained in the following chapter.

4. Results

In this section, all results that were derived within this work will be explained and discussed.

4.1. Feature Detection and Matching

As described in section 1, at comet 67P, higher order terms of the cometary gravitational potential have a statistically significant influence only with a target center distance less than about 30km. Since prolonged mission phases and hence many images were taken outside of this criterion, the processing of optical data acquired outside 35km target center distance was omitted. Images between 30km and 35km were still considered in order to keep consecutive image series from orbits that just transitioned inside 30 km from a greater distance. The closer the comet moved towards the Sun, the more intense the outgassing activity was. This scenario led to the spacecraft orbiting at a larger, safe distance from the comet, well outside 35km target center distance. As a consequence, almost no images from 2015 were processed, except for a few in January and February. Since the cometary surface was undergoing significant changes during perihelion (Figures 3, 4, and 6), no feature matching was carried out between images taken prior and post perihelion.

	Navcam		Osiris-Nac	
	2014/15	2016	2014/15	2016
measurements #	7469531	9921474	3882613	15606864
surface points	283897	430606	257450	960546
images	2769	3380	1722	3104
start time	14-09-09T02:04	16-02-19T04:20	14-09-09T03:20	16-02-24T07:06
stop time	15-02-14T20:00	16-09-30T00:59	15-02-14T20:04	16-09-30T08:51
mean # / point	26.3	23.0	15.1	16.3
mean # / image	2697.5	2935.3	2254.7	5027.9
mean $3\sigma - x$	0.50px	0.49px	0.37px	0.51px
mean $3\sigma - y$	0.39px	0.37px	0.28px	0.42px
mean convergence	35%	33%	36%	42%

Table 3: Summary of all processed imagery datasets. A total of 10975 camera positions for orbit determination could be determined from this data.

Additionally, no cross feature matching was carried out between Osiris-Nac and

NAVCAM images because of significant differences in scale and systematic directional calibration offsets within the different filters of the OSIRIS-NAC. As a result, **a total of four datasets** of imagery data have been processed in this work. Table 3 summarizes the used data. It can be seen that each surface point is observed in multiple images, on average between 15 and 26 observations, but up to more than 100 observations in some cases. Additionally, tie point measurements on average are below 0.5 pixels within the 3σ a priori uncertainty estimate. The objective function in polynomial least squares matching decreases by more than 50 percent on average, indicating good convergence of the method within the SIFT detected key points. On average, more than 2000 measurements can be obtained per image. Within the processed data, on average, 61 minutes passed between two consecutive images of the NAVCAM while the minimum duration in between was 177 seconds. Regarding the OSIRIS-NAC, on average, 67 minutes passed between two images while the minimum duration could only be 6 seconds. Overall, 1.93×10^6 surface points are observed in 36.88×10^6 subpixel accurate measurements from 10975 images, obtained through the fully automated algorithm **FDAM** in widely altering scales, reaching from 4km up to the 35km target center distance.

4.2. Robust Bundle Adjustment

After the processing of all imagery data, robust sparse bundle adjustment was carried out with all four datasets. Due to the high number of parameters involved through millions of surface points and thousands of images, it becomes necessary to take advantage of the problem's sparsity structure as described in subsection 3.2.1. After the bundle adjustment eventually converged, the objective function and reprojection error together with the required changes in the camera positions and the derived surface point cloud could be evaluated. Figure 53 illustrates the total correction distance required per camera position in order to achieve convergence for the bundle of rays.

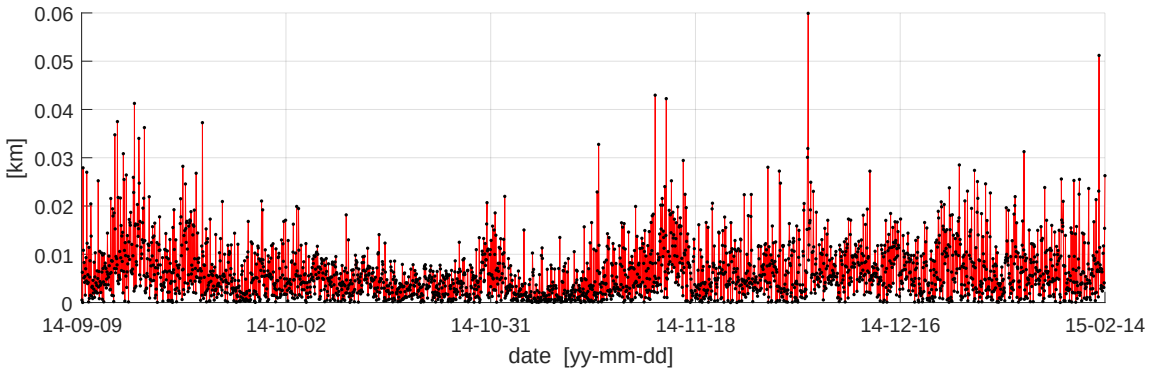

Figure 53: Correction of camera positions for the NAVCAM 2014/15 dataset.

The convergence ratio of the reprojection error from equation (225) is **18.7%** for the NAVCAM 2014/15 and **11.5%** for the NAVCAM 2016 dataset, respectively, indicating a good convergence and improvement from the start values obtained via the SPICE toolkit in conjunction with triangulation of the surface points.

Figure 54 shows a comparable result. Maximum corrections are in the order of 60m, and, on average not more than 15m correction is needed for convergence. This result is clear evidence that the SPICE orbit already has a high level of precision.

Interestingly, at some mission phases, larger corrections seem to be necessary in order to fit the data. Possible reasons for this are outbursts, differences in relative distance, or challenging conditions for optical navigation, such as altering phase angles or general non-optimal illumination conditions. However, note that the observed changes cannot be assigned to a specific orbit in each case, because for the purpose of parametrization, one camera position remains fixed in the process of bundle adjustment; camera positions close to the fixed one can result in smaller corrections.

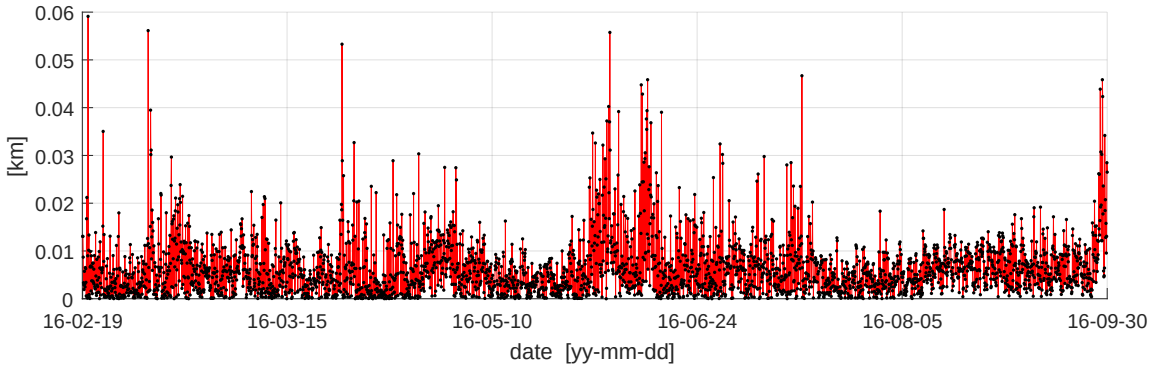

Figure 54: Correction of camera positions for the NAVCAM 2016 dataset.

Figures 55, 56 and 57 show the combined surface points of all datasets mentioned in Table 3. The point cloud markedly reflects the bilobate shape of the comet (Figure 58). All keypoints visible were detected, triangulated, and corrected through **FDAM** and **RSTBA**. It can be seen that the **SIFT** algorithm favors areas that create gradients in the imagery data, as introduced in subsection 3.1. Hence, for example, Figure 55 shows less detections in the neck region of the comet. In general, the changing illumination conditions between 2014 and 2016 caused the feature detection algorithm to favor different areas of the cometary surface. The images in 2016 allowed for more key point detections, because the spacecraft operated in comet proximity over a longer timeframe and, on average, in closer orbits. This led to a higher level of detail and more distinctive features within in the imagery data.

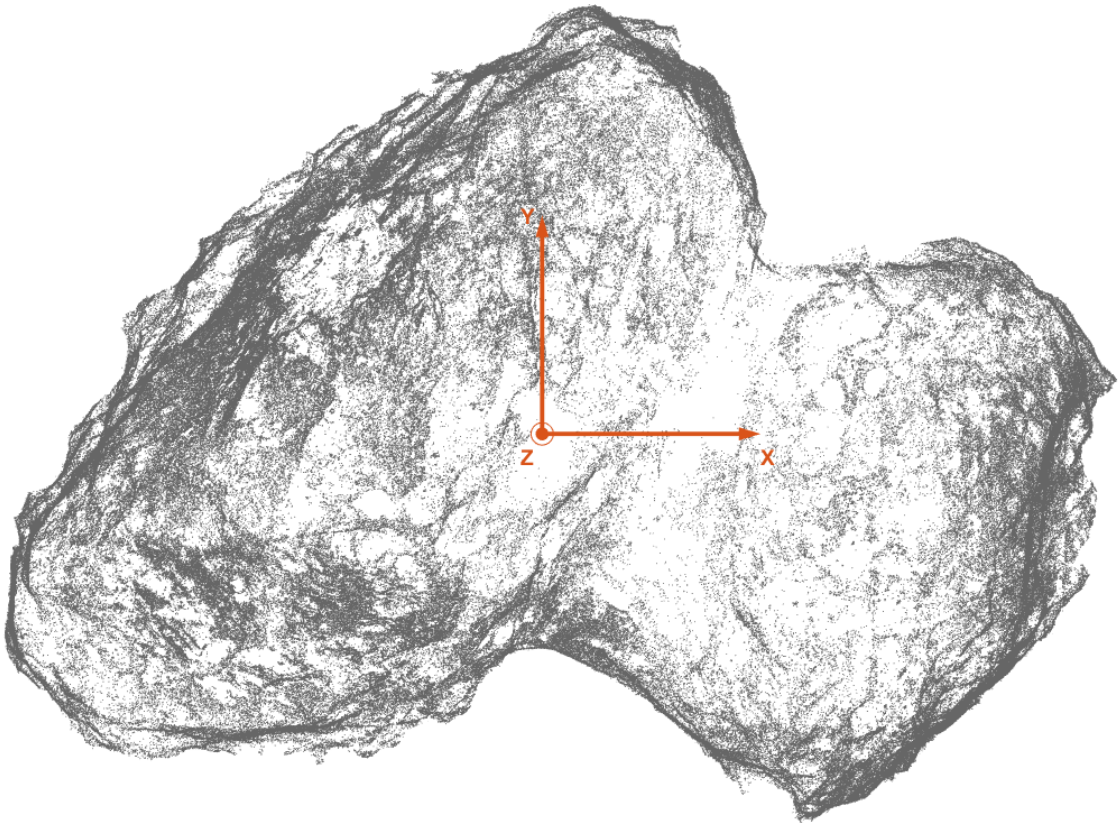

Figure 55: Corrected distinctive surface points combined for all datasets. Each point is visible and measured subpixel-accurate in at least 10 additional images. The +Z axis points out of the image plane.

The accuracy of the method introduced within this work can be evaluated by analyzing the remaining **reprojection error after convergence**. For both the NAVCAM 2014/15 and 2016 dataset, the root mean square reprojection error is **0.6 pixels**, confirming that subpixel accuracy could be achieved. In [23], the RMS accuracy of a state of the art algorithm for the Rosetta mission is given to be **0.7 pixels**, indicating that the **SIFT** tie point detection in conjunction with **polynomial least squares matching** and the **Student's t robust bundle adjustment** leads to an improvement in accuracy. Additionally, a considerably larger database of tie points was used to generate the results within this work. The uncertainties for the camera position on average are in the range of 7 meters for all images processed. For the very close orbits in 2016, the average uncertainty of the camera positions is 3.7 meters.

For the OSIRIS-NAC datasets, the same procedure was applied. Figures 59 and 60 show the required changes in camera position in order to achieve convergence of the reprojection error.

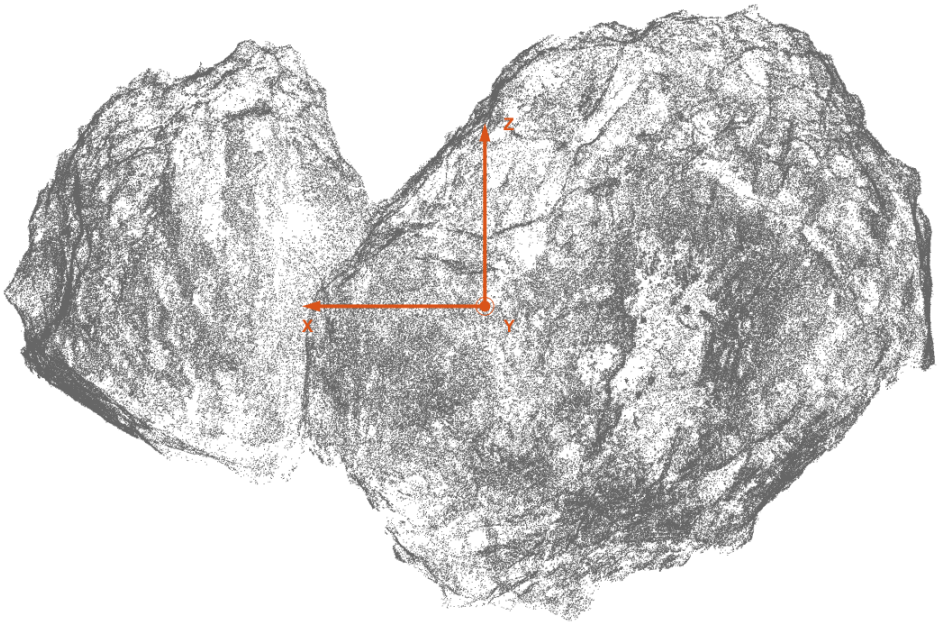

Figure 56: Corrected distinctive surface points. All points were automatically detected by **FDAM**, triangulated, and precisely located in bundle adjustment. The +Y axis points out of the image plane.

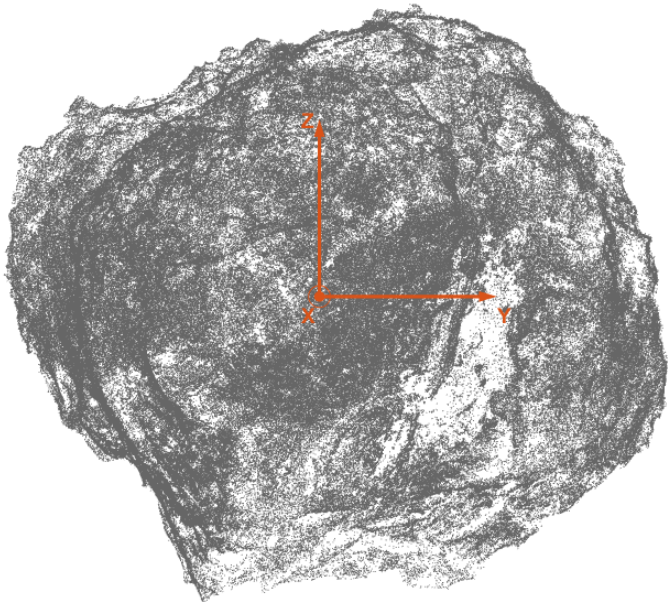

Figure 57: Corrected distinctive surface points from Figures 55 and 56. The +X axis points out of the image plane.

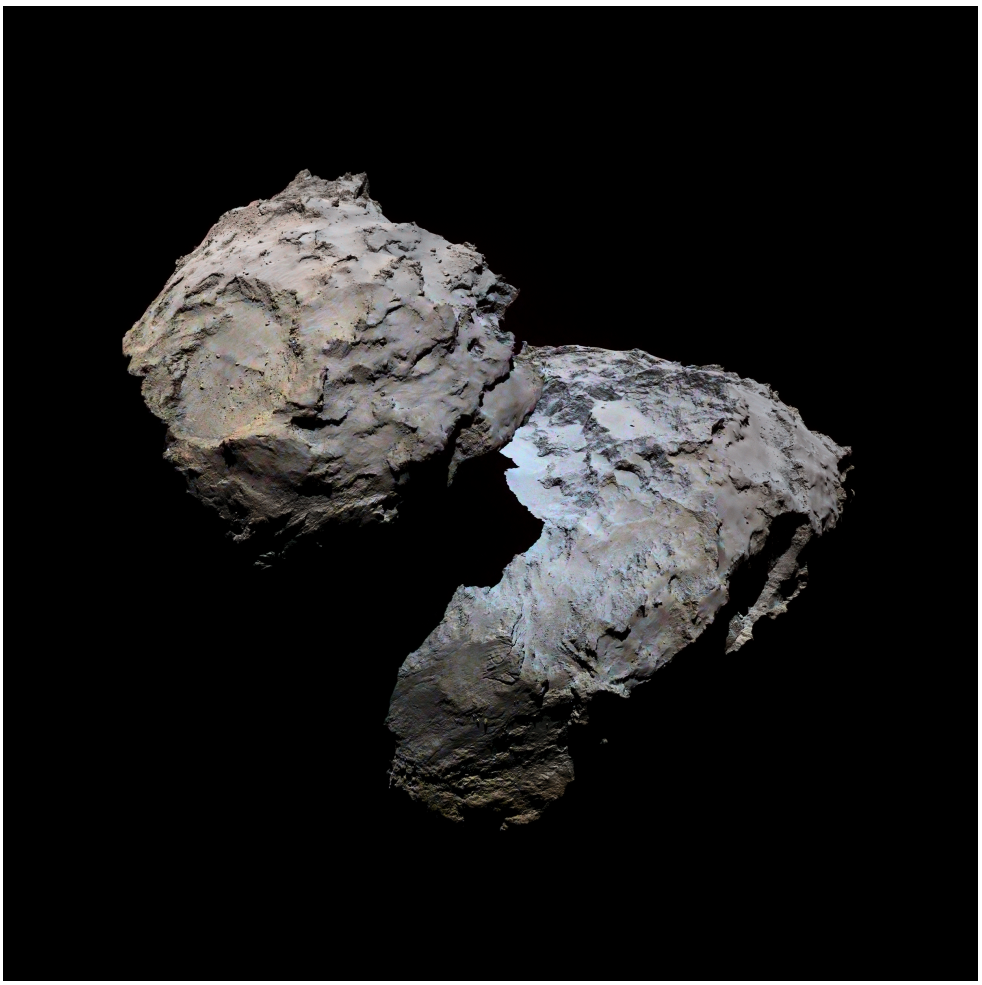

Figure 58: A comparison to the corrected surface points in Figures 55, 56, and 57: The image of comet Churyumov-Gerasimenko taken on 5 August 2014 from a distance of 123km. The view is reconstructed from three images through orange, blue and near-IR filters. Spectra beyond human vision are made visible. Copyright: ESA/Rosetta/MPS for Osiris Team MPS/UPD/LAM/IAA/SSO/INTA/UPM/DASP/IDA/Daniel Macháček

It is observable, that the scientific Osiris camera system was not primarily used for navigational purposes. Frequently, a series of consecutive images was taken with different filters in a fairly short amount of time. This led to the spacecraft not traveling far during that period, so images are often corrected towards positions close by. This effect can clearly be seen in Figures 59 and 60 when comparing to the camera corrections shown in Figures 53 and 54.

In order to find tie points within the Osiris imagery data, no additional tie point search was applied for reasons of computational cost. Instead, the tie points found within

the NAVCAM datasets were used as start values and searched for within the OSIRIS images. This is the reason why much stronger convergence ratios of **2.3%** and **2.7%** could be observed in bundle adjustment. The root mean square of the reprojection error remained at **1.21 pixels** after convergence. However, the a priori estimate of the match uncertainties is well below one pixel (Table 3). This can be explained by the following reasons. First, in the case of the OSIRIS images, directionally calibrated products were used. In these files, the directions are corrected for nonlinear distortions and new pixel values are generated through a two-dimensional linear interpolation. Since the real pixel brightness cannot be assumed to change linearly with the direction, a small error occurs with this approach.

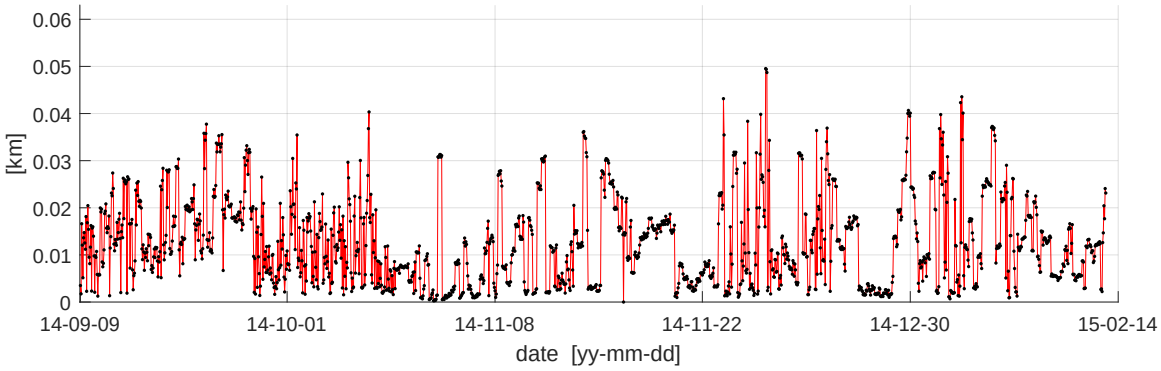

Figure 59: Correction of camera positions for the OSIRIS-NAC 2014/15 dataset.

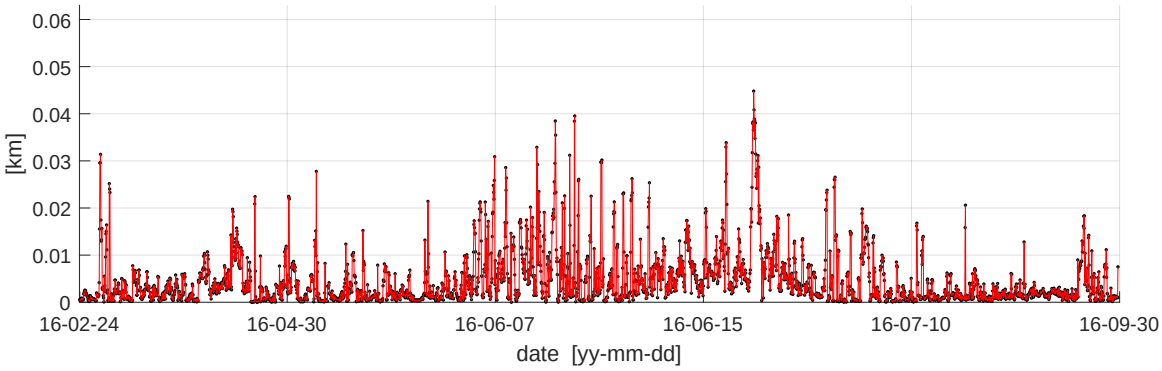

Figure 60: Correction of camera positions for the OSIRIS-NAC 2016 dataset.

Additionally, in [68], a camera distortion and boresight correction update was given. It states that, depending on temperature and filter, offsets in the pixel direction up to 10 pixels have been observed. The given correction values for the filter-caused directional changes were considered within this work; however, changes through variations in

temperature were not modeled. Summarized, with **1.21 pixels** RMS after convergence, a directional error remains. However, due to the small field of view and the higher resolution of 2048 pixels, **the directional accuracy is still higher** than for the NAVCAM data.

4.3. Cometary Parameters

4.3.1. Evolution of the Rotational Period

The outgassing induced evolution of the rotational period of the comet was widely discussed in many publications [62][87][71][76][100]. From the optical data processed within this work, the rotational period of the comet is determined precisely. Since the reconstruction from optical data results in camera positions in a body fixed frame, the results can be compared to the orbit in the J2000, and the rotational parameters can be derived. Figures 61 and 63 show the changes during the time frame when spacecraft positions were obtained from bundle adjustment. The evolution of the rotational period $P(t)$ is fitted by a polynomial of degree three, written as

$$P(t) = \sum_{n=0}^{3} c_n t^n, \tag{233}$$

where $t = (et_{\text{image}} - et_0)/10^8$ describes the time interval in Ephemeris Time seconds after the first processed camera image, but scaled by a factor of 1E-8 for numerical stability. The resulting polynomial coefficients c_n for the 2014/15 and 2016 datasets can be found in Table 4. The first images for the respective datasets were taken at UTC 2014-09-09T02:04:34, and UTC 2016-02-19T04:20:27. The two polynomials describe the rotational period until 14 February 2015 and 30 September 2016, respectively.

n	c_n 2014/15	c_n 2016
0	12.4040 ± 0.0001	12.0607 ± 0.0001
1	0.0097 ± 0.0003	-0.0429 ± 0.0003
2	-0.0992 ± 0.0037	0.1796 ± 0.0020
3	0.9799 ± 0.0125	-0.3298 ± 0.0048

Table 4: Polynomial coefficients for the description of the rotational period of comet 67P within the time frame of camera observations processed within this work.

Interestingly, in 2014/15, the rotational motion of the comet initially slowed down instead of showing an acceleration. However, after the time frame plotted in Figure 61, the comet soon underwent a significant angular acceleration. With the largest moment of inertia $I_z = 1.89 \times 10^{19}$ kg m^2 as stated in [62], a decelerating torque between -1.38×10^4 kg m^2 s^{-2} at 3.3 AU and -8.12×10^4 kg m^2 s^{-2} at 2.3 AU on 14 February 2015 can be observed with the 2014/15 dataset.

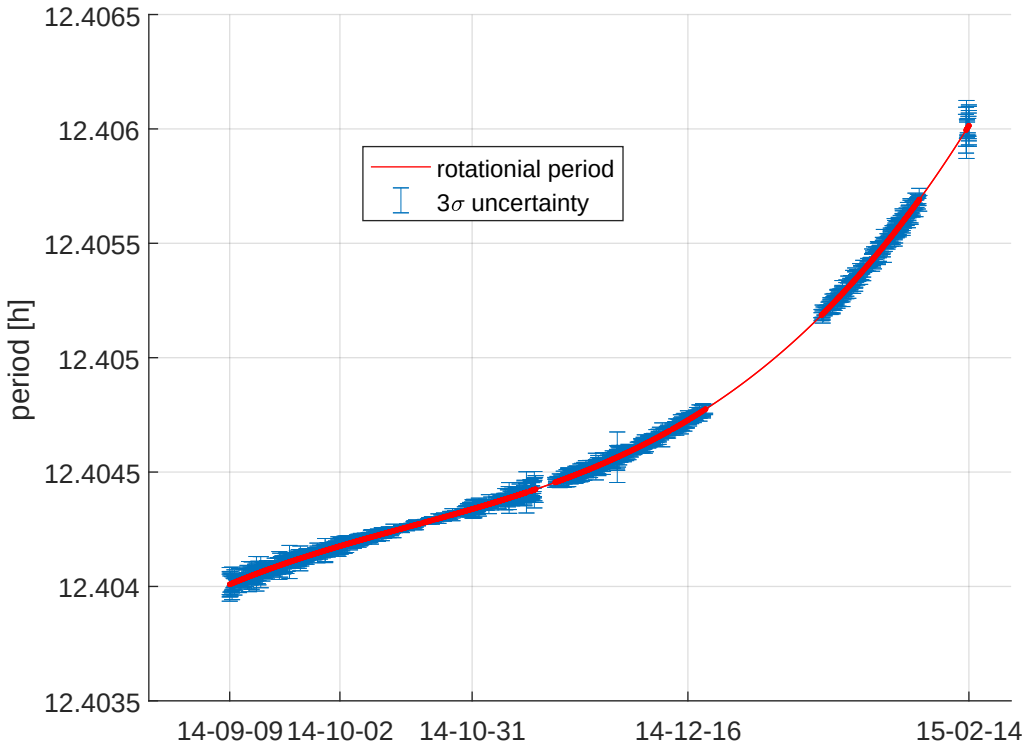

Figure 61: Evolution of the rotational period in 2014/15, beginning at 2014-09-09T02:04:34 UTC. During the time frame, when the spacecraft was orbiting in close proximity to the comet, an increase in the period can be observed.

In [65], it was shown why the period initially increases during the approach of the comet towards the Sun; it has its maximum shortly before the equinox and then drops rapidly during perihelion passage. The measured deceleration mainly depends on the shape of the nucleus, leading to varying areas with the highest torque efficiency on the cometary surface, as the comet continues to close towards the Sun (Figure 62). By using a detailed shape model of the comet, the authors of [65] have shown how the orientation and the distance from the center of mass for each model facet affects the overall torque distribution that acts on the comet. The result and analysis in their study is in good agreement with the results that could be derived within this work.

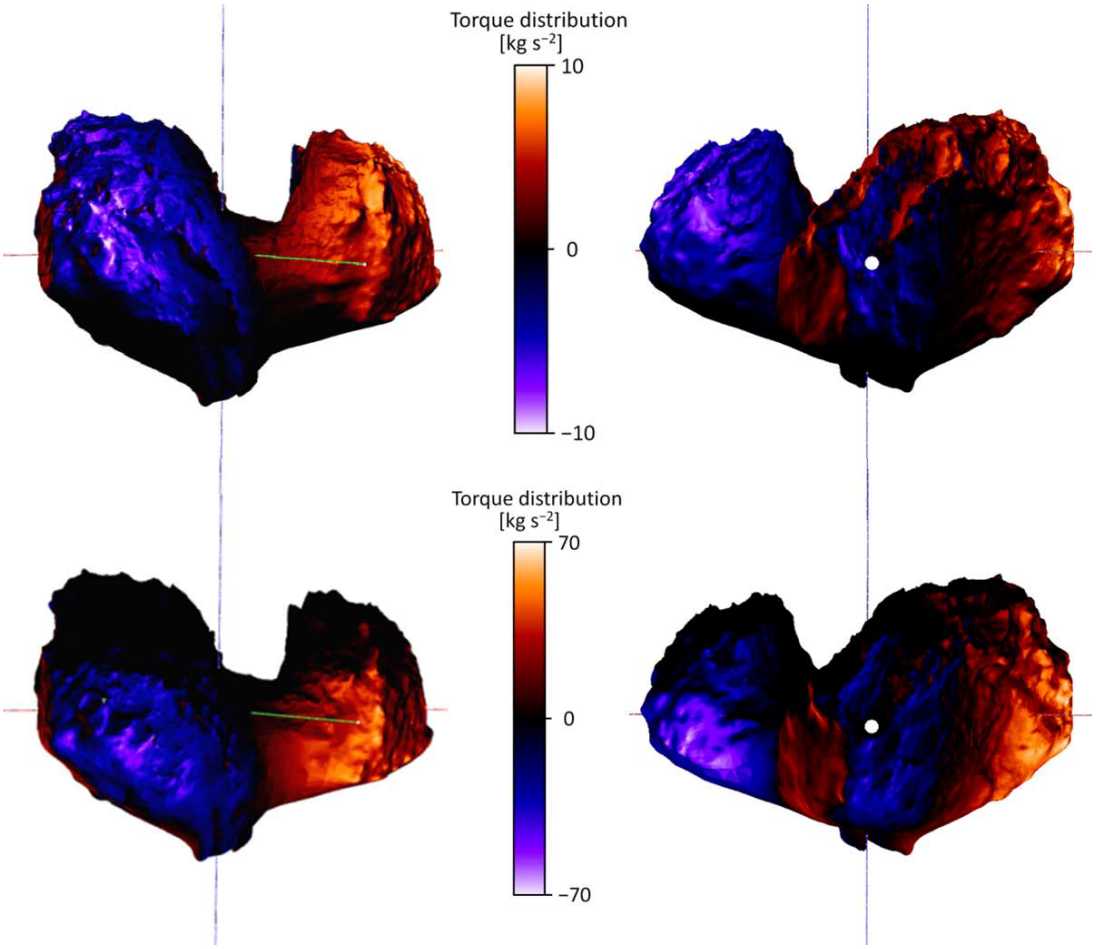

Figure 62: An illustration taken from the study accomplished in [65]. Blue areas decelerate, red areas accelerate the angular velocity of the comet. Top: Torque distribution on 20 January 2015, in this timeframe, the changes in the rotational period of the comet could be observed within this work. Bottom: Torque distribution at perihelion, significant changes can be seen; the dimension is torque per area [65].

Periods between 12.4060 ± 0.0001h in 2015 and 12.0567 ± 0.0001h in 2016 could be observed from the data processed within this work. With the 2016 dataset, an accelerating torque between 9.74×10^4 kg m^2 s^{-2} at 2.4 AU and 2.34×10^4 kg m^2 s^{-2} at 3.8 AU on 30 September 2016 can be observed. Note that even after more than one year after perihelion, a significant angular acceleration in the rotational period of the comet is still measurable (Figure 63).

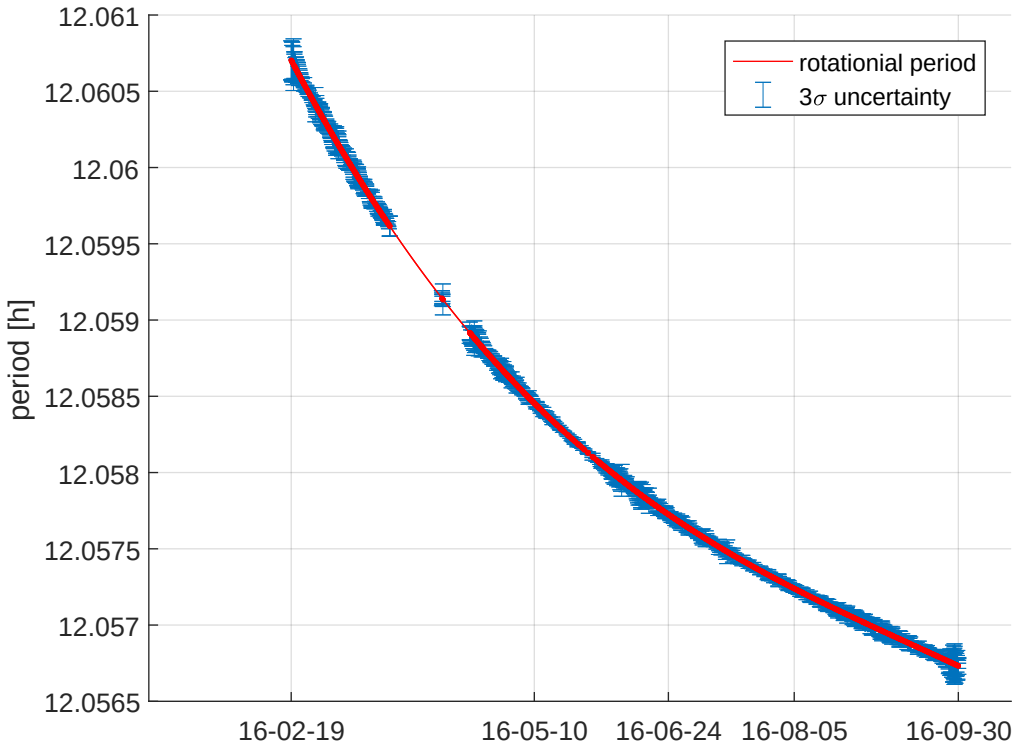

Figure 63: The changes of the rotational period measured in 2016, beginning at 2016-02-19T04:20:27 UTC.

4.3.2. Non-Principal Axis Rotation

As the spacecraft came closer to the comet, no signs of multiple periodicity could be found from approach observations with the Osiris cameras on Rosetta [87]. Shortly after the arrival of Rosetta at the comet, however, a non-principal axis rotation mode was presumed after first data analysis [100]. For navigational purpose, the authors of [43] had hoped and explicitly searched for a small torque-free nutation motion, since it would have helped to accurately determine the inertia matrix and center of mass. However, they came to the conclusion that any free nutation motion had to be within the noise. The same has applied for this work. Repeated attempts to find a non-principal axis rotational period within the data were not successful. However, a cone size of 0.14 degrees, as stated in [99], has been precluded, since it would have caused residuals of more than 50 meters in the camera positions (Figure 66).

Since the final orbit reconstruction has a residual RMS of 4.13 meters, this magnitude of non-principal axis rotation would be visible in the data. Additionally, the stated period of 10.7 days requires moments of inertia that differ significantly from those of a homogeneous density distribution [49]. However, up to degree and order four of gravitational coefficients, the comet appears to have a predominantly homogeneous structure and density distribution inside the nucleus, as it will be shown in subsection 4.3.3.

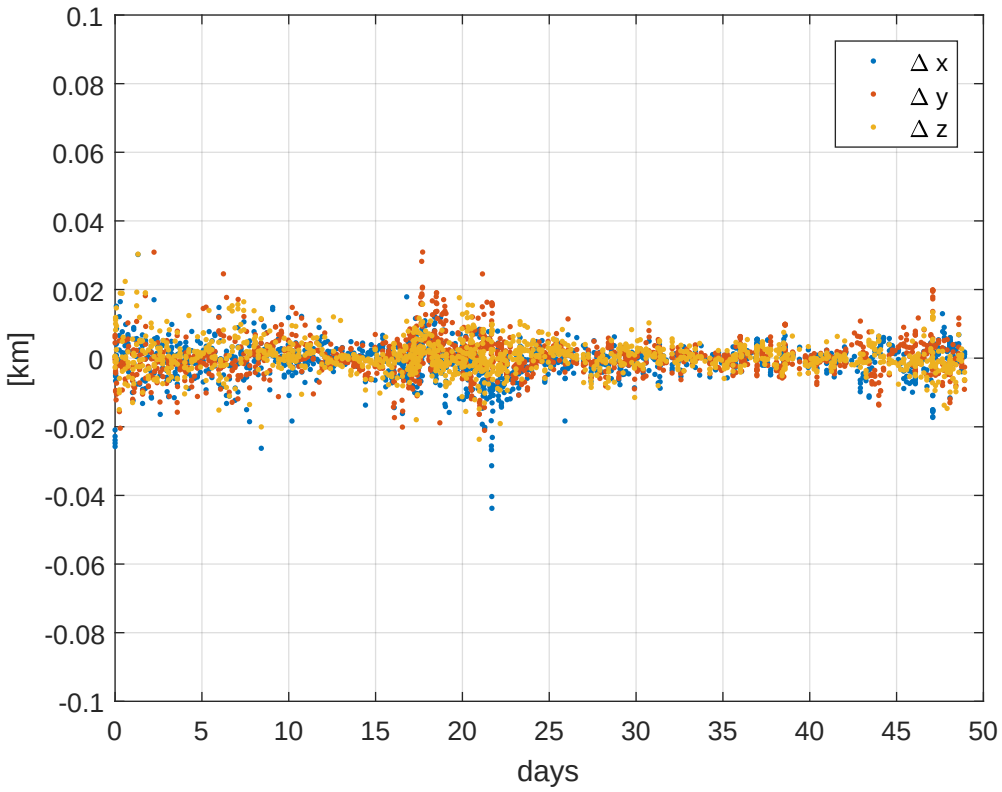

Figure 64: Residuals of OSINAC and NAVCAM camera positions after iterative integration of the euler equations over 50 days in 2014, beginning at 2014-09-09T02:04:34 UTC.

When searching for a non-principal axis rotation, the rotational period is usually averaged over a specific period, and the orientation of the spin axis is estimated. However, Figure 67 shows a significant problem within this approach. If the rotational period of the comet is held constant within a model, whereas the comet actually changes its angular velocity, additional periods appear in the residuals. After only 10 days, the first amplitudes can be seen. If the orbital plane of the spacecraft around the comet is not perpendicular to the spin axis, this can easily be confused with a periodically changing rotation axis of the target body. The reason for this effect is the constantly changing rotational period of the comet.

In order to overcome the problem, the euler equations (235) as defined in the appendix A.2 were fully integrated to derive the changes in the rotational period and search for any non-principal axis rotation mode. For the simulation, the moments of inertia $I_x = 0.95 \times 10^{19}$ kg m^2, $I_y = 1.76 \times 10^{19}$ kg m^2, $I_z = 1.89 \times 10^{19}$ kg m^2 as stated in [62] were used. The result can be seen in Figures 64 and 65, which show the residuals in the position of the spacecraft for the 2014/15 and the 2016 datasets relative to the comet without any non-principal axis rotation being necessary. The root mean square error

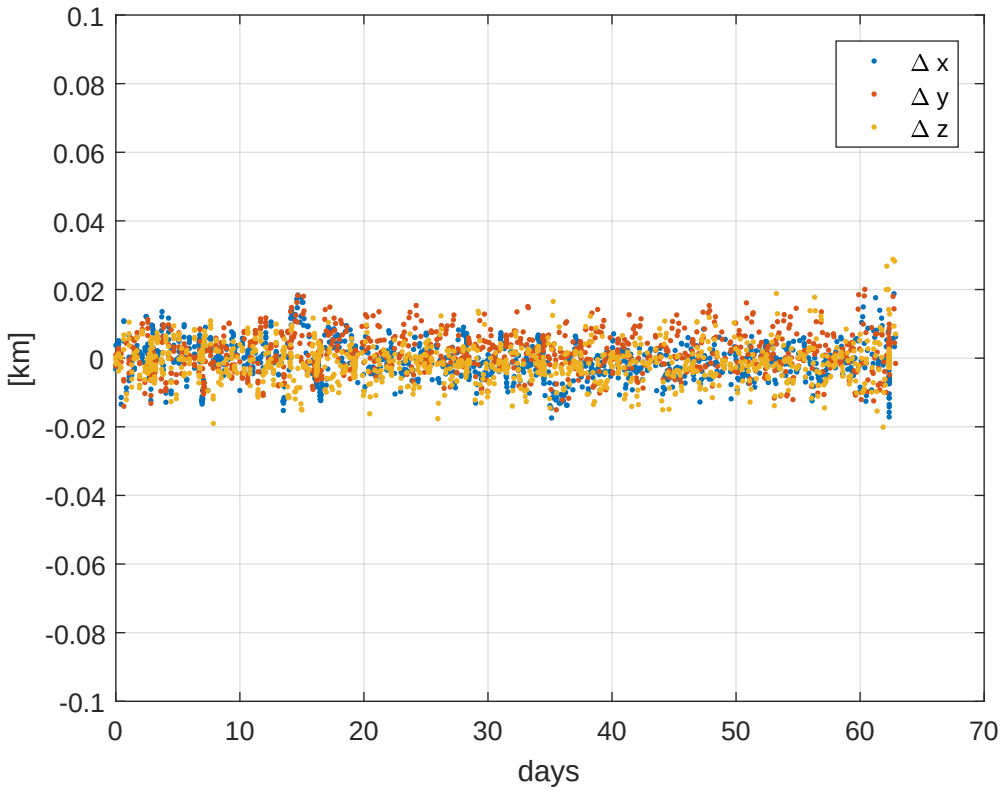

Figure 65: Residuals of OSINAC and NAVCAM camera positions after iterative integration of the euler equations over 60 days in 2016, beginning at 2016-04-19T04:20:27 UTC.

is in the order of 6 meters and probably will further decrease, as in Figure 72, after a full orbit reconstruction. Hence, any significant torque-free nutation cone would appear within this data, as illustrated in Figure 66. Here, the rotation axis has been rotated artificially by only 0.1 degrees. This change is smaller than the radius of the cone that was presumed and stated in [100]. However, it already results in significant additional periods that are markedly visible within the data.

The Euler equations have fully been solved for time frames of 50 days in 2014 (Figure 64) and 60 days in 2016 (Figure 65), showing no evidence for an excited rotational state. The orientation of the rotational axis changed throughout the mission, especially during perihelion. However, since no star-tracking is carried out within this work, the absolute orientation of the rotational axis with respect to the J2000 frame and its changes from 2014 until 2016 will not be discussed here.

4.3.3. The Gravitational Field

The gravitational field and the total mass of the comet has been discussed in several publications [89]. From the radio science investigations team, gravitational coefficients

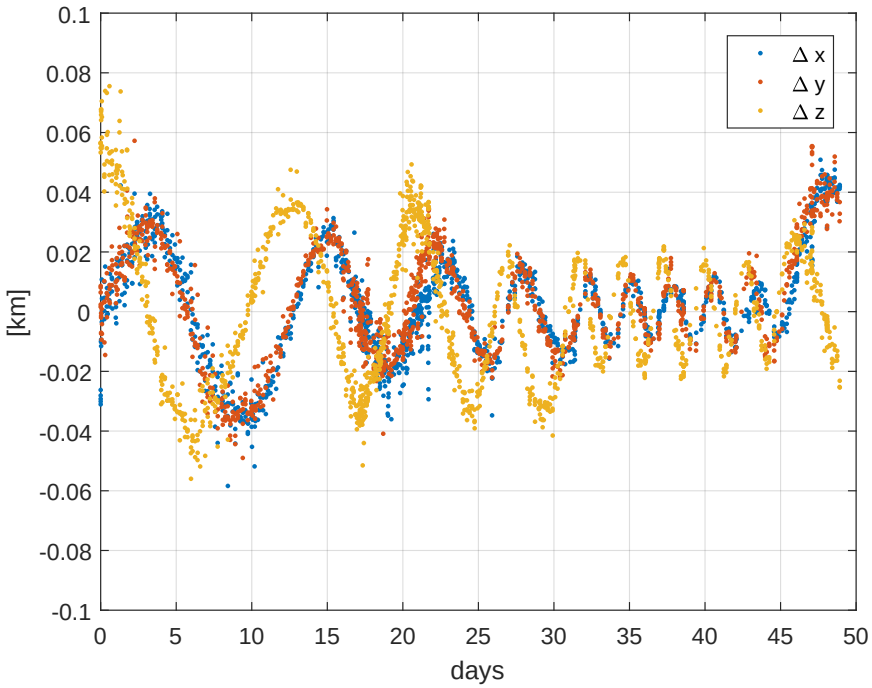

Figure 66: Residuals of OSINAC and NAVCAM camera positions beginning at 2014-09-09T02:04:34 UTC with a rotational axis that is **artificially rotated by 0.1 degrees** - only about two thirds of the amount of non-principal axis rotation that was presumed in [100]. It can be seen, that a non-principal axis rotation mode with a higher amplitude than this would be visible within the data processed within this work.

up to degree and order two have been estimated [96][95]. In [44], the Rosetta navigation team computed a gravity field up to degree and order five from the close orbits in 2016. However, altering solutions of the gravitational field were obtained for different orbits, showing inconsistencies, especially in the higher order terms. The solution provided by the navigation team was primarily used for the navigation around the comet. Within this work, a full orbit reconstruction has been carried out as previously described in subsection 3.3.2.

Over a time frame of 42 days, the closest orbits towards the very end of the mission were integrated. In this way, and concerning parameter correlation, the mass of the comet could be estimated as $GM = 665.71 \pm 0.43$ m^{3}s^{-2}. This value is slightly lower but, within the error bars of the result in [44], stated as $GM = 665.92 \pm 0.30$ m^{3}s^{-2} with 1σ. Note that all uncertainties of physical parameters have been given as 3σ or within a 99% confidence ellipsoid throughout this document. Hence, a smaller value of uncertainty could be obtained.

Figure 71 shows the obtained coefficients for a spherical harmonics expansion of the gravitational field of the comet up to degree and order four. As explained in subsection

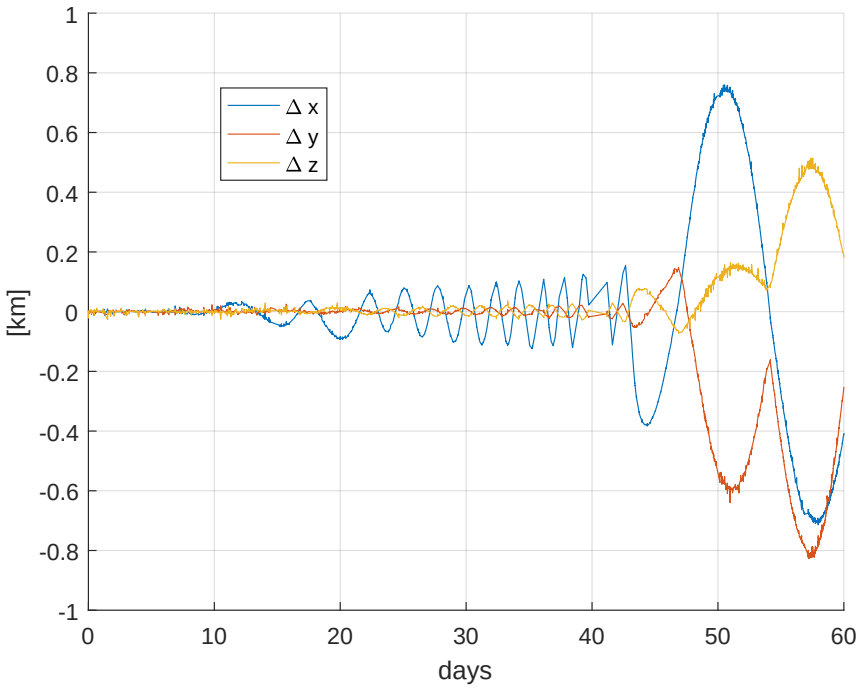

Figure 67: **Without torque:** Evolution of the error in relative spacecraft position for a constant rotational period. After only 10 days, an error resulting in an additional visible period can be seen; after 60 days, more than 0.8km error in the spacecraft position results.

2.2.5, the values of (C_{10}, C_{11}, S_{11}, C_{21}, S_{21}, S_{22}) are zero, since the body fixed frame containing all optical data is adjusted in a way that the origin of the resulting coordinate system is defined in the center of gravity of the comet and aligned along the axes of the main moments of inertia. Figures 68 and 69 illustrate the results of the gravitational field estimation.

The influence of coefficients up to degree and order seven could be shown with the optical data derived within this work, however, correlations become more pronounced if too many parameters are adjusted iteratively. Hence, the parameter uncertainties quickly grow to 100% and, therefore, gravitational field solutions with a degree and order higher than four are not realistic. Note, that within this work, the gravitational field of the comet is derived from optical data alone. Therefore, after the method has successfully been combined with Doppler and ranging data, higher order terms of the gravitational field might be revealed.

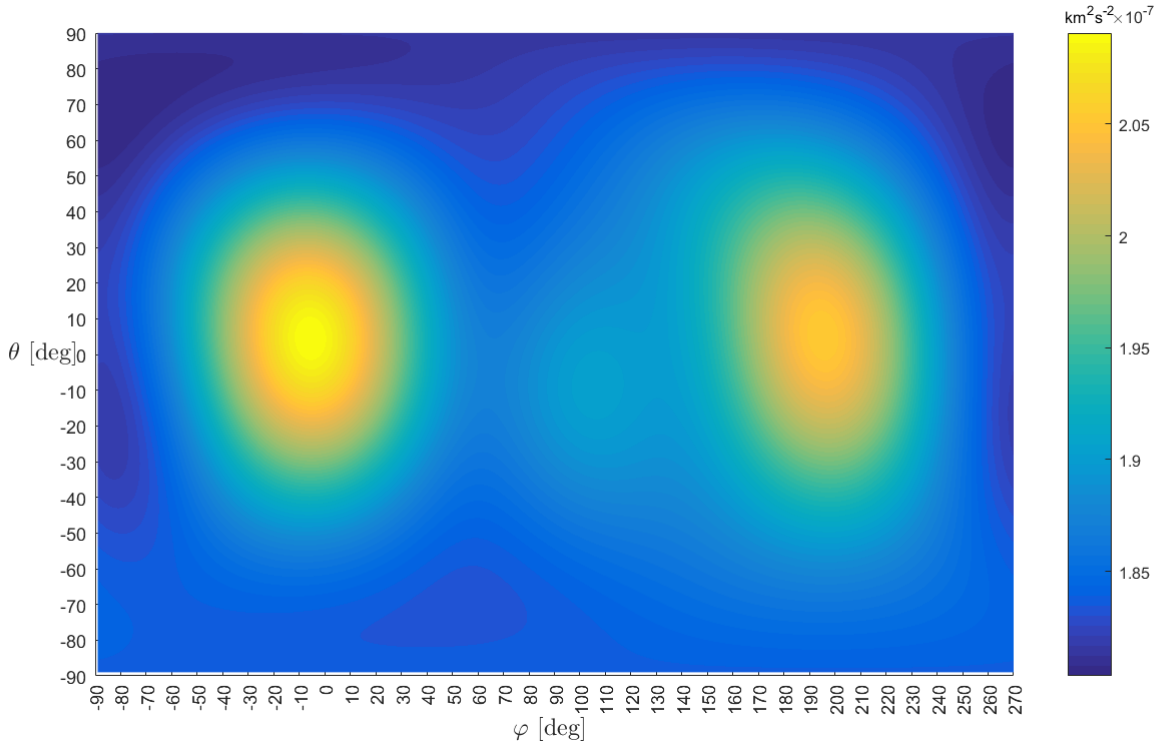

Figure 68: The gravitational potential of the comet as it appears at a distance of 3.5km. The bilobate shape of the comet is reflected markedly in the appearance of its gravitational field. In this plot, the small lobe appears on the left.

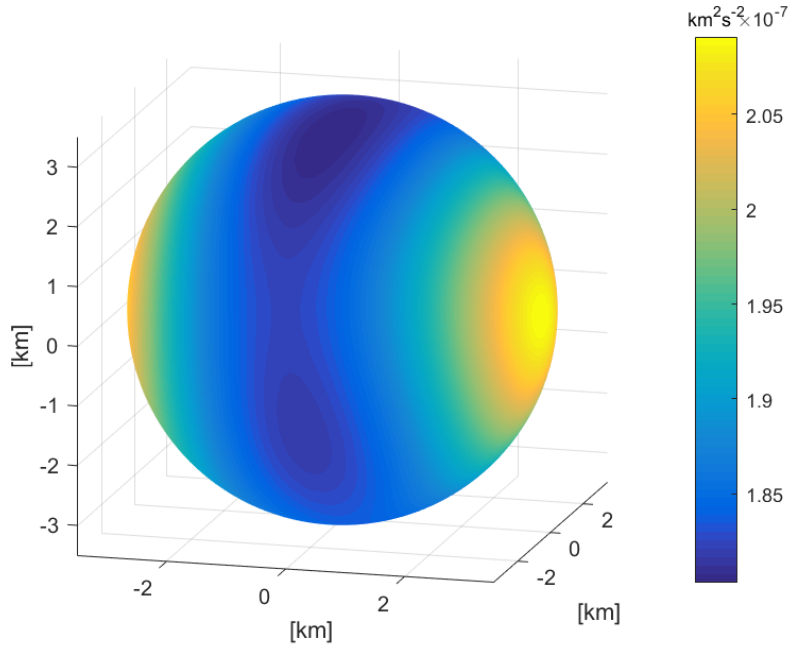

Figure 69: The gravitational potential of the comet plotted on a sphere with a radius of 3.5km.

Important quantities that enlarge the uncertainties of the estimated gravitational field parameters are wheel offloadings as introduced in subsection 3.3.3. In theory, during WoLs, the thrusters are active in a way that only a momentum is induced to stabilize the attitude of the spacecraft while running down the angular momentum of the reaction wheels inside. Hence, no acceleration should influence the trajectory of the spacecraft if the activity of the thrusters would be perfect. However, from a practical perspective, small imperfections result in small accelerations. Since the amount of the unplanned induced $\Delta\mathbf{v}$ is unknown, the gravitational field of the comet was estimated both with and without the consideration of the 42 parameters that are necessary to adjust the WoLs. The two different results can be seen in Figures 70 and 71. Both parameter estimations show a gravitational field that is close to the expected one for a homogeneous density distribution. However, as soon as WoLs are not considered, parameter correlations become less pronounced and smaller uncertainties can be obtained.

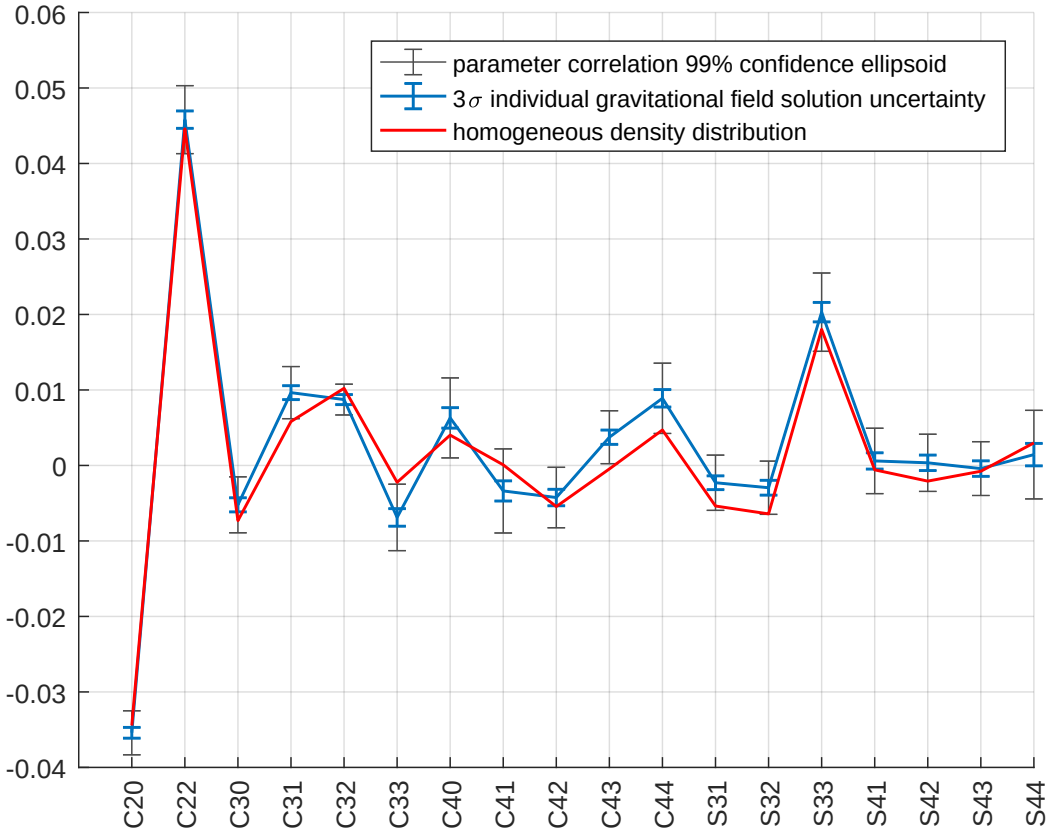

Figure 70: **Without wheel offloadings:** The normalized spherical harmonics coefficients of the gravitational field determined within this work. $R_\oplus$ was chosen to be 2.65 km. Note that almost all coefficients, including their uncertainties, are close within in the region of a homogeneous mass distribution inside the nucleus.

The difference in the respective residuals of camera positions is shown in Figures 72 and 73. For both parametrizations, no major changes in the residuals can be observed. The root mean square increases only from 4.06 to 4.13 meters, which strengthens the assumption that the WoLs resulted in negligible influence on the trajectory of the orbiter around the nucleus. However, as soon as Doppler data will be involved, the consideration of WoLs can be necessary again, since the Doppler measurement is very sensitive to changes in the relative velocity up to millimeters per second. Hence, the choice to adjust the WoLs remains in the software that was developed within this work.

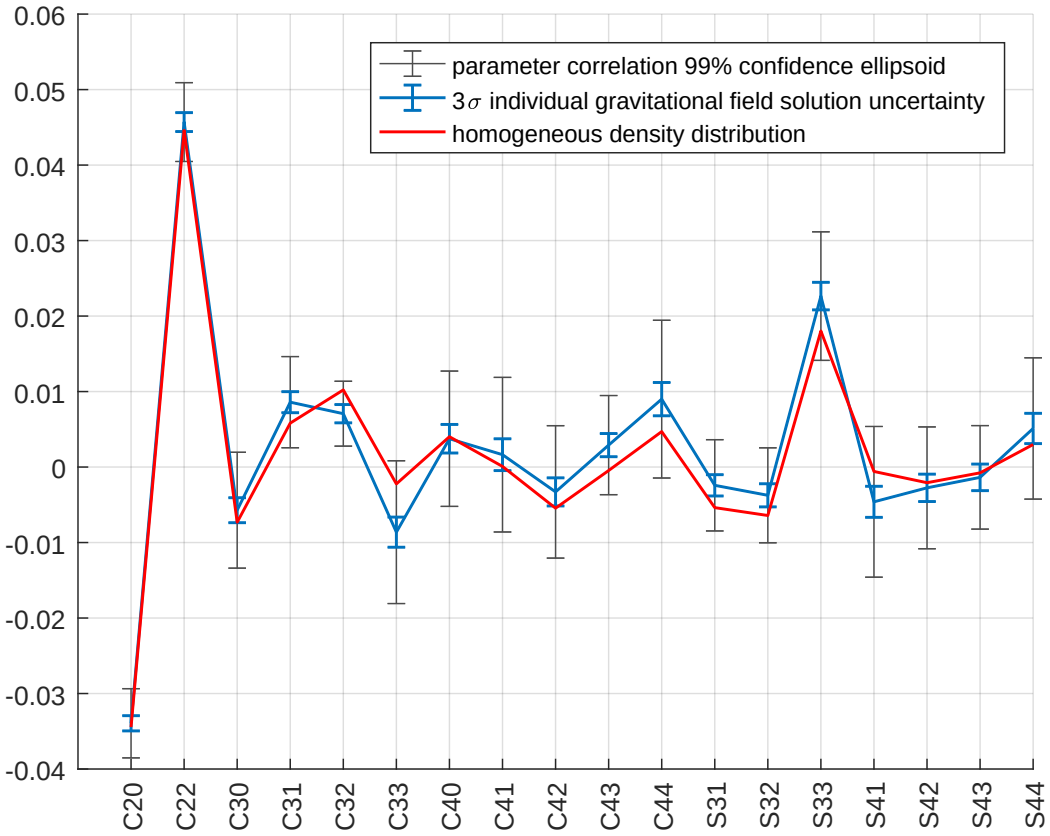

Figure 71: **Including wheel offloadings:** The normalized spherical harmonics coefficients of the gravitational field determined within this work. Only minor changes can be observed, however, the error bars are markedly enlarged when compared to Figure 70, where no WoLs have been adjusted.

In Figures 72 and 73, the residuals after 42 days of orbit integration are shown. A total of 500 NAVCAM and 200 OSIRIS-NAC images has been used to determine the spacecraft position relative to the comet. Gravitational field coefficients from a homogeneous density distribution were used as start values prior to the iteration; they were generated from the SHAP7 shape model, which was prepared from OSIRIS images [50][99][100]. The

usage of start values for a homogeneous nucleus **significantly improved the orbit reconstruction residuals even prior to iteration**. The derived gravitational field parameters together with the associated uncertainties can be found in Table 5.

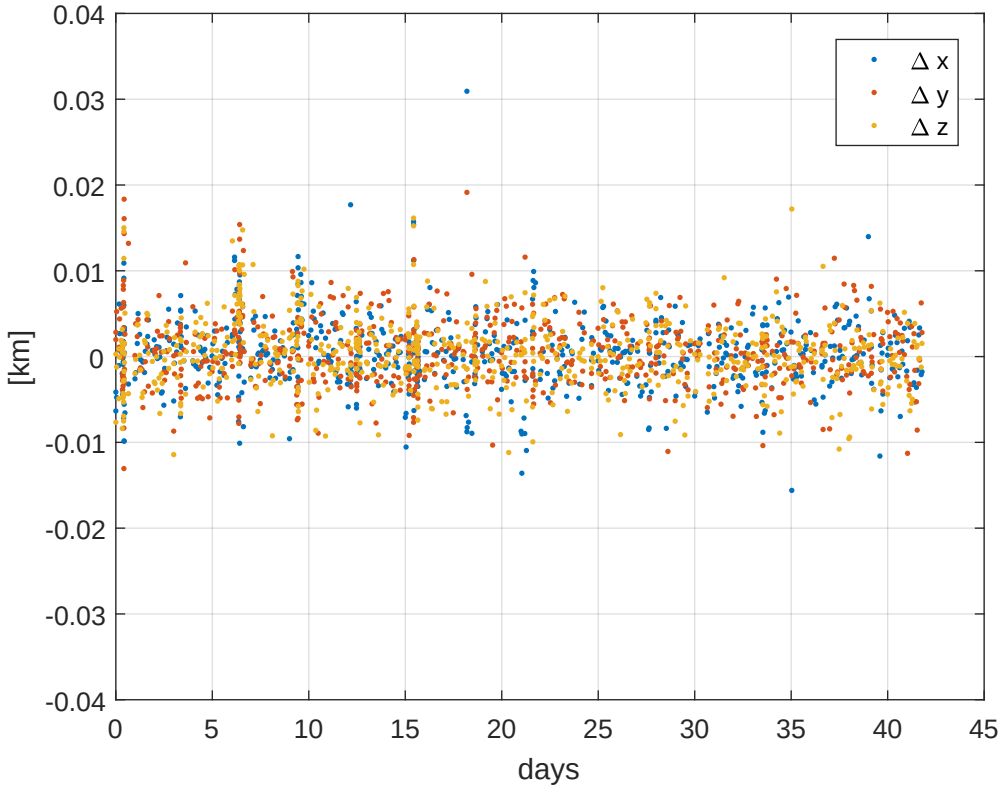

Figure 72: **Including wheel offloadings:** The residuals after convergence of the precise orbit determination tool. 28 consecutive data arcs were integrated using the derived gravitational field shown in Figure 68, starting from 2016-08-15T09:00:13 UTC. The root mean square residual between the reconstructed orbit trajectory and bundle adjustment derived camera position is 4.06 meters.

4.3.4. Combination with RSI Doppler Data

Besides the development of routines for the processing of optical data acquired during the Rosetta mission, another scientific goal of this work was the combination of the derived data with existing routines of the radio science investigations team (RSI).

All related tools were implemented in FORTRAN subroutines, complementing existing Doppler data by three-dimensional optical measurements relative to the comet. To stabilize the iterative estimation process, the Tikhonov regularization, as described in

subsection 2.7.2, was implemented. Software tests for data arcs from July 2016 showed **clear improvements in the stability and accuracy of the algorithm**. Both the Doppler frequency residuals and the parameter uncertainties decreased as soon as optical data was used additionally.

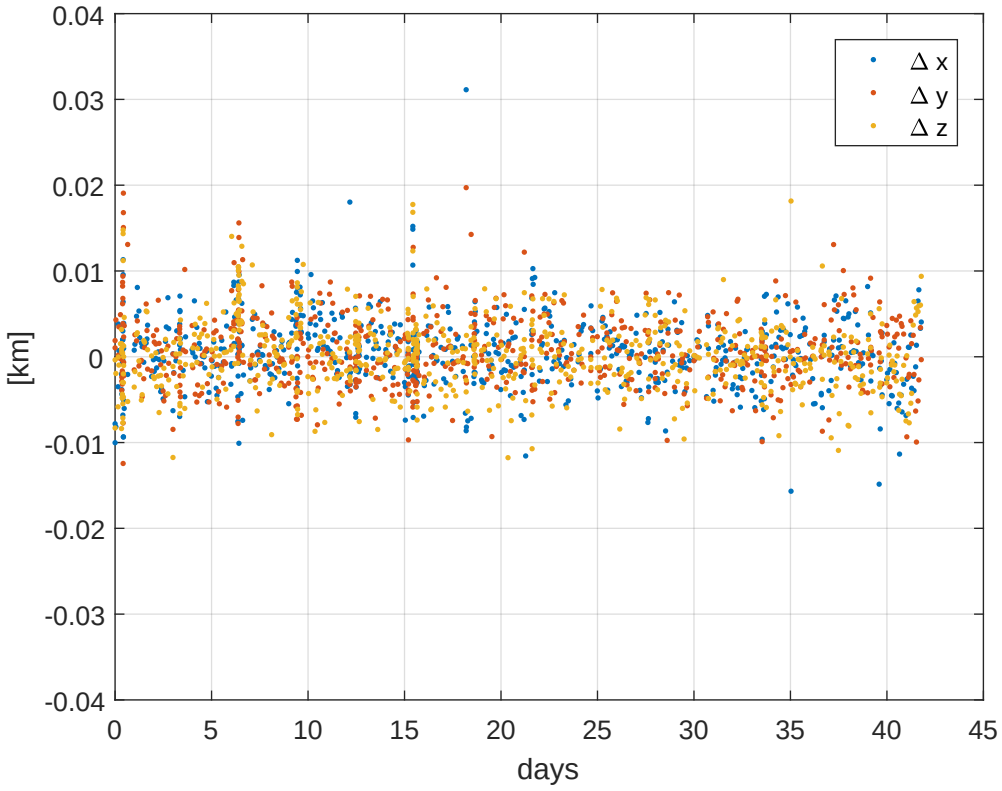

Figure 73: **Without wheel offloadings:** The same residuals as in Figure 72, but without the parametrization of WoLs. The result beginning at 2016-08-15T09:00:13 UTC does not show major changes, and the root mean square residual between the reconstructed orbit trajectory and bundle adjustment derived camera position is 4.13 meters. The 42 WoL parameters cause larger uncertainties while only a RMS improvement of 0.07 meters is the result.

However, the combined iteration of Doppler data together with optical data still suffers from an interesting effect that evolves especially from the nature of a comet: The orbit relative to the solar system is subject to significant non-gravitational perturbation due to the cometary outgassing. Consequently, the position of the comet in SPICE kernels shows deviations from its true position. These deviations currently **add a significant offset between the predicted and received frequency**. For this reason, new subroutines are being developed by RSI which allow for a more accurate recalculation of Churyumov-

Gerasimenko's orbit through the solar system. Hence, results from Doppler- and optical data combined processing will be published soon in the future.

	Value	Model	3-σ optical	Corr. optical	Corr. Doppler	Corr. combined
$GM \times 10^{-2}$	**6.6571**		0.0013	**0.0043**	0.0196	0.0024
C_{20}	**-0.0354**	-0.0344	0.0007	**0.0029**	0.0018	0.0010
C_{22}	**0.0458**	0.0446	0.0011	**0.0045**	0.0023	0.0012
C_{30}	**-0.0052**	-0.0073	0.0010	**0.0037**	0.0023	0.0013
C_{31}	**0.0096**	0.0058	0.0010	**0.0035**	0.0024	0.0015
C_{32}	**0.0087**	0.0102	0.0007	**0.0020**	0.0026	0.0011
C_{33}	**-0.0069**	-0.0022	0.0012	**0.0044**	0.0027	0.0015
C_{40}	**0.0063**	0.0040	0.0014	**0.0053**	0.0026	0.0016
C_{41}	**-0.0034**	0.0001	0.0013	**0.0056**	0.0029	0.0016
C_{42}	**-0.0043**	-0.0054	0.0011	**0.0040**	0.0029	0.0015
C_{43}	**0.0038**	-0.0005	0.0009	**0.0035**	0.0029	0.0016
C_{44}	**0.0089**	0.0047	0.0012	**0.0047**	0.0029	0.0016
S_{31}	**-0.0023**	-0.0054	0.0009	**0.0037**	0.0029	0.0014
S_{32}	**-0.0030**	-0.0064	0.0010	**0.0035**	0.0024	0.0012
S_{33}	**0.0203**	0.018	0.0013	**0.0052**	0.0025	0.0014
S_{41}	**0.0006**	-0.0009	0.0011	**0.0043**	0.0031	0.0017
S_{42}	**0.0003**	-0.0021	0.0010	**0.0038**	0.0030	0.0015
S_{43}	**-0.0004**	-0.0008	0.0010	**0.0036**	0.0029	0.0015
S_{44}	**0.0014**	0.0030	0.0015	**0.0059**	0.0028	0.0016

Table 5: An overview of the estimated parameters and the associated uncertainties. **Bold entries reflect real results derived within the work**, non-bold entries result from simulations or simplifications and give an overview of what can be expected after the combination of Doppler data and optical data. The last four columns show the uncertainties of the estimated parameters; only for the last three rows, parameter correlation was considered. The L2-norm of the gravitational coefficient uncertainties decreases to a value of **53%**, if the optical data processed within this work is used additionally to Doppler data.

In order to obtain an estimate of the improvement through the combination of Doppler data with optical data, however, within this work, an application was developed that simulates Doppler data from (46) with the assumption, that the orbit of the comet was known more precisely than currently. The received frequency was modeled with artificial Gaussian distributed noise of 3 millihertz at times when real measurements were made.

From this simulation, it could be derived that the uncertainty of the gravitational field parameters on average decreased to **a value of 53%**, as soon as optical data was used additionally. Hence, once the orbit of the comet through the solar system will be known more accurately, a more precise estimate of the cometary gravitational field can be expected. Table 5 reflects the results and the uncertainties resulting from the different measurement methods, and through their combination.

The gravitational field estimated within this work only shows small deviations from an expected appearance for a homogeneous density distribution inside the nucleus. However, some uncertainties in Figure 70 are close to reveal small inhomogeneities. As soon as the uncertainties are replaced by the ones that can be expected from the last row in Table 5 through the combination of optical data with Doppler data, more details about the inner structure of comet Churyumov-Gerasimenko will be known.

In general, however, a predominantly homogeneous density distribution inside the nucleus confirms fundamental aspects in the theory of solar system evolution. It is presumed that comets have formed from gravitational and streaming instabilities in solar nebula clouds of millimeter- to centimeter sized agglomerates [15]. Pebbles of this size could be made visible through the CIVA images sent from the lander Philae.

Most likely, the origin of Churyumov-Gerasimenko is the Kuiper belt; this region is far away from the Sun, which results in low orbital velocities of particles. Thus, impacts and collisions with high velocity are very unlikely; contacts of matter in the Kuiper belt occur slowly. Additionally, no thermal or aqueous alterations affect the material [14]. Hence, before becoming a Jupiter-family comet, the nucleus of Churyumov-Gerasimenko formed at a large solar distance in cold and smooth low velocity conditions.

With the processes described above, no major inhomogeneities within the cometary material can be expected - a homogeneous density distribution inside the nucleus is most likely. Hence, with the results derived within this work, a small part in the theory of solar system evolution can be confirmed.

5. Conclusion and Outlook

The main goal of this work was the development of methods which enable the extraction of the camera position relative to a target body based on images taken during the orbit of the spacecraft. Once the spacecraft positions were derived with smallest possible uncertainties, they should be combined with existing routines of the Radio Science Investigations experiment to obtain estimates of the physical properties of the target body with an improved accuracy. The main small-body for the test and evaluation of all components was the target of the Rosetta mission, comet Churyumov-Gerasimenko.

The software that has been developed was subdivided into three main components: The feature detection and matching algorithm, robust sparse bundle adjustment and the collection of all tools for physical parameter estimation. All subroutines were designed in a way that each software component is modular and exchangeable. Hence, each algorithm can easily be adapted to a new mission, such as Lucy or Hera, for example. Lucy was launched on 16 October 2021 and will visit different asteroids including Jupiter trojans. Hera is planned to visit the asteroid Didymos; it is going to evaluate the effects of the impact from the Double Asteroid Redirection Test (DART) on it's satellite Dimorphos.

For the first algorithm that detects features and tracks them over consecutive image series, a novel combination of methods was introduced. Distinctive features initially were automatically detected by the scale invariant feature transform and subsequently matched with a least squares matching approach based on polynomials. From the triangulated and subsequently reprojected surface reference grid into multiple camera reference frames, a block matching could be obtained. It allowed for more than hundred observations of single surface points from a broad variety of illumination conditions, viewing angles, and scales. The matching process enables a subpixel-accurate determination of the tie point location within the image frame. Depending on the scenario and the amount of change in illumination conditions, the user of the software package can additionally enable light correction – a method that predicts reprojected pixel brightness depending on surface illumination, and based on the combination of reflectance models.

Additionally, a routine that enables the construction of a digital elevation model from surface reflectance was implemented. This tool allowed for the reconstruction of a surface element with a resolution of less than 5 cm, acquired from Osiris-Nac images taken during Rosetta's final descent in 2016. The result can be helpful to constrain the cometary surface roughness for the bistatic radar experiment executed with the RSI experiment in 2014.

To obtain the spacecraft position from the subpixel-accurate tie point measurements, a sparse bundle adjustment technique was used, which is robust with respect to corrupted measurements. The main difference is, that in comparison with commonly used robust methods no outlier removal with a σ-edit rule is necessary within the approach. Instead, the statistical model is adapted by assuming that the noise is determined by the Student's t-distribution. This leads to superior stability and accuracy in comparison with methods that utilize σ-edit rules, since outliers are much more likely within the Student's t-distribution. Since the iterative estimation problem of the bundle adjustment with 36.88×10^6 optical measurements results in a large computational cost, the sparsity of the problem was used and all computational expensive routines were implemented on a cluster.

The Student's t bundle adjustment resulted in a reprojection RMS of 0.6 pixels. Hence, it could be confirmed, that subpixel accuracy was reached within the developed feature detection and matching software. The algorithm results in a higher accuracy than the state of the art method introduced in [24], resulting in a reprojection RMS of 0.7 pixels. Additionally, 1.93×10^6 surface points were used instead of the 10481 landmarks used by flight dynamics. The mean 1σ uncertainty for all NAVCAM derived positions is 10 meters, and 5 meters for the OSINAC respectively. The mean uncertainty for NAVCAM images taken in the close orbits during the end of mission phase is 3.7 meters. Single OSINAC images resulted in uncertainties smaller than 1 meter. Hence, a spacecraft position uncertainty on a centimeter level could be reached within several images. The combination of the derived spacecraft positions with existing RSI routines showed a clear improvement in both the stability and the accuracy within the iterative estimation software.

The third part of software was developed to estimate physical parameters of the comet. An increase of the rotational period in 2014 as well as a decrease in 2016 could accurately be determined, confirming predictions that were published prior to the arrival at the comet. Interestingly, towards the end of the mission in September 2016 at 3.8 AU, the comet still shows a significant angular acceleration, indicating that cometary outgassing is still an important effect to consider during that period. No evidence of a non-principal axis rotation could be found.

An estimate of the gravitational field of the comet up to degree and order four of gravitational field coefficients in spherical harmonics could successfully be derived. It could be shown, that the higher order terms still have a measurable influence on the spacecraft's trajectory within the uncertainties of the derived camera positions. The solution covers 28 data arcs over 42 days during the end of mission phase with a RMS resid-

ual of 4.13 meters in the reconstructed orbit when compared to the derived spacecraft positions. As expected and predicted in previous publications, the comet appears to have a predominantly homogeneous density distribution inside the nucleus. The result confirms the basic theory of solar system evolution.

The optical data processed within this work will be complemented by the ranging- and Doppler data, which is currently being processed by the RSI team. These additional measurements will help to decorrelate the gravitational field parameters and to better constrain the solution as it was shown in section 4. With the theory, the developed novel methods and algorithms, and the results discussed within this work, the basis for a more accurate determination of the gravitational field parameters of comet Churyumov-Gerasimenko was successfully created.

Outlook

After the routines developed within this work have successfully been combined with existing RSI methods, still additional research should be accomplished. First, after a recalibration by the Osiris team, the Osiris-Wac now has a directional accuracy comparable to the Navcam. Hence, all Osiris-Wac derived images should be processed as well and included in the orbit reconstruction.

Another important step is to use a more sophisticated model of the cometary outgassing, since the resulting perturbing force has a significant influence on the spacecraft orbit, especially in close proximity.

Since the shape of the comet can better be approximated by an ellipsoid, the gravitational field could be estimated from an ellipsoidal harmonics expansion in the future [101]. Even more accurate would be a bipolar approach, which is currently being developed from the RSI scientists.

As stated before, the Osiris-Nac shows small differences in its directional calibration depending on the filter or the temperature. Hence, an auto-calibration method could be used within the bundle adjustment, and therefore, maybe further improve the reprojection RMS.

These topics would exceed the envelope of this work, however, it is definitely worthwhile to investigate them in future research and publications. Five years after Rosetta has descended to comet Churyumov-Gerasimenko, still exciting questions are left to be discussed.

A. Appendix

A.1. The Gamma Function

The Gamma function is defined as

$$\Gamma(x) = \int_0^\infty t^{x-1} e^{-t} \mathrm{d}t. \tag{234}$$

A.2. Euler's Equations

In principal orthogonal coordinates, Euler's rotation equations are defined as [72]

$$\begin{aligned} M_1 =& \Theta_1 \dot{\omega}_1 + (\Theta_3 - \Theta_2)\omega_2\omega_3 = \dot{L}_1 + \left(\frac{1}{\Theta_2} - \frac{1}{\Theta_3}\right) L_2 L_3, \\ M_2 =& \Theta_2 \dot{\omega}_2 + (\Theta_1 - \Theta_3)\omega_3\omega_1 = \dot{L}_2 + \left(\frac{1}{\Theta_3} - \frac{1}{\Theta_1}\right) L_3 L_1, \\ M_3 =& \Theta_3 \dot{\omega}_3 + (\Theta_2 - \Theta_1)\omega_1\omega_2 = \dot{L}_3 + \left(\frac{1}{\Theta_1} - \frac{1}{\Theta_2}\right) L_1 L_2. \end{aligned} \tag{235}$$

Here, $M_1 - M_3$ denotes the torque, $\Theta_1 - \Theta_3$ the moments of inertia, $L_1 - L_3$ denotes the angular momentum, $\omega_1 - \omega_3$ and $\dot{\omega}_1 - \dot{\omega}_3$ are the angular velocities and the angular accelerations, respectively. In this work, (235) is numerically solved to determine the rotational state of the comet.

A.3. Determinant and Trace of a Matrix

The determinant of a matrix $\mathrm{A} \in \mathbb{R}^{2\times 2}$ is a scalar value and can be obtained from [73]

$$\det(\mathrm{A}) = \begin{vmatrix} a_{11} & a_{12} \\ a_{21} & a_{22} \end{vmatrix} = a_{11}a_{22} - a_{21}a_{12}. \tag{236}$$

In general, for matrices $\mathrm{A} \in \mathbb{R}^{n\times n}$, the determinant can be obtained recursively from [73]

$$\det(\mathrm{A}) = \sum_{j=1}^{n} (-1)^{i+j} a_{ij} S_{ij}, \tag{237}$$

where a_{ij} denotes the entry of the $i-$th row and the $j-$th column of matrix A and S_{ij} is the determinant of the submatrix that is obtained if the $i-$th row and the $j-$th column of A is removed. The trace of a matrix $\mathrm{A} \in \mathbb{R}^{n \times n}$ can be obtained from [73]

$$\mathrm{tr}(\mathrm{A}) = \sum_{i=1}^{n} a_{ii}, \tag{238}$$

which equals the sum of all entries on the main diagonal of it.

A.4. Skew-Symmetric Matrices

A skew-symmetric matrix may be written as

$$[\mathbf{v}]_{\times} \coloneqq \begin{bmatrix} 0 & -v_z & v_y \\ v_z & 0 & -v_x \\ -v_y & v_x & 0 \end{bmatrix}, \tag{239}$$

with the relation [52]

$$\mathbf{v} \times \mathbf{b} = [\mathbf{v}]_{\times} \mathbf{b} = \left(\mathbf{v}^{\mathsf{T}} [\mathbf{b}]_{\times}\right)^{\mathsf{T}}. \tag{240}$$

In general, a matrix is symmetric if $\mathrm{A}^{\mathsf{T}} = \mathrm{A}$ and skew-symmetric if $\mathrm{A}^{\mathsf{T}} = -\mathrm{A}$ [52].

A.5. The Pseudo-Inverse

With the singular value decomposition $\mathrm{A} = \mathrm{UDV}^{\mathsf{T}}$ of a matrix $\mathrm{A} \in \mathbb{R}^{m \times n}$ with $m \geq n$, the pseudo-inverse A^{+} can be obtained from

$$\mathrm{A}^{+} = \mathrm{V}\mathrm{D}^{+}\mathrm{U}^{\mathsf{T}}, \tag{241}$$

where D^{+} is defined as

$$\mathrm{D}^{+} = \begin{cases} 0 & \text{if } D_{ii} = 0, \\ D_{ii}^{-1} & \text{otherwise.} \end{cases} \tag{242}$$

More information can be found in [52].

A.6. OSIRIS-NAC Geometric Distortion Removal

For the Osiris-Nac, a geometric calibration curve is available. The correction values are fitted to a two dimensional, third-order polynomial. The undistorted pixel positions (X_u, Y_u) are expressed as a function of the actual image coordinates by [37]

$$\begin{aligned} X_u &= \sum_{i,j} k_{x_{i,j}} X_0^i Y_0^j, \\ Y_u &= \sum_{i,j} k_{y_{i,j}} X_0^i Y_0^j. \end{aligned} \tag{243}$$

The full table of third-order polynomial fit coefficients for distortion removal can be found in table 6 [37].

i	j	k_x	k_y
0	0	-9.09076000E+00	4.61801000E+00
0	1	9.06443000E-04	9.97063000E-01
0	2	-5.26902000E-07	-5.93490000E-07
0	3	-3.32516000E-12	1.99967000E-10
1	0	1.01413000E+00	3.21866000E-03
1	1	-2.39320000E-07	-3.38901000E-06
1	2	1.19823000E-10	1.88602000E-12
1	3	-2.01772000E-16	-1.95971000E-17
2	0	-4.71201000E-06	-6.41550000E-08
2	1	8.98608000E-12	1.16434000E-10
2	2	-7.17827000E-16	-1.12755000E-16
2	3	2.23917000E-19	3.01745000E-20
3	0	2.91214000E-10	-1.06652000E-11
3	1	-1.94627000E-16	-4.15382000E-17
3	2	2.20615000E-19	3.98303000E-20
3	3	-6.87882000E-23	-1.09102000E-23

Table 6: The coefficients for the removal geometric distortion [37].

B. References

[1] Č. Albl and T. Pajdla. Global camera parameterization for bundle adjustment. In *2014 International Conference on Computer Vision Theory and Applications (VISAPP)*, volume 3, pages 555–561. IEEE, 2014.

[2] K. Altwegg. ROSINA user's guide / RO-ROS-UG-1000 / Issue: 1 / Revision: 1.1, 2019.

[3] T. Andert. *Masses of small bodies: mass estimation of small solar system bodies using radio science data from close flybys*. PhD thesis, Universität zu Köln, 2010.

[4] A. Aravkin. *Robust methods for Kalman filtering/smoothing and bundle adjustment*. PhD thesis, University of Washington, 2010.

[5] A. Aravkin, M. Styer, Z. Moratto, A. Nefian, and M. Broxton. Student's t robust bundle adjustment algorithm. In *2012 19th IEEE International Conference on Image Processing*, pages 1757–1760. IEEE, 2012.

[6] R. C. Aster, B. Borchers, and C. H. Thurber. *Parameter estimation and inverse problems*. Elsevier, 2018.

[7] N. Attree, L. Jorda, O. Groussin, S. Mottola, N. Thomas, Y. Brouet, E. Kührt, M. Knapmeyer, F. Preusker, F. Scholten, et al. Constraining models of activity on comet 67P/Churyumov-Gerasimenko with Rosetta trajectory, rotation, and water production measurements. *Astronomy & Astrophysics*, 630:A18, 2019.

[8] Y. Bar-Shalom, X. R. Li, and T. Kirubarajan. *Estimation with applications to tracking and navigation: theory algorithms and software*. John Wiley & Sons, 2004.

[9] H. Bay, T. Tuytelaars, and L. Van Gool. SURF: speeded up robust features. In *European conference on computer vision*, pages 404–417. Springer, 2006.

[10] M. Berry and V. Coppola. Correct modeling of the indirect term for third body perturbations (AAS 07-417). *Advances in the Astronautical Sciences*, 129(3):2625, 2008.

[11] J.-L. Bertaux. Estimate of the erosion rate from H2O mass-loss measurements from SWAN/SOHO in previous perihelions of comet 67P/Churyumov-Gerasimenko and connection with observed rotation rate variations. *Astronomy & Astrophysics*, 583: A38, 2015.

[12] F. Bethmann and T. Luhmann. Least-squares matching with advanced geomet-

ric transformation models. *International Archives of Photogrammetry, Remote Sensing and Spatial Information Sciences*, 38(Part 5):86–91, 2010.

[13] C. Bielsa, M. Müller, and U. Herfort. Operational approach for the modeling of the coma drag force on Rosetta. In *Proceedings 24th International Symposium on Space Flight Dynamics, 24th ISSFD, Laurel, USA*, 2014.

[14] J. Blum. Yet more evidence that comet 67P formed by gravitational instability of a pebble cloud - presentation. Institut für Geophysik und extraterrestrische Physik, Technische Universität Braunschweig, Germany. URL https://www.astro.uni-jena.de/~pfe2017/talks/4-1%20Blum.pdf. Accessed: 2021.

[15] J. Blum, B. Gundlach, S. Mühle, and J. M. Trigo-Rodriguez. Comets formed in solar-nebula instabilities!–An experimental and modeling attempt to relate the activity of comets to their formation process. *Icarus*, 235:156–169, 2014.

[16] D. Bussey, M. Robinson, K. Edwards, P. Thomas, J. Joseph, S. Murchie, J. Veverka, and A. Harch. 433 Eros global basemap from NEAR Shoemaker MSI images. *Icarus*, 155(1):38–50, 2002.

[17] C. Güttler, H. Sierks. OSIRIS georeferenced data products / RO-RIS-MPAE-TN-089 / Issue: 1 / Revision: a, 2018.

[18] C. Tubiana, H. Sierks. Software interface specification for OSIRIS science products / RO-RIS-MPAE-ID-023 / Issue: 1 / Revision: e, 2018.

[19] C. Capanna, G. Gesquière, L. Jorda, P. Lamy, and D. Vibert. Three-dimensional reconstruction using multiresolution photoclinometry by deformation. *The Visual Computer*, 29(6):825–835, 2013.

[20] D. T. Cassidy et al. A multivariate Student's t-distribution. *Open Journal of Statistics*, 6(03):443, 2016.

[21] F. Castellini, D. Antal-Wokes, R. P. de Santayana, and K. Vantournhout. Far approach optical navigation and comet photometry for the Rosetta mission. In *Proceedings of the 25th International Symposium on Space Flight Dynamics (ISSFD'15)*, 2015.

[22] B. J. Davidsson, S. Birch, G. A. Blake, D. Bodewits, J. P. Dworkin, D. P. Glavin, Y. Furukawa, J. I. Lunine, J. L. Mitchell, A. N. Nguyen, et al. Airfall on comet 67P/Churyumov–Gerasimenko. *Icarus*, 354:114004, 2021.

[23] R. P. de Santayana and M. Lauer. Optical measurements for Rosetta navigation near the comet. In *Proceedings of the 25th International Symposium on Space*

Flight Dynamics (ISSFD), Munich, 2015.

[24] R. P. de Santayana, M. Lauer, P. Muñoz, and F. Castellini. Surface characterization and optical navigation at the Rosetta flyby of asteroid Lutetia. In *International Symposium on Space Flight Dynamics*, 2014.

[25] T. Dorfmüller et al. *Lehrbuch der Experimentalphysik, Band 1, Mechanik, Relativität, Wärme*. Walter de Gruyter, Berlin, New York, 11. Auflage, 1998.

[26] Y. Dufournaud, C. Schmid, and R. Horaud. Matching images with different resolutions. In *Proceedings IEEE Conference on Computer Vision and Pattern Recognition. CVPR 2000 (Cat. No. PR00662)*, volume 1, pages 612–618. IEEE, 2000.

[27] A. Eibner, R. S. Harris, G. Gebauer, T. Leissle, and M. Richner. Rosetta technical note - coordinate systems for Rosetta / RO-DSS-TN-1081 / Issue: 6d, 2003.

[28] M. R. El-Maarry, O. Groussin, N. Thomas, M. Pajola, A.-T. Auger, B. Davidsson, X. Hu, S. F. Hviid, J. Knollenberg, C. Güttler, et al. Surface changes on comet 67P/Churyumov-Gerasimenko suggest a more active past. *Science*, 355(6332): 1392–1395, 2017.

[29] M. R. El-Maarry, O. Groussin, H. Keller, N. Thomas, J.-B. Vincent, S. Mottola, M. Pajola, K. Otto, C. Herny, and S. Krasilnikov. Surface morphology of comets and associated evolutionary processes: a review of Rosetta's observations of 67p/Churyumov–Gerasimenko. *Space science reviews*, 215(4):1–33, 2019.

[30] European Space Agency. Archive image browser, 2021. URL https://imagearchives.esac.esa.int/.

[31] European Space Agency. ESA Rosetta website, 2021. URL https://rosetta.esa.int.

[32] European Space Agency / Directorate of Operations and Infrastructure / Ground Systems Engineering Department. ROSETTA / MARS EXPRESS / VENUS EXPRESS mission control system (MCS) data delivery interface document DDID RO-ESC-IF-5003 / MEX-ESC-IF-5003 / VEX-ESC-IF-5003 appendix H / FD products / Issue 4.4, 2013.

[33] European Space Agency / Science Operations Department / Solar System Science Operations Division. ROSETTA payload boresight alignment details RO-EST-TN-3305 / Issue: 2 / Revision: g, 2014.

[34] F. Scholten et al. Reference frames and mapping schemes of comet 67P. 2015.

[35] M. Fairbairn. Principles of planetary photometry - image from website, 2004. URL http://orca.phys.uvic.ca/~tatum/plphot. Accessed: 2020.

[36] R. Förstner. Skriptum „Weltraumphysik". Institute of Space Technology and Space Application (ISTA), Universität der Bundeswehr, München.

[37] G. Kovacs, H. Sierks. OSIRIS camera distortion correction parameters / RO-RIS-MPAE-TN-081 / Issue: 1 / Revision: b, 2018.

[38] R. Gaskell, O. Barnouin-Jha, D. J. Scheeres, A. Konopliv, T. Mukai, S. Abe, J. Saito, M. Ishiguro, T. Kubota, T. Hashimoto, et al. Characterizing and navigating small bodies with imaging data. *Meteoritics & Planetary Science*, 43(6): 1049–1061, 2008.

[39] B. Geiger. Rosetta navigation camera images - presentation. Rosetta Operations Workshop - 2014/05/21 - Madrid.

[40] B. Geiger and M. Barthelemy. Rosetta navigation camera dataset deliveries - presentation. DAWG SWT40 - 2015/03/04 - ESTEC.

[41] B. Geiger, M. Barthelemy, and C. Archibald. ROSETTA-NAVCAM to planetary science archive interface control document / RO-SGS-IF-0001 / Version 4.3, 2016.

[42] B. Geiger, R. Andrés, and T. Statella. Radiometric calibration of the Rosetta navigation camera. *Journal of Astronomical Instrumentation*, 10(01):2150004, 2021. doi: 10.1142/S2251171721500045. URL https://doi.org/10.1142/S2251171721500045.

[43] B. Godard, F. Budnik, P. Munoz, T. Morley, and V. Janarthanan. Orbit determination of Rosetta around comet 67P/Churyumov-Gerasimenko. In *Proceedings 25th International Symposium on Space Flight Dynamics–25th ISSFD, Munich, Germany*, 2015.

[44] B. Godard, F. Budnik, G. Bellei, P. Muñoz, and T. Morley. Multi-arc orbit determination to determine Rosetta trajectory and 67P physical parameters. In *Proceedings 26th International Symposium on Space Flight Dynamics–26th ISSFD, Matsuyama, Japan*, 2017.

[45] A. Gruen. Adaptive least squares correlation: a powerful image matching technique. *South African Journal of Photogrammetry, Remote Sensing and Cartography*, 14(3):175–187, 1985.

[46] A. Gruen. Least squares matching: a fundamental measurement algorithm. *Close range photogrammetry and machine vision*, 1996.

[47] A. Gruen. Development and status of image matching in photogrammetry. *The Photogrammetric Record*, 27(137):36–57, 2012.

[48] P. J. Gutiérrez, L. Jorda, N. H. Samarasinha, and P. Lamy. Outgassing-induced effects in the rotational state of comet 67P/Churyumov—Gerasimenko during the Rosetta mission. *Planetary and Space Science*, 53(11):1135–1145, 2005.

[49] P. J. Gutiérrez, L. Jorda, R. Gaskell, B. J. Davidsson, C. Capanna, S. Hviid, H. Keller, L. Maquet, S. Mottola, F. Preusker, et al. Possible interpretation of the precession of comet 67P/Churyumov-Gerasimenko. *Astronomy & Astrophysics*, 590:A46, 2016.

[50] M. Hahn. Personal communication. Rheinisches Institut für Umweltforschung an der Universität zu Köln, Abteilung Planetenforschung, Aachenerstrasse 209, D-50931 Köln, Germany, 2021.

[51] R. Hartley and P. Sturm. Triangulation. *Computer Vision and Image Understanding*, 68(2):146–157, 1997. ISSN 1077-3142. doi: https://doi.org/10.1006/cviu.1997.0547. URL https://www.sciencedirect.com/science/article/pii/S1077314297905476.

[52] R. Hartley and A. Zisserman. *Multiple view geometry in computer vision, second edition*. Cambridge University Press, 2003.

[53] B. Häusler. Radio Science Messungen im Sonnensystem mit einer Einführung in die Theorie der Gravitation, Forschungsbericht. Technical report, LRT-WE-9-FB-2, 2002.

[54] B. Häusler, W. Eidel, D. Hagl, S. Remus, J. Selle, and M. Pätzold. Venus Express Radio Science Experiment VeRa. Reference Systems and Techniques used for the Prediction of Atmospheric and Ionospheric Measurements at Planet Venus. Technical report, Univ. d. Bundeswehr München, Forschungsbericht and Technical Note, VEX-VERA-UBW-TN-3040, 2003.

[55] B. Häusler, W. Eidel, R. Mattei, and S. Remus. The Planetary Doppler Effect in a Relativistic Treatment. Technical report, Univ. d. Bundeswehr, Forschungsbericht, LRT 9-FB-5, 2007.

[56] H. Hu and B. Wu. Bound-constrained Multiple-image least-squares matching for multiple-resolution images. *Photogrammetric Engineering & Remote Sensing*, 83 (10):667–677, 2017.

[57] S. F. Hviid. Optical, spectroscopic, and infrared remote imaging system plane-

tary science archive interface control document, RO-RIS-MPAE-ID-015, Issue: 3, Revision: e, 2011.

[58] J. Deller, H. Sierks. OSIRIS science user guide / RO-RIS-MPAE-MA-011 / Issue: 2 / Revision: a, 2018.

[59] R. Jacob. Massenbestimmung eines Asteroiden aus Dopplerdaten - Studienarbeit. Institute of Space Technology and Space Application (ISTA), Universität der Bundeswehr, München, 2010.

[60] R. Jacob. Simulation von Dopplerdaten der Raumsonde Rosetta - Bachelorarbeit. Institute of Space Technology and Space Application (ISTA), Universität der Bundeswehr, München, 2011.

[61] R. Jacob. Verwendung von elliptischen Koordinaten zur Berechnung der Beschleunigungen durch das Schwerefeld eines unregelmäßig geformten Körpers - Masterarbeit. Institute of Space Technology and Space Application (ISTA), Universität der Bundeswehr, München, 2012.

[62] L. Jorda, R. Gaskell, C. Capanna, S. Hviid, P. Lamy, J. Ďurech, G. Faury, O. Groussin, P. Gutiérrez, C. Jackman, et al. The global shape, density and rotation of comet 67P/Churyumov-Gerasimenko from preperihelion Rosetta/OSIRIS observations. *Icarus*, 277:257–278, 2016.

[63] D. Jupp and K. Vozoff. Stable iterative methods for the inversion of geophysical data. *Geophysical Journal International*, 42(3):957–976, 1975.

[64] H. U. Keller, C. Barbieri, P. Lamy, H. Rickman, R. Rodrigo, K.-P. Wenzel, H. Sierks, M. F. A'Hearn, F. Angrilli, M. Angulo, et al. OSIRIS–the scientific camera system onboard Rosetta. *Space science reviews*, 128(1):433–506, 2007.

[65] H. U. Keller, S. Mottola, Y. Skorov, and L. Jorda. The changing rotation period of comet 67P/Churyumov-Gerasimenko controlled by its activity. *Astronomy & Astrophysics*, 579:L5, 2015.

[66] A. S. Konopliv, J. K. Miller, W. M. Owen, D. K. Yeomans, J. D. Giorgini, R. Garmier, and J.-P. Barriot. A global solution for the gravity field, rotation, landmarks, and ephemeris of Eros. *Icarus*, 160(2):289–299, 2002.

[67] K. Konstantinidis, J. Adler, R. Jacob, P. Dykta, M. Thies, M. Rudolph, and R. Förstner. Simulation of autonomous landing near a plume source in a tiger stripe canyon on the south pole of Enceladus. 2016.

[68] G. Kovacs and H. Sierks. OSIRIS camera distortion and boresight correction

RO-RIS-MPAE-TN-081 / Issue: 1 / Revision: d, 2020.

[69] T. Kramer and M. Läuter. Outgassing-induced acceleration of comet 67P/Churyumov-Gerasimenko. *Astronomy & Astrophysics*, 630:A4, 2019.

[70] T. Kramer, M. Noack, D. Baum, H.-C. Hege, and E. J. Heller. Dust and gas emission from cometary nuclei: the case of comet 67P/Churyumov–Gerasimenko. *Advances in Physics: X*, 3(1):1404436, 2018.

[71] T. Kramer, M. Läuter, S. Hviid, L. Jorda, H. U. Keller, and E. Kührt. Comet 67P/Churyumov-Gerasimenko rotation changes derived from sublimation-induced torques. *Astronomy & Astrophysics*, 630:A3, 2019.

[72] L. Landau and E. Lifshitz. *Mechanics, 3rd. ed.* Pergamon Press, 1976.

[73] S. Lang. *Algebra*, volume 211 of *Graduate Texts in Mathematics*. Springer New York, New York, NY, 2002. ISBN 978-1-4612-6551-1 978-1-4613-0041-0. doi: 10.1007/978-1-4613-0041-0. URL http://link.springer.com/10.1007/978-1-4613-0041-0.

[74] M. Lauer, S. Kielbassa, and R. Pardo. Optical measurements for attitude control and shape reconstruction at the Rosetta flyby of asteroid Lutetia. In *ISSFD2012 paper, International Symposium of Space Flight Dynamics, Pasadena, California, USA*, 2012.

[75] N. N. Lebedev, R. A. Silverman, and D. Livhtenberg. Special functions and their applications. *Physics Today*, 18(12):70, 1965.

[76] C. Lhotka, S. Reimond, J. Souchay, and O. Baur. Gravity field and solar component of the precession rate and nutation coefficients of Comet 67P/Churyumov–Gerasimenko. *Monthly Notices of the Royal Astronomical Society*, 455(4):3588–3596, 2016.

[77] Z.-Y. Lin, J. Knollenberg, J.-B. Vincent, M. F. A'hearn, W.-H. Ip, H. Sierks, C. Barbieri, P. Lamy, R. Rodrigo, D. Koschny, et al. Investigating the physical properties of outbursts on comet 67P/Churyumov–Gerasimenko. *Monthly Notices of the Royal Astronomical Society*, 469:S731–S740, 2017.

[78] M. I. Lourakis and A. A. Argyros. SBA: A software package for generic sparse bundle adjustment. *ACM Transactions on Mathematical Software (TOMS)*, 36 (1):1–30, 2009.

[79] D. G. Lowe. Object recognition from local scale-invariant features. In *Proceedings of the seventh IEEE international conference on computer vision*, volume 2, pages

1150–1157. IEEE, 1999.

[80] D. G. Lowe. Distinctive image features from scale-invariant keypoints. *International journal of computer vision*, 60(2):91–110, 2004.

[81] C. Matonti, N. Attree, O. Groussin, L. Jorda, S. Viseur, S. F. Hviid, S. Bouley, D. Nébouy, A.-T. Auger, P. L. Lamy, et al. Bilobate comet morphology and internal structure controlled by shear deformation. *Nature Geoscience*, 12(3):157–162, 2019.

[82] P. F. McLauchlan. Gauge independence in optimization algorithms for 3D vision. In *International Workshop on Vision Algorithms*, pages 183–199. Springer, 1999.

[83] Y. Meng and B. Tiddeman. A Matlab implementation of the SIFT algorithm, 2016.

[84] K. Mikolajczyk. *Detection of local features invariant to affine transformations: application to matching and recognition*. PhD thesis, Grenoble INPG, 2002.

[85] O. Montenbruck and E. Gill. *Satellite orbits: models, methods and applications*. Springer Science & Business Media, 2012.

[86] J.-M. Morel and G. Yu. ASIFT: a new framework for fully affine invariant image comparison. *SIAM journal on imaging sciences*, 2(2):438–469, 2009.

[87] S. Mottola, S. Lowry, C. Snodgrass, P. Lamy, I. Toth, A. Rożek, H. Sierks, M. F. A'Hearn, F. Angrilli, C. Barbieri, et al. The rotation state of 67P/Churyumov-Gerasimenko from approach observations with the OSIRIS cameras on Rosetta. *Astronomy & Astrophysics*, 569:L2, 2014.

[88] S. Mottola, N. Attree, L. Jorda, H. U. Keller, R. Kokotanekova, D. Marshall, and Y. Skorov. Nongravitational effects of cometary activity. *Space Science Reviews*, 216(1):1–20, 2020.

[89] P. Muñoz, V. Companys, F. Budnik, B. Godard, D. Pellegrinetti, G. Bellei, R. Bauske, and W. Martens. Rosetta navigation during the end of mission phase. In *2017 International Symposium on Space Flight Dynamics, Matsuyama, Japan, ISSFD-2017-015*, 2017.

[90] P. NASA. Planetary data system standards reference. Technical Report JPL D-7669 Part 2, NASA Planetary Data System, 1992.

[91] W. Owen Jr, T. Wang, A. Harch, M. Bell, and C. Peterson. NEAR optical navigation at Eros. 2001. URL http://hdl.handle.net/2014/12992.

[92] L. O'Rourke. Science user guide for the Rosetta HK engineering data / RO-SGS-UM-1002 / Issue: 2 / Revision: 0, 2019.

[93] A. Pasewaldt, J. Oberst, K. Willner, M. Wählisch, H. Hoffmann, K.-D. Matz, T. Roatsch, H. Hussmann, and V. Lupovka. New astrometric observations of Deimos with the SRC on Mars Express. *Astronomy & Astrophysics*, 545:A144, 2012.

[94] M. Pätzold, B. Häusler, K. Aksnes, J. D. Anderson, S. W. Asmar, J.-P. Barriot, M. K. Bird, H. Boehnhardt, W. Eidel, E. Grün, et al. Rosetta radio science investigations (RSI). *Space science reviews*, 128(1):599–627, 2007.

[95] M. Pätzold, T. Andert, M. Hahn, S. Asmar, J.-P. Barriot, M. Bird, B. Häusler, K. Peter, S. Tellmann, E. Grün, et al. A homogeneous nucleus for comet 67P/Churyumov–Gerasimenko from its gravity field. *Nature*, 530(7588):63–65, 2016.

[96] M. Pätzold, T. Andert, M. Hahn, J.-P. Barriot, S. W. Asmar, B. Häusler, M. K. Bird, S. Tellmann, J. Oschlisniok, and K. Peter. The nucleus of comet 67P/Churyumov–Gerasimenko–part I: the global view–nucleus mass, mass-loss, porosity, and implications. *Monthly Notices of the Royal Astronomical Society*, 483(2):2337–2346, 2019.

[97] R. Piché. Robust multivariate linear regression using the Student-t distribution. 2012.

[98] E. Pitjeva. Updated IAA RAS planetary ephemerides-EPM2011 and their use in scientific research. *Solar System Research*, 47(5):386–402, 2013.

[99] F. Preusker, F. Scholten, K.-D. Matz, T. Roatsch, K. Willner, S. Hviid, J. Knollenberg, L. Jorda, P. J. Gutiérrez, E. Kührt, et al. Shape model, reference system definition, and cartographic mapping standards for comet 67P/Churyumov-Gerasimenko–Stereo-photogrammetric analysis of Rosetta/OSIRIS image data. *Astronomy & Astrophysics*, 583:A33, 2015.

[100] F. Preusker, F. Scholten, K.-D. Matz, T. Roatsch, S. Hviid, S. Mottola, J. Knollenberg, E. Kührt, M. Pajola, N. Oklay, et al. The global meter-level shape model of comet 67P/Churyumov-Gerasimenko. *Astronomy & Astrophysics*, 607:L1, 2017.

[101] S. Reimond and O. Baur. Spheroidal and ellipsoidal harmonic expansions of the gravitational potential of small solar system bodies. Case study: comet 67P/Churyumov-Gerasimenko. *Journal of Geophysical Research: Planets*, 121 (3):497–515, 2016.

[102] R. Schulz. The Rosetta mission: comet and asteroid exploration. *Proceedings of the International Astronomical Union*, 5(S263):312–316, 2009.

[103] B. Schutz, B. Tapley, and G. H. Born. *Statistical orbit determination*. Elsevier, 2004.

[104] T. Sémon, K. Altwegg. COPS instrument modes / RO-ROS-MAN-1019 / Issue: 1 / Revision: 7, 2011.

[105] P. Thomas, J. Joseph, B. Carcich, J. Veverka, B. Clark, J. Bell III, A. Byrd, R. Chomko, M. Robinson, S. Murchie, et al. Eros: Shape, topography, and slope processes. *Icarus*, 155(1):18–37, 2002.

[106] B. D. Tracey and D. Wolpert. Upgrading from Gaussian processes to Student'st processes. In *2018 AIAA Non-Deterministic Approaches Conference*, page 1659, 2018.

[107] V. Tsingas. Automatische aerotriangulation. *Proceedings 43rd Photogrammetric Week, Institute for Photogrammetry, Stuttgart University*, 15:253–268, 1991.

[108] C. Tubiana, C. Guettler, G. Kovacs, I. Bertini, D. Bodewits, S. Fornasier, L. Lara, F. La Forgia, S. Magrin, M. Pajola, et al. Scientific assessment of the quality of OSIRIS images. *Astronomy & Astrophysics*, 583:A46, 2015.

[109] C.-Y. Tzou. *Calibrations of ROSINA-COPS and Observations at Comet 67P/Churyumov-Gerasimenko*. PhD thesis, Universität Bern, 2017.

[110] A. Vedaldi. An implementation of SIFT detector and descriptor. *University of California at Los Angeles*, 7, 2006.

[111] R. Weidling, C. Güttler, J. Blum, and F. Brauer. The physics of protoplanetesimal dust agglomerates. III. Compaction in multiple collisions. *The Astrophysical Journal*, 696(2):2036, 2009.

[112] S. L. Wilkison, M. S. Robinson, P. C. Thomas, J. Veverka, T. J. McCoy, S. L. Murchie, L. M. Prockter, and D. K. Yeomans. An estimate of Eros's porosity and implications for internal structure. *Icarus*, 155(1):94–103, 2002.

[113] K. Willner, J. Oberst, M. Wählisch, K.-D. Matz, H. Hoffmann, T. Roatsch, R. Jaumann, and V. Mertens. New astrometric observations of Phobos with the SRC on Mars Express. *Astronomy & Astrophysics*, 488(1):361–364, 2008.

[114] K. Willner, J. Oberst, H. Hussmann, B. Giese, H. Hoffmann, K.-D. Matz, T. Roatsch, and T. Duxbury. Phobos control point network, rotation, and shape.

Earth and Planetary Science Letters, 294(3-4):541–546, 2010.

[115] S. Wong. A Matlab implementation of the SIFT algorithm, 2016.

C. Acknowledgements

First of all, I want to thank my supervisor Dr.rer.nat. Thomas Andert for letting me be a part of this stunning scientific space experiment. He has been my academic mentor for almost ten years now, covering all scientific difficulties with helpful advice. This work would not have been possible without his support. I also appreciate the chance of attending various meetings and conferences through the kindness of his invitations.

Special thanks go to Prof. Dr. rer. nat. Bernd Häusler, PD Dr. rer. nat. Martin Pätzold and Prof. Dr.-Ing. habil. Michael Schmitt for being my examiners and for chairing the disputation. I also want to thank Prof. Dr.-Ing. Roger Förstner for giving me the credit of doing all the research for this work without being able to be present in his institute.

I am grateful to the radio science community for all their advice during various meetings. Especially, I want to thank Matthias Hahn and Graciela González Peytaví for all the fruitful scientific discussions and the support with the high performance computing.

Many thanks go to all members of the Osiris team. Special thanks go to Dr. Holger Sierks and Dr. Carsten Güttler for sharing their wonderful images and their scientific advice. Their products revealed cometary features on an impressive level of detail as never seen before.

I would like to thank the German Air Force for approving duty travels to each single scientific meeting with the Radio Science Investigations community. This has given me great support during this work.

Finally and at the very most, I want to say thank you to my family. This work would not have been possible without many hours of patience and support of my wife Franziska. I sincerely thank my parents for their endless support and my kids for making northern Germany a sunny place.